# PHYSICAL PROPERTIES AND SILICA DIAGENESIS

A DISSERTATION

SUBMITTED TO THE DEPARTMENT OF

GEOLOGICAL AND ENVIRONMENTAL SCIENCES

AND THE COMMITTEE ON GRADUATE STUDIES

OF STANFORD UNIVERSITY

IN PARTIAL FULFILLMENT OF THE REQUIREMENTS

FOR THE DEGREE OF

DOCTOR OF PHILOSOPHY

Caren Jill Chaika

August 1998

## ABSTRACT

Silica diagenesis in the Monterey Formation is of considerable interest to the petroleum industry because this unit is a major California hydrocarbon source and reservoir rock. Measurements of porosity, density, and ultrasonic velocity from dry core plugs in three Monterey Formation reservoirs in California's San Joaquin Valley are analyzed along with their corresponding well logs. Furthermore, these observations are compared to available data from other siliceous rocks of the Monterey Formation, the North Sea and the Sea of Japan. This work describes two distinct patterns of porosity reduction (Group 1 and Group 2) in siliceous rocks.

This thesis is organized so that each chapter gives additional physical properties by which to distinguish the two porosity reduction patterns.

The two patterns can be distinguished using density, porosity, and mineral content data (Chapter 1); therefore, they can be distinguished using outcrop or core data. Most dramatically, the two patterns can be identified by falling on one of two dry bulk density-porosity trends. In Group 1, grain density increases with decreasing porosity, the amount of opal-CT decreases while the amount of non-silica minerals (and quartz, if present) content increases, and the gradual opal-A/opal-CT transition shows no abrupt porosity change. In this case, porosity reduction appears to be due to increased amounts of non-silica minerals. In Group 2, grain density decreases with decreasing porosity, the amount of opal-CT (and quartz, if present) increases while the content of non-silica minerals decreases, and the opal-A/opal-CT transition is abrupt with a sharp decrease in porosity. In these rocks, porosity is reduced predominantly through addition of silica.

The patterns can be distinguished in trends of density or porosity versus impedance or elastic moduli (Chapter 2); therefore, they can be distinguished using well log or seismic data. One interesting and useful observation, however, is that the two groups

do not separate in graphs of ultrasonic compressional- or shear-wave velocity versus porosity or density. Instead, the data are strongly linear. Furthermore, both an analogy to chalk and effective medium modeling (Chapter 3) supports my hypothesis that the two porosity reduction patterns correspond to two textures.

There are several practical uses in identifying which porosity reduction trend best applies to a particular dataset. Because the two bulk density- porosity regressions have a high correlation coefficient, porosity can be predicted from bulk density if the porosity reduction trend is already known. A tool to calculate porosity from density in well logs is useful because one commonly used method, density- porosity, calculates porosity by incorrectly assuming that grain density is constant. Porosity calculated using my density-porosity transform approximates direct measurements much better than the neutron porosity tool and at least as good as density- porosity. This transform is not only effective in characterizing siliceous rocks from the Monterey Formation, but is also an effective tool to calculate porosity in siliceous rocks from other locations, such as the Norwegian North Sea and the Sea of Japan.

The last chapter documents some work about stress sensitivity of sandstones.

Laboratory measurements show that the variation of a sandstone's elastic moduli to changes in hydrostatic pressure increases with decreasing porosity. The difference between dry-rock elastic moduli of the same samples measured at high and low stress is close to zero as porosity approaches critical porosity (about 0.38 for sandstones), and reaches its maximum as porosity approaches zero. This relationship can be explained by using a combination of the critical porosity model and the modified solid model. This combined model yields a practical recipe for estimating P- and S-wave velocities versus stress from a single measurement.

## ACKNOWLEDGMENTS

There are many people without whose guidance and support would this project would have been impossible. Foremost, I am grateful to Jack Dvorkin, my advisor in almost every way. Jack's patience and intellect have sustained me when I most needed it, and for that I will always be grateful. My official advisor, J. G. Liou, encouraged me to complete this cross-disciplinary project and kept me informed of the official procedures and deadlines. Steve Graham also gave me intellectual guidance, particularly by encouraging my correspondence with Loretta A. Williams, who helped tremendously in refining both my ideas and the organization of this thesis.

Many individuals and organizations were instrumental in compiling this data. The siliceous shales team of Chevron provided the samples from Cymric, Asphalto, and McKittrick and paid for FTIR; I would like to specifically thank Tom Zalan, Bruce Bilodeau, Steve Smith, Fred Bair, and Scott Johnson for their knowledge and input. The Shell data from North Belridge was acquired at the Core Warehouse at California State University, Bakersfield; the Mobil data from South Belridge was provided by Tony Murer. The data from Elk Hills was provided by Tony Reid and Jana McIntyre at Occidental; the data, samples, and money for FTIR analyses on the samples from the North Sea were provided by Norsk Hydro; and many other datasets are from the Rockphysics database.

The Rockphysics group provided both resources and encouragement necessary for this project. The ultrasonic laboratory measurements were made in the Stanford Rockphysics Laboratory under the direction of Azra Tutuncu and Manika Prasad. Without their guidance, advice, and support, I never would have been able to complete my measurements.

Many friendships sustained me during my years here. I am blessed with terrific friends like Anthea Lee, Raphael Thomadsen, Jingqing Chai, Jeff Warwick, and Bashir

Koledoye. Your support during the difficult times and your joy during the good times are more appreciated than you will ever know. The greatest support, however, has been from my parents. Thank you for long telephone conversations and needed visits. I am grateful for the times when you gave advice, and the times you just listened.

Financial support for this work was provided by the Shell and McGee funds and the Petroleum Research Fund of the American Chemical Society, (ACS-PRF #32743-AC2).

# TABLE OF CONTENTS

## CHAPTER 1: POROSITY REDUCTION DURING SILICA DIAGENESIS



## CHAPTER 2: ULTRASONIC VELOCITIES OF OPALINE ROCKS UNDERGOING SILICA DIAGENESIS

## CHAPTER 5: STRESS SENSITIVITY OF SANDSTONES

# LIST OF TABLES

# LIST OF FIGURES

# CHAPTER 1

# POROSITY REDUCTION DURING SILICA DIAGENESIS

## ABSTRACT

There are two distinct patterns of porosity reduction in reservoir rocks of the Monterey Formation, California, as they undergo silica diagenesis from opal-A through opal-CT to quartz. One way to recognize the two groups (Group 1 and Group 2) is that they separate along two bulk density- porosity trends. Furthermore, in Group 1 grain density increases with decreasing porosity, the fraction of opal-A plus opal-CT decreases while the fraction of non-silica minerals (and quartz, if present) increases, and the opal-A/opal-CT transition has a smooth decrease in porosity. In these rocks, porosity reduction appears to be due to increased amounts of non-silica minerals. In Group 2, grain density decreases with decreasing porosity, the amount of opal-CT (and quartz, if present) increases while the fraction of non-silica minerals is relatively constant, and the opal-A/opal-CT transition is marked by an abrupt decrease in porosity. In these samples, porosity is reduced predominantly through addition of silica to the rocks.

## INTRODUCTION

Diatoms, radiolaria, and other siliceous organisms precipitate silica from seawater as amorphous opal (opal-A). After deposition, silica progresses from opal-A towards quartz, the stable phase, through an intermediate phase, opal-CT. Empirical evidence suggests that each transition occurs through dissolution and reprecipitation (Murata and Randall, 1975; Pisciotto, 1981; Rimstidt and Barnes, 1980.)

These diagenetic transitions cause changes in density and porosity. With the change from opal-A to opal-CT, grain density increases by about 0.1 $g/cm^3$ and porosity may

reduce by 20% (Murata and Larson, 1975; Beyer, 1987). However, because opal-A and opal-CT are not composed of well-ordered crystals (Graetsch, 1994), the density of each polymorph can vary.

Relationships among velocity, porosity, density, mineral content, and the stage of silica diagenesis have been recognized from laboratory and well log studies of opaline rocks (Beyer, 1987; O'Brien et al., 1989; Nobes et al., 1992; Tribble et al., 1992; Guerin and Goldberg, 1996). Changes in acoustic impedance (the product of density and velocity) due to silica transformations can be dramatic; bottom simulating reflectors on seismic profiles in the Pacific Ocean and North Sea mark the depth of the opal-A to opal-CT transition (Hein et al., 1978; Bohrmann et al., 1992). This work concentrates on understanding physical laws behind trends that link porosity, density, mineralogy, and the stage of silica diagenesis.

The principal finding of this work is that two different patterns (Group 1 and 2) of porosity reduction exist in opaline rocks. These two porosity reduction mechanisms correspond to two linear bulk density - porosity transforms. As porosity decreases in Group 1 rocks, the content of non-silica minerals increases, and the opal-A/opal-CT transition is marked by a gradual porosity decrease. In Group 2, decreasing porosity is accompanied by an increase in silica content, and the opal-A/opal-CT transition is marked by a sharp drop in porosity.

## SAMPLE ORIGIN AND PREPARATION

Silica diagenesis in the Monterey Formation is of considerable interest to the petroleum industry because this unit is a major California hydrocarbon source and reservoir rock. Identifying the causes for porosity reduction and pathways by which it occurs is important for understanding petroleum migration and the development of reservoirs. Furthermore, much of what is learned from studies of the Monterey Formation can be used in other reservoir units throughout the world where silica diagenesis is an issue.

This study presents new core data from five oil fields in the southwest San Joaquin Valley. Mineralogy, porosity and density on the Cymric, Asphalto, and McKittrick reservoir samples were determined for this study; the North and South Belridge data were supplied by Shell and Mobil Petroleum Companies, respectively. These three parameters are shown for all samples in Appendix A. This information was supplemented with data supplied by Occidental Petroleum Company from the Elk Hills reservoir in the San Joaquin Valley (Reid and McIntyre, in prep), and published outcrop data collected both near Point Pedernales (Compton, 1991) and along the Santa Barbara coast (Isaacs, 1980). Relative locations are shown in Figure 1.

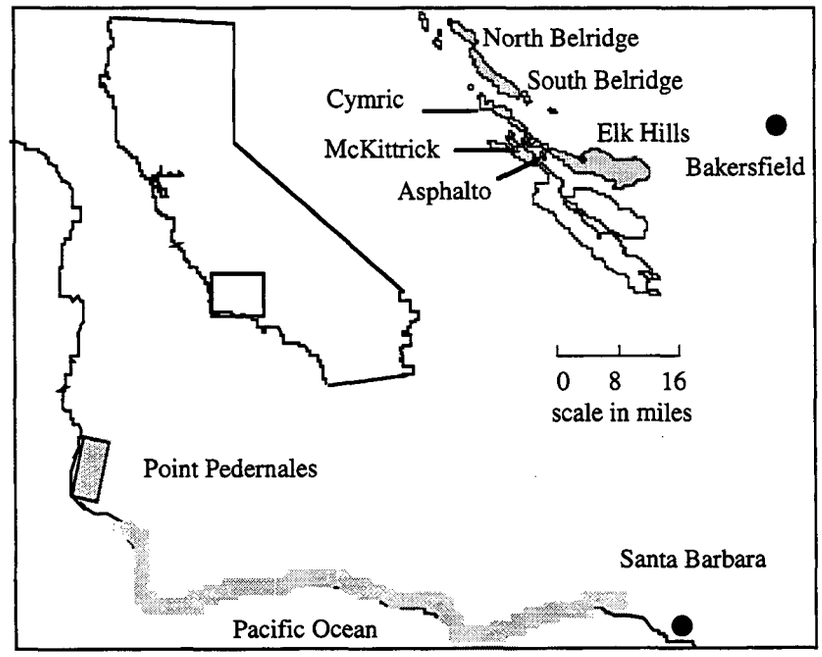


Figure 1. General locations from where samples were taken.

The samples from Cymric, North and South Belridge fields and Point Pedernales traverse the opal-A/opal-CT transition, those from McKittrick contain opal-CT, and those from Asphalto and Elk Hills span the opal-CT/quartz transition.

Methods for determining mineralogy, porosity, and density for the San Joaquin Valley samples are similar to each other. When known, the weight percent of the minerals in all these samples were determined with Fourier Transform Infrared Spectroscopy (FTIR), discussed by Harville and Freeman (1988). Weight percentages of different minerals are reproducible within 5%. Pore fluids in all samples were removed by Dean Stark method, which involves cleaning the samples with boiling toluene at approximately 115° C and then removing the remainder of the oil with methylene chloride which boils at about 45° C. All samples were dried in either a humidity controlled oven or a convection oven at approximately 115° C for between four and 48 hours. FTIR analyses show that waters of hydration remain bound to both opal and clay minerals. In determining porosity and density, the weight of the matrix was determined after all pore fluids were extracted; both grain volume and porosity were determined using Boyle's law and helium as the gaseous medium. Bulk density is calculated from porosity and grain density. The samples from Cymric, McKittrick, and Asphalto were cut into cylindrical plugs with a saw blade lubricated with liquid nitrogen. After preparation, all samples were kept room-dry.

Compton (1991) and Isaacs (1980) both determined mineralogy using a combination of X-ray diffraction (XRD), elemental analyses, and organic carbon analyses. In examining samples collected near Point Pedernales, Compton also used X-ray fluorescence (XRF), petrography, and scanning electron microscopy (SEM) to determine the weight fractions of the different constituent minerals. Similarly, in examining samples from the Santa Barbara coast, Isaacs supplemented the above methods with constants of proportionality to determine different mineral fractions that would be under- or over-represented using conventional methods.

Porosity and grain density of the Point Pedernales samples was measured according to Archimedes' principle-- porosity and the mass of the grains were determined by weighing the samples both before and after being vacuum impregnated with toluene, and the volume determined by comparing the latter weight to the weight of the sample while immersed in

toluene. The initial, dry weight was made after the samples were dried overnight at 105° C. Compton (1991) reports that his porosity measurements are repeatable within 0.5%.

In contrast, the samples collected along the Santa Barbara coast were heated at 100° to 105° C for 24 hours before density was measured. After being dried, the samples were kept in a dessicator until all measurements were made. First, mass was measured, then bulk volume was measured with a vacuum-equipped mercury pycnometer; grain volume was measured with a helium pycnometer. Porosity was determined from measurements of bulk and grain density. Isaacs (1980) reports that bulk density measurements are reproducible within 5% and grain density is reproducible within 1%. However, she notes that porosity was determined under dry conditions, and is not comparable to "humidified" conditions because water normally would re-adsorb onto opal-A and opal-CT. She writes that "dry and humidified values of porosity, however, may differ considerably-- for opal-CT rocks with 5 to 10 percent adsorbed water by weight, by 7 to 20 porosity percent...."

While the samples from the Santa Barbara coast were kept fully dry, all other samples were kept room-dry, which corresponds to humidified values. Because of this difference in methodology, the porosity and the density of the rocks collected along the Santa Barbara coast cannot be compared to that of the other samples. However, these samples will be compared to each other, and relative trends noted.

Although the total silica content is at least 40% in all analyzed samples from North and South Belridge, Cymric and Asphalto, it was sometimes less in samples from Elk Hills, Point Pedernales and the Santa Barbara coast. The low-silica samples are generally rich in carbonates or clay minerals, both of which have physical properties very different from opaline rocks. To be comparing similar rocks, the datasets from Elk Hills, Point Pedernales and the Santa Barbara coast were restricted to only include samples where the silica content exceeded 40%.

## TWO POROSITY REDUCTION PATTERNS

Trends of dry-rock bulk density $\rho_b$ versus porosity $\phi$ (Figure 2a) can be described:

$$\rho_b = 2.581 - 2.725\phi, \quad R^2 = 0.990; \tag{1}$$

and

$$\rho_b = 2.061 - 1.926\phi, \quad R^2 = 0.955; \tag{2}$$

where density is in g/cm$^3$ and $R^2$ is the correlation coefficient. A correlation coefficient near 1.0 indicates that the variation in bulk density is almost entirely explained by porosity variation. Regression (1) describes the Elk Hills, Belridge, Cymric, and Asphalto samples and is based on 97 data points; regression (2) describes the Point Pedernales and McKittrick samples and is based on 34 data points. Subsequently, the samples described by Equations (1) and (2) will be termed Group 1 and Group 2, respectively.

Grain density is calculated from dry bulk density according to $\rho_b = \rho_s(1-\phi)$. If grain density is constant, changes in $\rho_b$ will be solely due to porosity changes. However, Figure 2b and Equations (3) and (4) show that grain density is not constant. Furthermore, the regression coefficients show that although porosity explains most of the variation in bulk density, it is not as significant in explaining variations in grain density.

Grain density increases with porosity reduction in the Group 1 samples according to:

$$\rho_s = 2.410 + 0.999\phi - 1.879\phi^2, \quad R^2 = 0.697; \tag{3}$$

and decreases with porosity reduction in the Group 2 samples according to

$$\rho_s = 1.922 + 1.142\phi - 0.535\phi^2, \quad R^2 = 0.286. \tag{4}$$

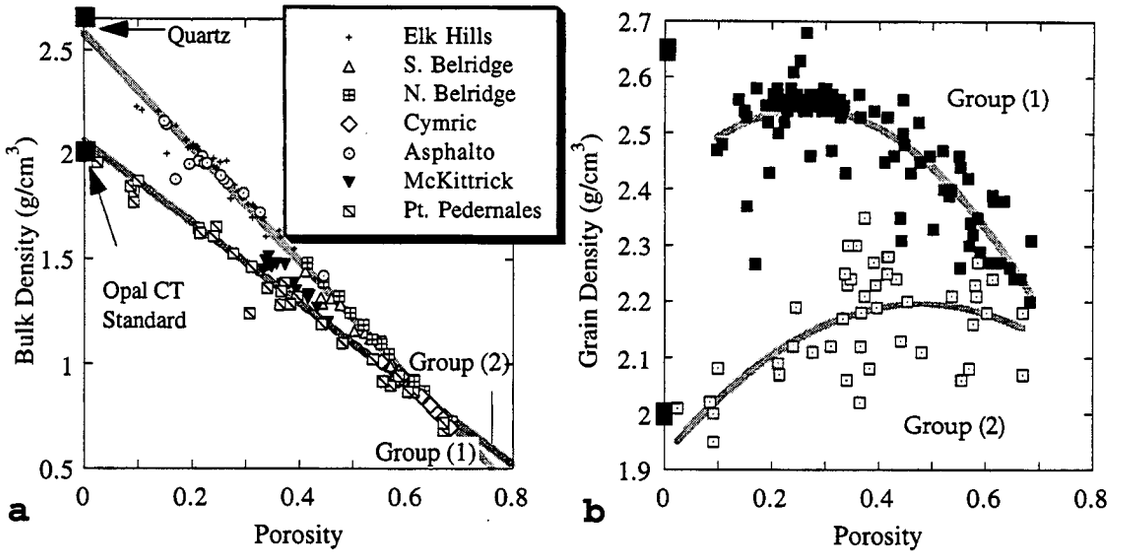


Figure 2. (a) Dry-rock bulk density and (b) grain density versus porosity.

Grain density is sensitive to the types and relative abundance of the minerals forming the rock. The grain density of opal-A is less than that of opal-CT, and both are much less than most other rock-forming minerals. Therefore, grain density could increase due to an increased fraction of (a) non-silica minerals over silica minerals or (b) opal-CT over opal-A, or (c) quartz over opal-CT with decreasing porosity. I argue that (a) and (c) are responsible for the grain density-porosity trend in the Group 1 rocks. Furthermore, the trends of the Group 2 rocks with decreasing porosity are controlled by (b) above 40% porosity and the reverse of (a) below 45% porosity. In other words, below 45% porosity, grain density decreases because the fraction of non-silica minerals decreases with decreasing porosity.

To support this hypothesis, Figure 3 shows silica and non-silica minerals versus porosity for the two groups. Group 1 includes North and South Belridge, Cymric, and Asphalto; Group 2 includes McKittrick and Point Pedernales. Elk Hills will not be shown on further graphs because specific mineralogy was not provided.

The trends in both Figure 3a and 3b are similar above 45% porosity. As porosity decreases from 70% to 45%, biogenic silica mineral content decreases while the content of other minerals increases. Because the porosity decrease is continuous, a change in porosity is not noticeable at the opal-A/opal-CT transition (Figure 3a). In other words, Group 1 opal-CT reservoirs may have as much matrix porosity as Group 1 opal-A reservoirs. In contrast, above 50% porosity in Figure 3b, all biogenic silica is opal-A, whereas below porosity of 43%, only opal-CT is present.

Below 45% porosity, Group 1 and Group 2 have different trends. In the Group 1 samples (Figure 3a) the trend at higher porosity repeats itself: the silica content decreases and the non-silica content increases with decreasing porosity. The most striking difference between the two groups, however, is that there are no Group 2 samples with porosity between 43%-50% (Figure 3b). Thus, opal-A rocks with porosity of 50% must directly overlie opal-CT rocks of 43% porosities or less. This abrupt phase change and porosity decrease results in the bottom simulating reflector phenomenon previously mentioned.

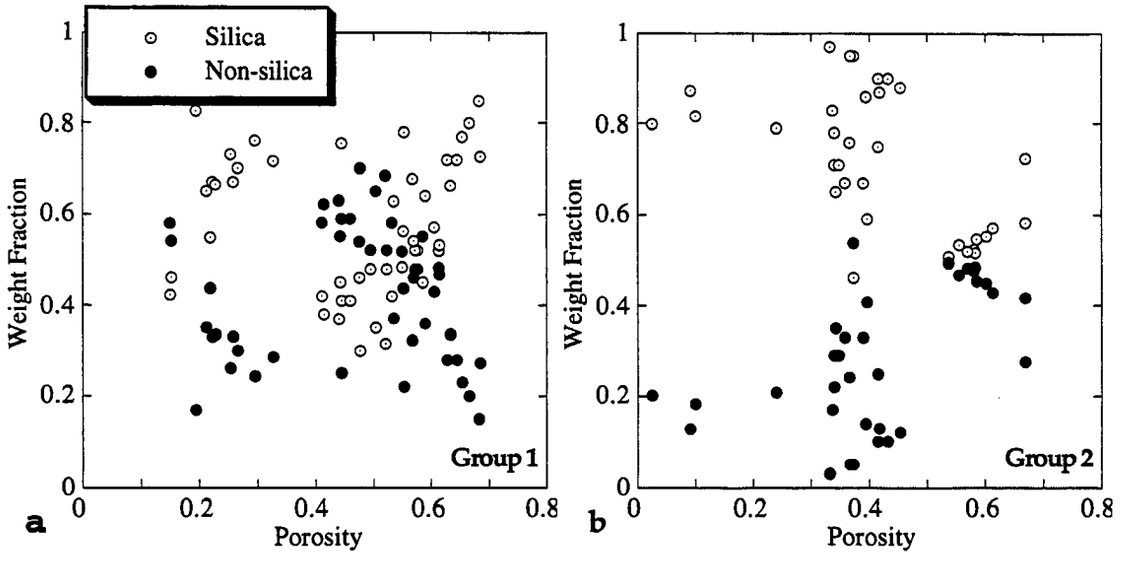


Figure 3. Fraction of silica and non-silica minerals in (a) Group 1 and (b) Group 2. samples.

The two grain-density porosity trends can be explained using Figure 3. The increase in grain density with decreasing porosity at porosity above 45% in all samples appears primarily due to an increase in non-silica minerals. Below 45% porosity, non-silica minerals also cause an increase in grain density, with an increase in biogenic quartz playing a smaller role. Below 43% porosity in the Group 2 samples, there is a slight increase in silica minerals; this explains the decrease in grain porosity with decreasing porosity in this region (and the low correlation coefficient of the regression).

Figure 4 shows bar charts of the fraction of opal-A, opal-CT, quartz, and non-silica minerals of each sample in Group 1 (excluding Elk Hills), Group 2, and Santa Barbara, sorted by porosity. The value of this analysis is that I can link the relative abundance of these mineral groups in each sample. Furthermore, the Santa Barbara samples can be included in this analysis because the samples are merely sorted by porosity (absolute values are not used) and because the samples within a dataset are primarily being compared to each other. Comparing the Group 1, Group 2, and Santa Barbara samples permits categorization of the latter dataset.

## DEFINING GROUP 1, GROUP 2

Although Group 1 and Group 2 can be recognized solely by their placement on a graph of dry bulk density versus porosity (Equations 1 and 2), this method cannot be used to classify the Santa Barbara data because porosity and density were measured on dry, rather than humidified samples. However, in addition to different porosity-density trends, Group 1 and Group 2 rocks differ in ways which can be contrasted with Isaacs' (1980) data collected along the Santa Barbara coast. The data from Santa Barbara have the following characteristics: a decrease in porosity at the opal-A to opal-CT transition with an absence of samples from about 45% to 55% porosity, and, with one exception, all samples contain either opal-A or opal-CT. These observations plus the others collated in Table 1 suggest that the Santa Barbara data belongs to Group 2.

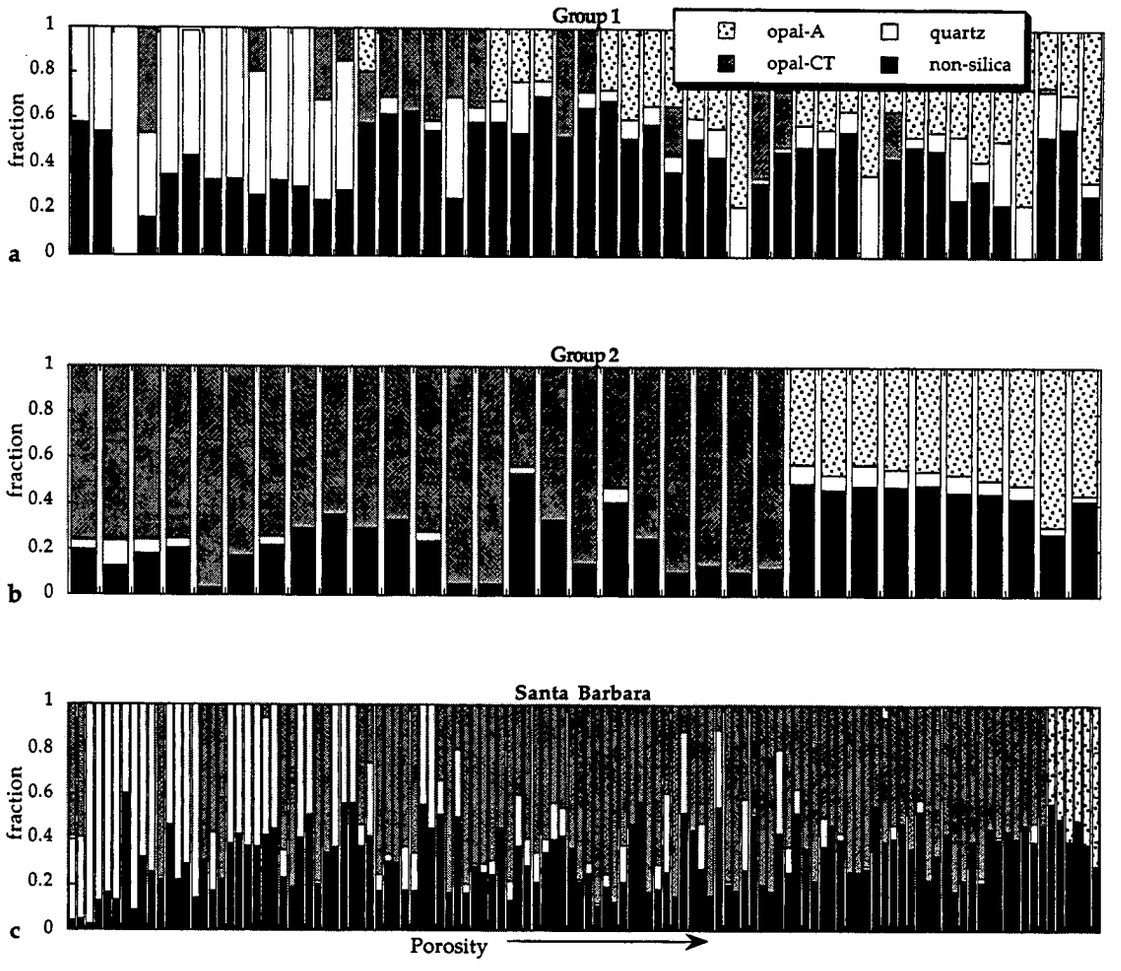


Figure 4. Bar charts of the weight fractions of the amount of opal-A, opal-CT, quartz, and non-silica minerals in the samples from (a) Group 1 excluding Elk Hills, (b) Group 2, and (c) samples collected along the Santa Barbara coast.

Table 1. Variations in porosity with silica diagenesis in Group 1, Group 2, and the samples collected along the Santa Barbara coast.

| diagenetic phase | Group 1 | Group 2 | Santa Barbara |
|---|---|---|---|
| opal-A | mixed with opal-CT<br>opal-A + opal-CT decreases<br>non-silica content increases | opal-A constant<br>non-silica content increases | opal-A decreases<br>non-silica content increases |
| opal-A to opal-CT | many samples exist | no samples | one sample |
| opal-CT | see opal-A | opal-CT increases slightly<br>non-silica decreases slightly | opal-CT increases slightly<br>non-silica decreases slightly |
| opal-CT to quartz | quartz increases (total silica content decreases slightly)<br>non-silica content increases | N/A | opal-CT + quartz increases<br>non-silica decreases |

## COMPACTION

These Monterey Formation samples can be categorized into two sample groups which show different porosity reduction patterns during diagenesis. Because compaction is the process most commonly used to explain porosity reduction during silica diagenesis (Tada and Iijima, 1983; Isaacs, 1981; Iijima, 1988; Compton, 1991), I need to determine if compaction can explain the variations in porosity with depth in the two Groups.

The most obvious way to identify the occurrence of compaction is to plot porosity with depth, and compare the field trends to those established in a controlled laboratory experiment. I will follow the methodology of Compton (1991), who compared the trends of the Point Pedernales samples to laboratory compaction experiments on diatomite performed by Bryant et al. (1981). Compton assumed a maximum burial depth of 0.5 km. Similarly, from Bowersox (1990) I assume a maximum burial depth of 282 meters in the North and South Belridge samples and combine the datasets in Figure 5a. The other reservoirs are excluded because satisfactory burial information was not found.

The three regressions describe two porosity-depth relationships for Compton's data: where (a) depth <0.5 km, and (b) depth >0.5 km with 41% diatoms. The third porosity-depth relationship (c) is from the compaction experiment (Bryant et al., 1981) performed on samples with 60-70% diatoms at increasing pressure. The North and South Belridge samples contain an average of 47% opal-A; they should follow regression (b).

Only the opal-A-bearing samples from Point Pedernales show a clear relationship between porosity and depth; because the compaction curves do not fit the samples from North and South Belridge, some other factors are affecting porosity reduction. Assuming that the North and South Belridge samples are indicative of the other Group 1 samples, I reject compaction as a primary porosity reduction mechanism in the Group 1 opal-A samples.

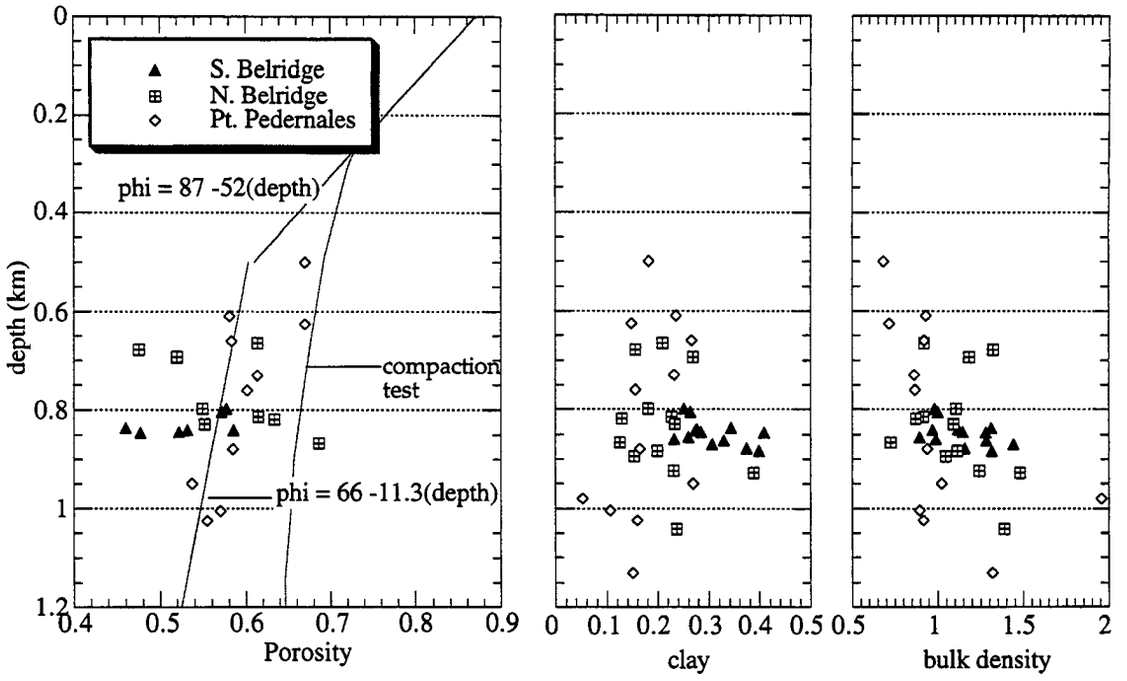


Figure 5. (a) Maximum burial depth versus porosity in opal-A-bearing rocks, (b) volumetric fraction of clay, and (c) bulk density in the samples from North and South Belridge and Pt. Pedernales.

Another explanation for the trends of silica and non-silica minerals with porosity is that the older, deeper, more diagenetically altered samples were deposited in a somewhat different depositional environment. Thus, the variations in silica and non-silica minerals with porosity that we have noted in previous graphs may actually represent changes in the depositional environment. To pursue this, Figure 5b and 5c show variations in clay and bulk density with depth in the three datasets. Samples with both opal-A and opal-CT are shown. Again, there appears to be smaller changes in both clay and bulk density with depth in the Point Pedernales than those from North and South Belridge. Therefore, if environmental changes are responsible for the variations in the North and South Belridge samples shown in Figure 5, the environmental changes are more abrupt than those recorded in the samples from Point Pedernales.

A third explanation for the variation in silica and non-silica fractions with porosity in the two porosity reduction mechanism is that clay minerals can also be precipitated during diagenesis. This hypothesis is the focus of the next section.

Because all previous graph has represented only non-silica minerals, I need to explicitly show or state how much of this non-silica fraction is clay minerals. In all seven datasets, 40% to 60% of the non-silica minerals are clay minerals (Appendix A). After clay minerals, feldspar minerals are the next most abundant non-silica group. Furthermore, Group 1 samples generally have greater amounts of clay than the Group 2 samples.

## INTERPRETATION

I postulate that as porosity decreases, the increase in non-silica minerals is partly due to precipitation of aqueous silica as clay rather than opal-CT. One area where there is strong evidence for this is DSDP Hole 584, which sampled clay-rich siliceous sections in the Japan Trench (Tribble et al., 1992). With depth, opal-A decreased in abundance; however, no opal-CT precipitated (Figure 6). It appears that clay has precipitated at the expense of opal-CT in these samples. If Figure 6 shows clay forming at the expense of opal-CT in clay-rich rocks and Figure 4b shows that Group 1 has higher clay than Group 2, then it is possible that the Group 1 rocks from the San Joaquin Valley also followed a path of clay precipitation at the expense of silica minerals.

One method suggested to determine if clay minerals are detrital or authigenic is to analyze clay crystallinity (e.g., Frey, 1987). Unfortunately, this analysis is generally not successful in fine-grained rocks. Clay crystallinity analysis assumes that the pore spaces of the rock are large enough for euhedral crystals to form. In fine-grained rocks such as those in this study, it is impossible to differentiate between very small well-formed crystals and very small broken detrital bits.

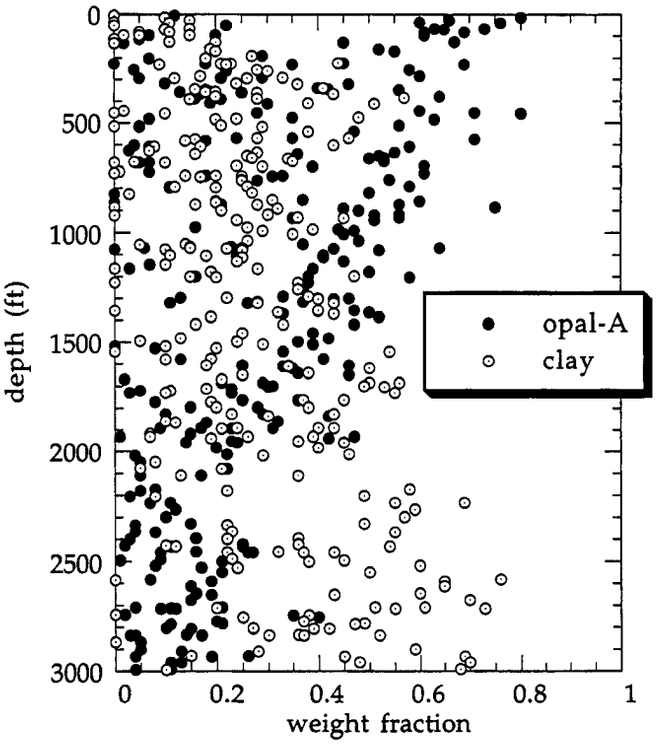


Figure 6. Opal-A and clay content versus depth in DSDP Hole 584.

Many workers have shown that silica transformations can be accelerated or retarded due to variations in detrital mineral and/or carbonate content (Merino, 1975b; Kastner et al., 1977, Isaacs, et al., 1983, Williams and Crerar, 1985), the presence of organic acids (Hinman, 1990), and other pore water chemistry variations (Merino, 1975a). Because clay minerals retard the opal-A to opal-CT transition, a clay-rich rock is likely to also be an opal-A-rich rock, and therefore have greater porosity. Other possibilities for the variation in clay with porosity are that clays are destroyed during diagenesis in Group 2 samples, or that it is due to variation in the depositional environment with time.

In the Group 2 rocks, opal-A phase rocks have noticeably more porosity than opal-CT phase rocks. In these rocks, clay minerals affect porosity in two ways: (a) they diminish porosity by clogging pores, and (b) retard the opal-A to opal-CT transition.

Although the type of diagenetic transition described as Group 2 has gotten much notice in the literature, particularly by Isaacs (1980), some observations which can be attributed to Group 1 porosity reduction trends have also been noted. Porosity decrease in diatomites of the South Belridge field was attributed to increased abundance of non-opaline minerals by Schwartz (1988), and porosity reduction specifically caused by precipitation of silica minerals in pore spaces was noted by Williams et al. (1985).

The observations presented above suggest the following interpretation: after dissolution of opal-A, Group 1 reservoirs gradually replace porosity with clay minerals. Silica content decreases with decreasing porosity because clay minerals are added to the system through inflow and precipitation from pore waters (an open system). For example, precipitation of smectite is observed throughout the Monterey Formation rocks of the San Joaquin Valley (L Williams, pers. comm., 1998). In contrast, after dissolution of opal-A in Group 2 reservoirs, porosity is replaced by opal-CT. This amount of opal-CT is greater than the amount of dissolved opal-A (Figure 4b); therefore, the silica is added to the system through inflow and precipitation from pore waters, again in an open system.

Whether precipitation of silica or clay is preferred geochemically is determined by the pore water chemistry and mineralogy of the opal-A phase rock. The Group 1 rocks contain more clay and thus, if they are in equilibrium with the pore waters, it is likely that the pore fluids contain more dissolved cations than the Group 2 rocks. Thus, in some geologic environments, precipitation of clay will be preferred to silica. Since clay is known to retard the opal-A to opal-CT transition, additional clay will cause not only a slower but also a less dramatic transition, producing less opal-CT than a Group 2 rock (e.g., Figure 4).

## SUMMARY

Porosity reduction in opaline rocks of the Monterey formation occurs through two distinct pathways. In the beginning, samples bearing opal-A have similar physical properties: high porosity and relatively constant amounts of opal-A in the solid. For some

reason, precipitation of opal-CT is retarded in Group 1 samples relative to Group 2 rocks. The opal-CT which precipitates in Group 1 rocks has high porosity like opal-A, and opal-A and opal-CT coexist. In Group 1, porosity decreases due to a diagenetic increase in non-silica minerals, producing gradual changes in porosity and density with silica diagenesis. In Group 2, porosity reduction is controlled by a diagenetic increase in silica content. This pathway is characterized by an abrupt opal-A/opal-CT transition.

The principal difference between these two groups is illustrated in Figure 7 by comparing the non-silica fraction versus porosity in the two groups. Group 1 samples (Figure 7a) shows a **continuous** reduction in porosity due to a gradual increase in non-silica minerals. Group 2 (Figure 7b) exhibits an **abrupt** porosity reduction from 53% to 45% due to the opal-A to opal-CT transition.

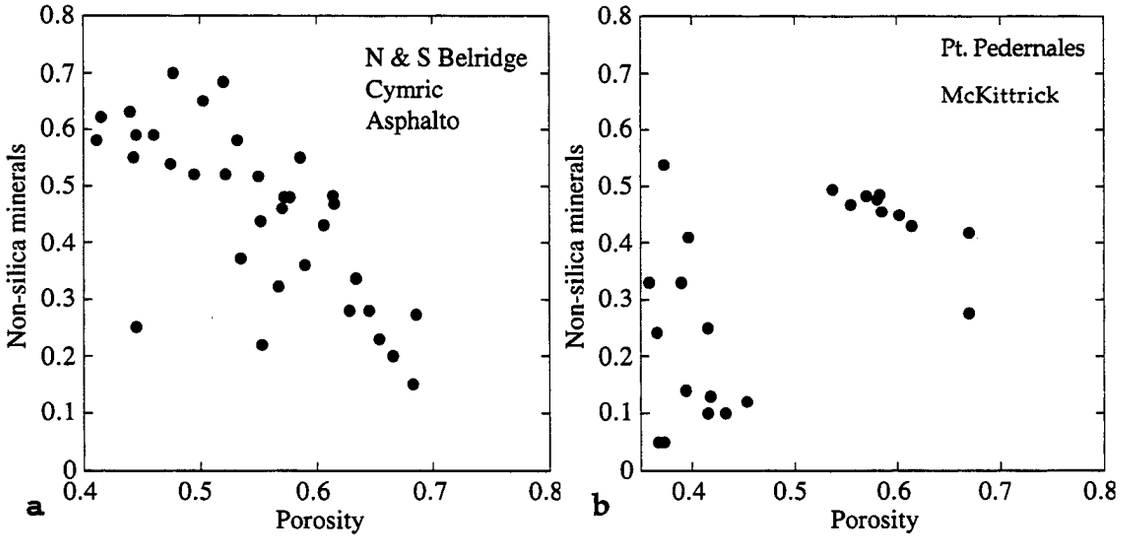


Figure 7. Non-silica minerals versus porosity in the (a) Group 1 and (b) Group 2 samples.

# CONCLUSIONS

## Group 1

Although conclusions for the Group 1 samples will be offered through the entire porosity range, those below 40% porosity are more uncertain because the data come from one region. The porosity reduction mechanism for Group 1 samples has theses features:

(a) $\rho_b = 2.581 - 2.725\phi, \quad R^2 = 0.990;$

(b) Grain density generally increases with porosity reduction.

(c) Samples containing both opal-A and opal-CT are common.

(d) Non-silica content generally increases with decreasing porosity. Ater quartz begins to precipitate, the quartz fraction increases with decreasing porosity although the total silica content decreases.

(e) Mechanical compaction does not appear to be a reasonable porosity reduction mechanism.

## Group 2

The samples from Point Pedernales, McKittrick, and the Santa Barbara coast suggest that the Group 2 rocks have the following features:

(a) $\rho_b = 2.061 - 1.926\phi, \quad R^2 = 0.955$

(b) Grain density generally decreases with porosity reduction.

(c) Each sample contains either opal-A or opal-CT (opal-CT and quartz may coexist), where the porosity of rocks with opal-A is greater than 53% and the porosity of rocks with opal-CT is less than 45%.

(d) Non-silica fraction content generally decreases with decreasing porosity; the content of opal-CT (and quartz, if present), increases.

## REFERENCES

Beyer, L. A., 1987, Porosity of unconsolidated sand, diatomite, and fractured shale reservoirs, South Belridge and West Cat Canyon Oil Fields, California, in R.F. Meyer, ed., Exploration for heavy crude oil and natural bitumen: AAPG Studies in Geology, **25**, 395-413.

Bryant, W. R., Bennett, R. H., Katherman, C. E., 1981, Shear strength, consolidation, porosity, and permeability of oceanic sediments, *in* Emiliani, C., ed., The sea; ideas and observations in the study of the seas, Volume 7: The oceanic lithosphere, 1555-1616.

Bohrmann, G., Spiess, V., Hinze, H. and Kuhn, G., 1992, Reflector "Pc" a prominent feature in the Maud Rise sediment sequence (eastern Weddell Sea): Occurrence, regional distribution and implications to silica diagenesis: Marine Geology, **106**, 69-87.

Bowersox, J. R., and Shore, R. A., 1990, Reservoir compaction of the Belridge Diatomite and surface subsidence, South Belridge Field, Kern County, California in J. G. Kuespert, and S. A. Reid, eds., Structure, stratigraphy, and hydrocarbon occurrences of the San Joaquin Basin, California: Field Trip Guidebook-- Pacific Section SEPM, **64**, 225-230.

Compton, J. S., 1991, Porosity reduction and burial history of siliceous rocks from the Monterey and Sisquoc Formations, Point Pedernales area, California: Geological Society of America Bulletin, **103**, 625-636.

Frey, M., 1987, Very low-grade metamorphism of clastic sedimentary rocks in M. Frey, ed., Low Temperature Metamorphism, New York, Chapman and Hall, 9-58.

Graetsch, H., 1994, Structural characteristics of opaline and microcrystalline silica minerals in P. J. Heaney, C. T. Prewitt and G. V. Gibbs, eds., Reviews in Mineralogy, Volume 29: Silica: Physical behavior, geochemistry and materials applications: Washington, D. C., Mineralogical Society of America, 209-232.

Guerin, G. and Goldberg, D., 1996, Acoustic and elastic properties of calcareous sediments across a siliceous diagenetic front on the eastern U.S. continental slope: Geophysical Research Letters, **23**, 2697-2700.

Harville, D. G. and Freeman, D. L., 1988, The Benefits of Application of Rapid Mineral Analysis Provided by Fourier Transform Infrared Spectroscopy: SPE Conference Proceedings, 141-146.

Hein, J. R., Scholl, D. W., Barron, J. A., Jones, M. G., Miller, J., 1978, Diagenesis of late Cenozoic diatomaceous deposits and formation of the bottom simulating reflector in the southern Bering Sea: Sedimentology, **25**, 155-181.

Hinman, N. W., 1990, Chemical Factors influencing the rates and sequences of silica phase transitions: Effects of organic constituents: Geochimica et Cosmochimica Acta, **54**, 1563-1574.

Iijima, A. 1988, Diagenetic Transformations of Minerals as Exemplified by Zeolites and Silica Minerals -- a Japanese View, in G. U. Chilingasia and K. H. Wolf, eds., Diagenesis II: New York, Elsevier, 147-211.

Isaacs, C. M., 1980, Diagenesis examined laterally along the Santa Barbara coast, California: Ph.D. thesis, Stanford University, 329 p.

Isaacs, C. M., 1981, Porosity reduction during diagenesis of the Monterey Formation, Santa Barbara coastal area, California, in R. E. Garrison and R. G. Douglas, eds., The Monterey Formation and related siliceous rocks of California: Los Angeles, Pacific Section SEPM, 257-271.

Isaacs, C. M., 1983, Compositional variation and sequence in the Miocene Monterey Formation, Santa Barbara coastal area, California, *in* D. K. Larue and R. J. Steel, eds., Cenozoic Marine Sedimentation, Pacific Margin, U.S.A.: Los Angeles, Pacific Section SEPM, 117-132.

Kastner, M., Keene, J. B., and Gieskes, J. M., 1977, Diagenesis of siliceous oozes --I. Chemical controls on the rate of opal-A to opal-CT transformation-- an experimental study: Geochimica et Cosmochimica Acta, **41**, 1041-1059.

Merino, E., 1975, Diagenesis in Tertiary sandstones from Kettleman North Dome, California- II. Interstitial solutions: distribution of aqueous species at 100°C and chemical relation to the diagenetic mineralogy: Geochimica et Cosmochimica Acta, **39**, 1629-1645.

Merino, E., 1975, Diagenesis in Tertiary sandstones from Kettleman North Dome, California. I. Diagenetic mineralogy: Journal of Sedimentary Petrology, **45**, 1, p. 320-336.

Murata, K. J., and Larson, R. R., 1975, Diagenesis of Miocene siliceous shales, Temblor Range, California: U.S. Geological Survey Journal of Research, **3,** 553-566.

Murata, K. J., and Randall, R. G., 1975, Silica mineralogy and structure of the Monterey shale, Temblor Range, California: U.S. Geological Survey Journal of Research, **3**, 567-572.

Nobes, D. C., Murray, R. W., Kuramoto, S., Pisciotto, K. A., and Holler, P., 1992, I. Impact of silica diagenesis on physical property variations, in K. A. Pisciotto, J. C. Ingle, Jr., M. T. von Breymann, and J. Barron, eds., Proceedings of the ODP Scientific Results, Part I: Washington, D. C., NSF and Joint Oceanographic Institutions, **127**, 3-32.

O'Brien, D. K., Manghnani, M. H., and Tribble, J. S., 1989, Irregular trends of physical properties in homogenous clay-rich sediments of DSDP Leg 87 Hole 584, Midslope terrace in the Japan Trench: Marine Geology, **87**, 183-194.

Pisciotto, K. A., 1981, Diagenetic trends in the siliceous facies of the Monterey Shale in the Santa Maria region, California: Sedimentology, **28,** 547-571.

Rimstidt, J. D. and Barnes, H. L., 1980, The kinetics of silica-water reactions: Geochimica et Cosmochimica Acta, **44**, 1683-1699.

Schwartz, D. E., 1988, Characterizing the lithology, petrophysical properties, and depositional setting of the Belridge diatomite, South Belridge field, Kern County, California, *in* S. A. Graham, ed., Studies of the Geology of the San Joaquin basin: Los Angeles, Pacific Section SEPM, **60**, 281-301.

Tada, R. and Iijima, A., 1983, Petrology and Diagenetic Changes of Neogene Siliceous Rocks in Northern Japan: Journal of Sedimentary Petrology, **53**, 3, 911-930.

Tribble, J. S., Mackenzie, F. T., Urmos, J., O'Brien, D. K., and Manghnani, M. H., 1992, Effects of Biogenic Silica on Acoustic and Physical Properties of Clay-Rich Marine Sediments: AAPG Bulletin, **76**, 6, 792-804.

Williams, L. A., and Crerar, D. A., 1985, Silica Diagenesis II. General Mechanisms: Journal of Sedimentary Petrology, **55**, 3, 312-321.

Williams, L. A., Parks, G. A., and Crerar, D. A., 1985, Silica Diagenesis I. solubility controls: Journal of Sedimentary Petrology, **55**, 3, 301-311.

# CHAPTER 2

# ULTRASONIC VELOCITIES OF OPALINE ROCKS UNDERGOING SILICA DIAGENESIS


## ABSTRACT

Sonic and seismic data are commonly used in petroleum exploration. However, the large wavelength of the signals averages rock properties over a large volume. Therefore, a study interested in comparing acoustic velocity variations through highly variable diagenetic differences has to utilize ultrasonic velocity experiments to explore the smallest possible scale. Compressional- and shear-wave ultrasonic velocities were measured on dry samples from the Miocene Monterey Formation of California in different stages of silica diagenesis and at effective reservoir pressure. Experimental results show very little pressure-dependence of elastic-wave velocities in samples from two of the three reservoirs. Ultrasonic velocity variations in these samples are linear with porosity and density.

However, the properties of the three datasets separate along two trends in graphs of either acoustic impedance or elastic modulus versus porosity. When elastic moduli are normalized by those of the solid phase, the two patterns persist: one group has moduli-porosity trends very close to that of chalk, whereas the samples in the other group do not. Similarly, only the lower-porosity samples in the first group produce normalized moduli-porosity trends similar to some clean sandstones.


## INTRODUCTION

Far from sources of detrital input, most silica in deep ocean basins is in the form of siliceous microorganism shells. With diagenesis, the amorphous opal-A of these skeletons alters towards crystalline quartz, the stable phase, through an intermediate phase, opal-CT.

Most published data on the relationship between silica diagenesis and seismic velocities are from the Ocean Drilling Project. Nobes et al. (1992) present log data which identify the opal-A/opal-CT transition by a pronounced change in velocity in silica-rich samples from the Japan Sea. Similarly, Tribble et al. (1992) present both log and bench-top measurements of ultrasonic $P$-wave velocity on sea-water-saturated, well-consolidated and unconsolidated detritus-rich samples from the Japan Trench.

Pronounced physical property changes in porosity, density, and velocity often accompany silica diagenesis. Since opal-A begins as the skeletons of microorganisms, void space exists both within the grains (the body cavity of the organism) and between the grains. Because the grains can contain the first type of porosity, the total porosity of rocks composed of this material can be as great as 70%. With the change from opal-A to opal-CT, porosity decreases as much as 20% and bulk density increases (Murata and Larson, 1975; Beyer, 1987). In addition, acoustic velocities increase-- sometimes quite abruptly (Bohrmann et al., 1992; Nobes et al., 1992) A bottom simulating reflector (BSR), for example, can be seen on seismic profiles in the Pacific Ocean and the North Sea. These BSRs mark the depth of the opal-A/opal-CT boundary (Hein et al., 1978; Bohrmann et al., 1992 ). Changes in these properties also occur at the opal-CT to quartz transition.

Abrupt contrasts in porosity, density, and acoustic velocity have been noted and attributed to physical property variations caused by the opal-A/opal-CT and opal-CT/quartz transition. However, previous investigators (e.g., Tada and Iijima, 1983; Nobes et al., 1992) have noted that changes in petrophysical properties at the diagenetic transitions are more gradual in rocks with a large non-silica component. Two of the three datasets in this study have a large non-silica component.

Both seismic and sonic velocity are useful tools in petroleum exploration. However, these types of velocity data average rock properties over a broad interval. By making laboratory ultrasonic experiments on samples of known mineralogy at all stages of silica diagenesis, this study is a useful step in obtaining small-scale information about silica

diagenesis from acoustic data. This work shows that two types of porosity reduction patterns can be recognized in trends of impedance or elastic moduli, but not in ultrasonic velocity. Furthermore, the trends recognized here can be applied to well logs at any stage of silica diagenesis (Chapter 4).

## EXPERIMENTAL PROCEDURE

The three suites of core plugs are from three Miocene Monterey Formation reservoirs in the southwest San Joaquin Valley, California (Figure 1). All cylindrical samples were cut parallel to the bedding. Fourier Transform Infrared Spectroscopy (FTIR) was used to determine the mineralogy of all samples (Harville and Freeman, 1988); these values and descriptions of the methods of measuring bulk and grain density and porosity are shown in Appendix A. The samples from Cymric field traverse the opal-A/opal-CT transition, those from McKittrick field all contain opal-CT, and the samples from Asphalto field traverse the opal-CT/quartz transition. Measurements were also made on two plugs from a sample from Nevada composed of 100% opal-CT of zero porosity of hydrothermal origin.

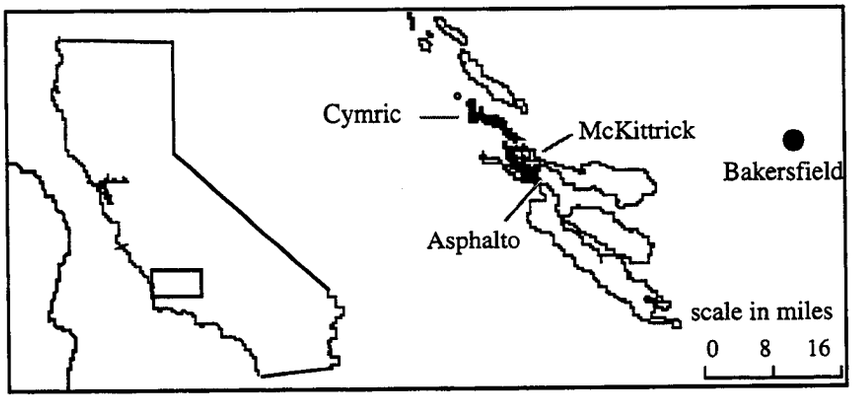


Figure 1. Sample locations.

All measurements were made on room-dry samples at atmospheric pore pressure. Ultrasonic (about 1 MHz) P- and S-wave velocities were measured by a pulse-transmission

technique at confining hydrostatic pressures up to 30 MPa. Silicone oil was used in the pressure vessel (Figure 2) to maintain hydrostatic pressure. Experimental pressures were raised to 30 MPa in most samples, but were raised to only 15 MPa in many of the Cymric samples due concern for damaging the samples. Although I recognize that the in situ pressures in the three wells is different, measurements at 15 MPa, the greatest pressure at which most measurements were made, will be frequently presented. Because increased pressure improves signal quality, waveforms are easier to interpret at higher pressures.

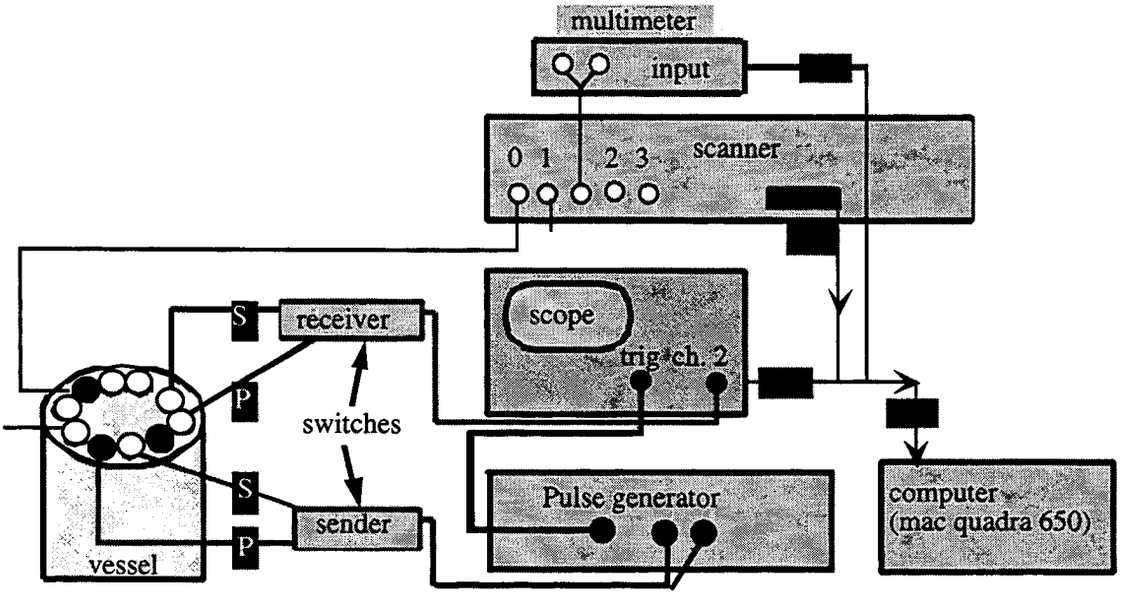


Figure 2. Experimental setup for ultrasonic velocity measurements.

Because many of the samples have large porosity, there was concern that a coupling material like honey would bias the experiment. Instead, one sheet of parrafilm was placed at either end of the sample, between it and the transducers. The experiment was repeated with two sheets of parrafilm and no sample between the transducers to determine the time necessary for the signal to go from the generator to the receiver.

Photomicrographs were taken on a five spectrometer JEOL 733 Superprobe under the operative conditions of 15 kV accelerating voltage, 15 nA beam current and 1μm beam diameter. As seen on two images from a Cymric sample subjected to a maximum pressure

of 15 MPa (Figure 3), sample deformation occurred most pervasively in those high-porosity samples. A secondary electron image (left) shows a biogenic opal-A fragment which was not damaged during the experiment, whereas a backscatter electron image (right) shows an opal-CT grain which was broken. These two images show that different minerals react differently to pressure and are consistent with laboratory tests which have shown that diatomite (opal-A) is one of the least compressible deep-sea sediments (Hamilton, 1976) while opal-CT is more brittle.

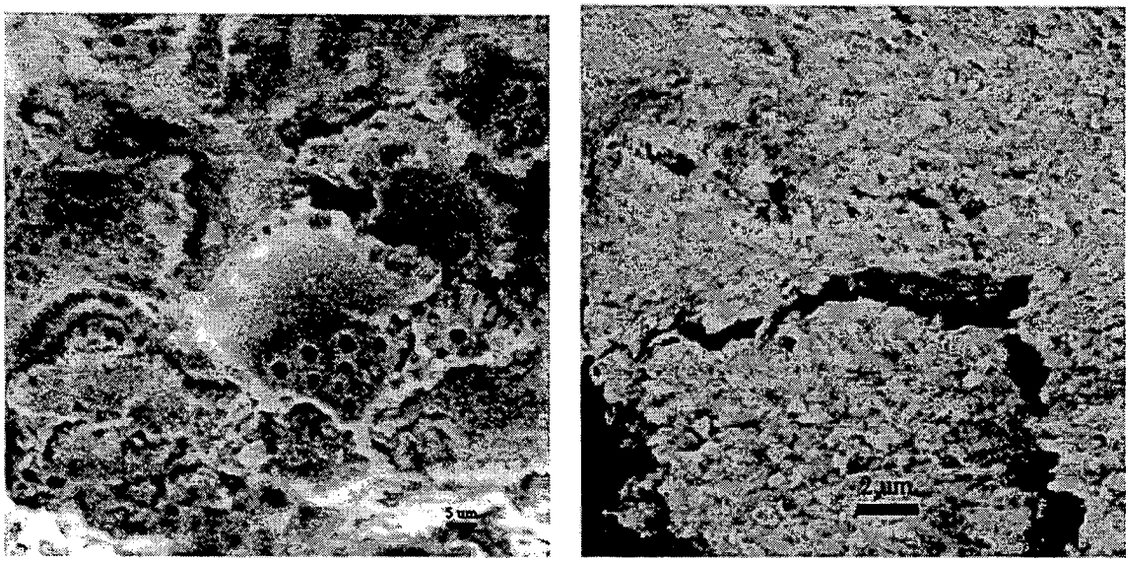


Figure 3. Microprobe images from one sample from Cymric. Left: Secondary electron image of opal-A showing well preserved diatom fossils and no sample damage. Right: Backscatter image of opal-CT grains, showing fracture caused by experiment.

The initial length of the samples was measured to either 0.001 inch or 0.1 mm; changes in length during the experiment were determined with sensors (Linear motion conductive plastic potentiometers) attached to the sample holder. These potentiometers measure length by applying a known voltage across a stretch of conducting material (here, conductive epoxy). A connector slides along the stretch of conducting material and measures voltage, which is a function of the change in sample length.

Shortening data indicate minor loading-induced grain crushing in the McKittrick and Asphalto samples (Figure 4). Measurements below 5 MPa are not shown because coupling between the sample and transducers is poor at these low confining pressures. Significant shortening did occur in the samples from Cymric where the in situ pressure (6 MPa) is less than half the maximum pressure applied. In situ reservoir pressure for the other reservoirs, however, is closer to the maximum pressures exerted during the experiment.

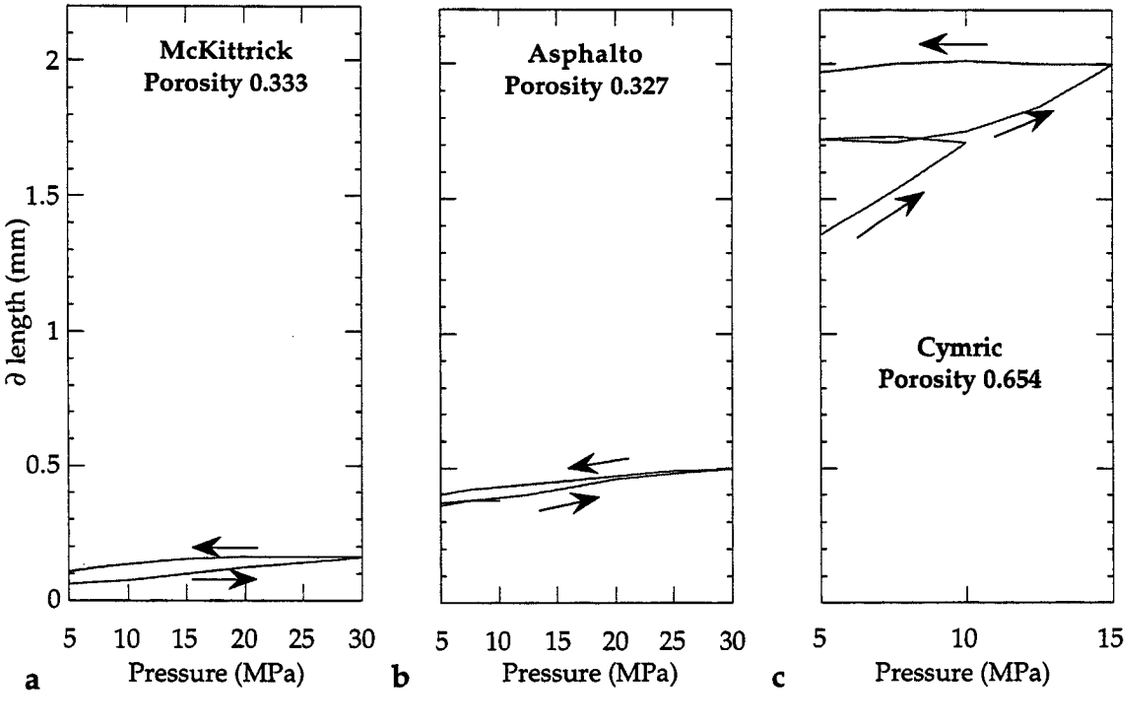


Figure 4. The change in length of a sample from (a) McKittrick, (b) Asphalto, and (c) Cymric with pressure.

Velocity was measured during both pressure loading and unloading. When differences existed between the two values, loading velocity was slower. Grain crushing and closing of microcracks may be responsible for this change in velocity. Although grains are broken at pressures exceeding reservoir pressure (e.g., Figure 3), experimental pressures near in situ conditions close microcracks induced during and after coring. Therefore, velocities at approximately in situ pressures are most applicable to reservoir conditions.

## ERROR ANALYSIS

Figure 5 shows waveforms from loading experiments at 15 MPa. Waveforms from additional experiments are shown in Appendix E. The waveforms from the three reservoirs show common results-- first arrivals are easier to recognize in samples with lower porosity, and there is much more background noise in $V_S$ than $V_P$ .

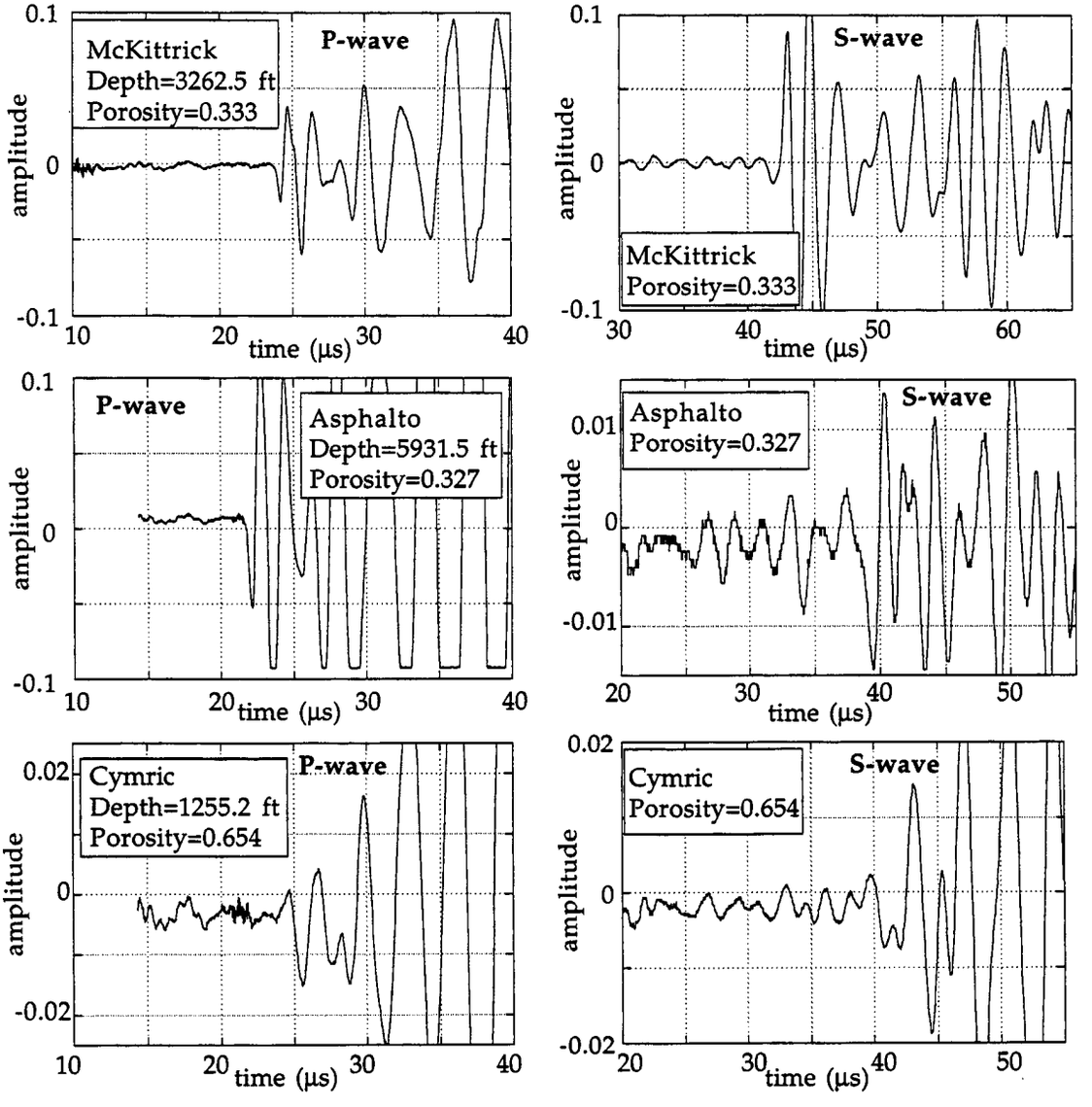


Figure 5. Loading velocity data collected at 15 MPa. Raw P- and S-waveforms shown for McKittrick, top; Asphalto, middle; and Cymric, bottom.

The poor quality of some waveforms means that the arrival of the signal may be recognized incorrectly. For example, the first shear-wave peak in the Cymric sample might be chosen at either approximately 44 or 46 μs, resulting in two calculations of shear-wave velocity. In contrast, there is little ambiguity over the $P$-wave velocity pick for the Cymric sample: the first peak is at about 25 μs.

Figure 6 shows the compressional and shear-wave velocity at 15 MPa (loading values) with error bars denoting the maximum and minimum velocities that might have been chosen from the waveforms. The error bars confirm what the waveforms in Figure 5 suggest: there is much greater confidence in low porosity samples in comparison to high porosity ones, and much greater confidence in $V_P$ than $V_S$.

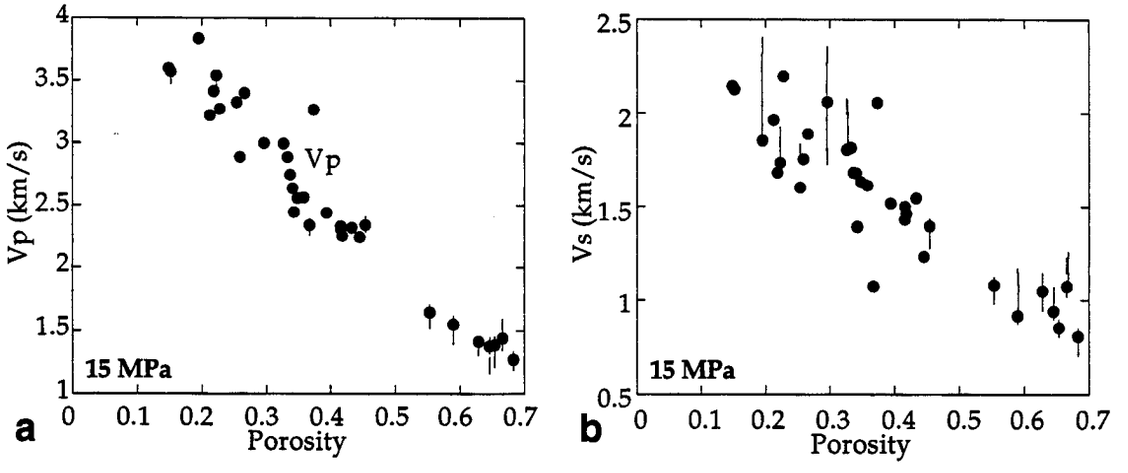


Figure 6. (a) $V_P$ and (b) $V_S$ versus porosity. Error bars shown only if ambiguity exists due to poor clarity in the waveform.

The only other source of error is variability in both the initial and incremental length measurement. Errors in the initial length measurement can arise due to rounding errors, because the sides of the core plug are not perfectly parallel, or due to an air gap between the transducers and the sample (note the difference between the change in length at 5 MPa for the Asphalto and McKittrick samples shown in Figure 4). Furthermore, uneven strain may

cause slight errors in the incremental measurements. However, the latter is even smaller than rounding errors in the initial length measurement.

The picking errors induced by noise in the waveform are much greater than the errors due to incorrect length measurements. For example, an error of 1 mm in a sample of initial length 35 mm would only cause a 2% error in velocity-- much smaller than human error introduced by incorrectly picking first arrivals. As a consequence, when the arrival of the signal is unambiguous, no error bars are shown in Figure 6.

## EXPERIMENTAL RESULTS

Ultrasonic velocity at several pressures versus porosity (Figure 7) shows both a strong linear relationship and that the elastic-wave velocities exhibit little variation with pressure. Actually, variations of velocity with pressure are significant in the high-porosity Cymric samples, most likely due to permanent sample damage. Due to concern sample damage at excessive pressures, only loading velocity data is presented. Furthermore, the linear trends between ultrasonic velocity at 15 MPa with porosity, $\phi$, and dry bulk density, $\rho_b$, (Figure 8), yield the following regressions:

$$V_P = 4.37 - 4.67\phi\,; R^2 = 0.930 \qquad V_S = 2.39 - 2.25\phi\,;\ R^2 = 0.771,$$

and

$$V_P = 0.120 + 1.67\rho_b\,; R^2 = 0.925 \quad V_S = 0.362 + 0.797\rho_b\,; R^2 = 0.755\,.$$

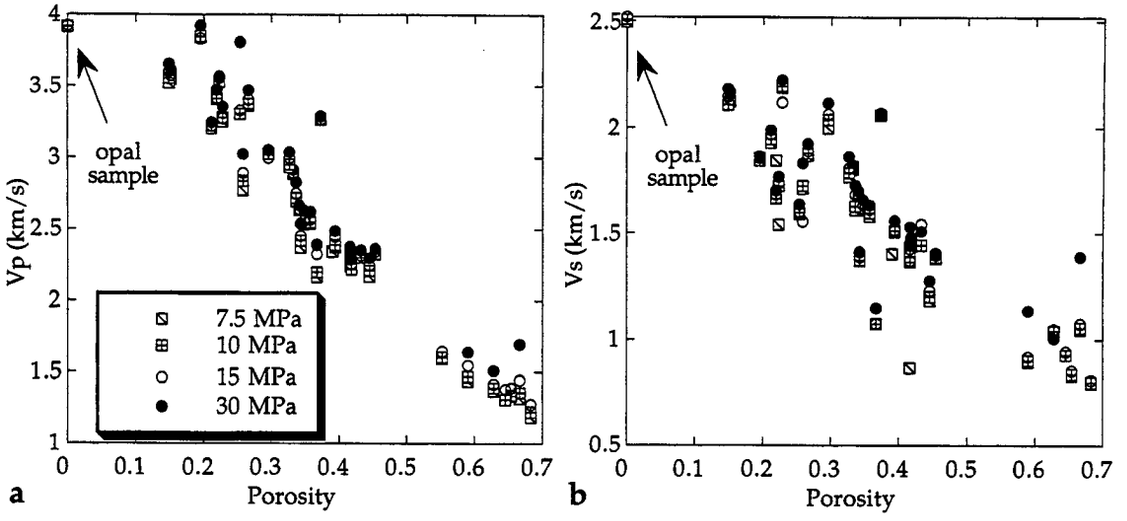


Figure 7. (a) $P$-wave and (b) $S$-wave velocity versus porosity for all dry samples at varying hydrostatic pressure. The sample with zero porosity is 100% opal-CT.

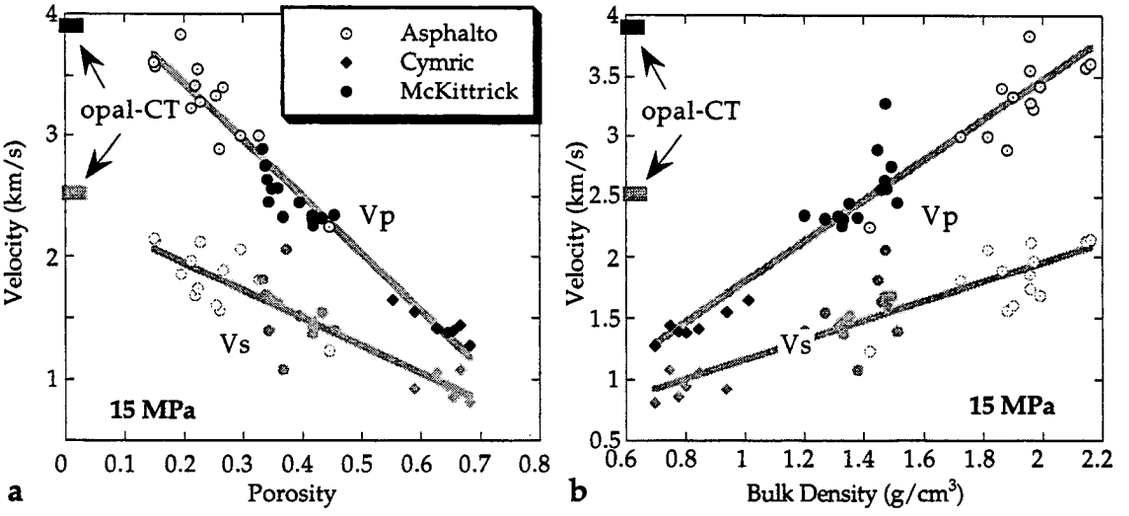


Figure 8. $V_P$ and $V_S$ versus (a) porosity and (b) dry bulk density at 15 MPa.

In the samples in this study, the relationships between velocity and porosity and velocity and density are linear. The gradual, linear trends shown in Figure 8 do not predict abrupt opal-A/opal-CT or opal-CT/quartz transitions such as those which produce BSRs in nature. A sequence with BSRs should produce stepwise functions at transition boundaries.

How can I explain this apparent disparity between our laboratory data and the widely reported BSR phenomenon?

Some siliceous sequences do not produce a BSR. These tend to be more clay rich (Nobes, et al., 1992). Monterey Formation rocks in the San Joaquin Valley are generally clay-rich (Graham and Williams, 1985). There are no known reports of a BSR in the San Joaquin Valley. The laboratory data presented here supports the idea that regions which do not produce a BSR are clay-rich rocks with gradual physical property changes.

Seismic data, however, measures contrasts in impedance (calculated $I_P = \rho V_P$ where $\rho$ is bulk density) rather than velocity. Although graphs of ultrasonic velocity versus porosity are linear, acoustic $P$-wave impedance versus porosity (Figure 9a) shows a separation of the trends described by the McKittrick and Asphalto samples. Another term commonly used for comparing velocity data is the elastic $M$-modulus, calculated $M = \rho V_P^2$ and shown versus porosity in Figure 9b. Since bulk density is the added term in these dependent variables in comparison to velocity alone, bulk density must be varying with porosity in these datasets.

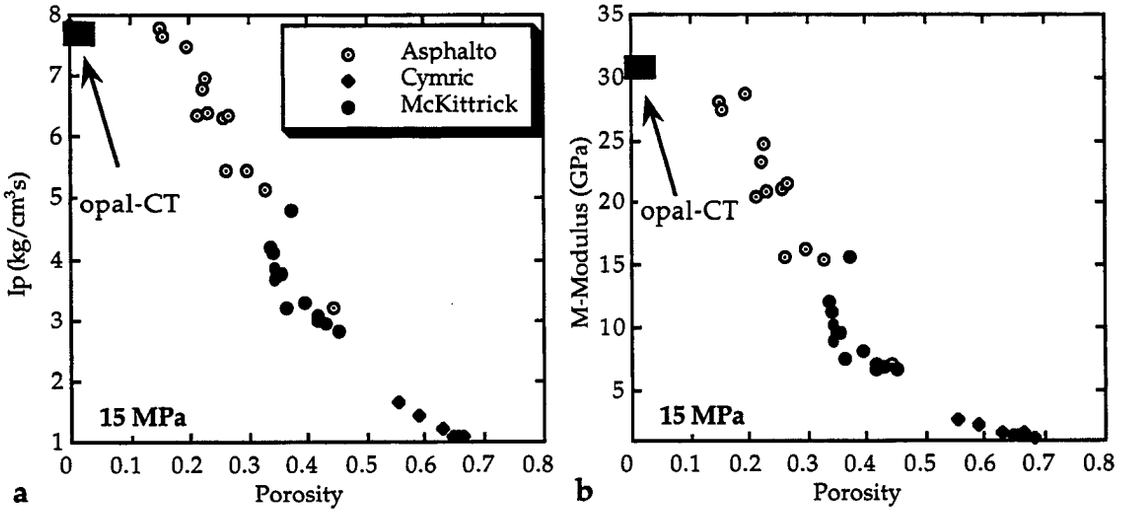


Figure 9. (a) $I_P$ and (b) $M$-Modulus versus porosity, measured at 15 MPa.

## COMPARISON WITH OTHER ROCKS

Trends of velocity versus density or porosity between Asphalto and McKittrick are linear. However, the two datasets separate when the dependent variable contains a density term, such as impedance or modulus. Chapter 1 shows that the samples from Asphalto and Cymric (Group 1) undergo porosity reduction along a different set of trends from the samples from McKittrick (Group 2). Furthermore, these two trends correspond to two textures. Group 1 is characterized by small, high surface area grains, whereas Group 2 samples are composed of interlocking, lower surface area grains. It is my assumption that these separate impedance- and moduli-porosity trends are also indicative of two textures.

One way to test this assumption is to compare the data from these Monterey Formation samples to measurements from samples with a known texture. One important characteristic for an analogous dataset is to find rocks which exist as solids at very high porosity. For example, most clastic rocks have porosity below 40%; in contrast, porosity may be as large as 60% in limestones (Nur et al., 1995).

For these comparisons, the laboratory measurements will be presented as elastic moduli. In addition to $M$-Modulus, defined above, the $G$-modulus (shear), calculated $G = \rho V_S^2$ will also be presented. Normalization of the elastic moduli by that of the solid phase (the moduli if the sample had no porosity) enables comparisons in situations with variable mineralogy or different rock types. The solid phase modulus is calculated as the Hill average of the weighted constituent minerals:

$$M_H = .5\left[\sum_{i=1}^{N} f_i M_i + \left(\sum_{i=1}^{N} \frac{f_i}{M_i}\right)^{-1}\right]$$

where $f_i$ is the volume fraction of a mineral in the solid and $M_i$ is the modulus (either $K$ or $G$) of that mineral. The density and elastic moduli of the mineralogical components are detailed in Table 1; methods are explained further in Appendix B.

Table 1. Density (rho), ultrasonic velocity, and elastic moduli of the rock-forming minerals in this study.

| | opal-A/CT | quartz | fsp $Or_{79}Ab_{19}An_2$ | Clay | carbonate (calcite) | pyrite | organics | analcime |
|---|---|---|---|---|---|---|---|---|
| rho (g/cm$^3$) | 2.0 | 2.649 | 2.56 | 2.6 | 2.712 | 5.1 | 1.3 | 2.712 |
| Vp (km/s) | 3.935 | 6.05 | 5.91 | 3.6 | 6.53 | 7.3 | 2.25 | 5.78 |
| Vs (km/s) | 2.508 | 4.09 | 3.25 | 1.85 | 3.36 | 5.2 | 1.45 | 3.11 |
| K (GPa) | 14.219 | 37.88 | 53.36 | 21.83 | 74.82 | 87.91 | 2.937 | 55.629 |
| G (GPa) | 12.580 | 44.31 | 27.04 | 8.899 | 30.62 | 137.9 | 2.733 | 26.231 |
| reference | this study | McSkimm et al., 1965 | Ryzhova, et al., 1965 | Castagna et al., 1985 | Dandekar, 1968 | Simmons and Birch, 1963 | Blangy, 1992 | Hughes and Maurette, 1957 |

Chalks are analogous to these rocks from California because both are of biogenic origin. However, while opaline rocks are made of siliceous microorganism skeletons, chalks are composed of calcareous microorganism skeletons. Because chalk is also composed of small, high surface area grains, it should be a good analogy to the Group 1 rocks. A comparison of the normalized moduli of the siliceous rocks at 15 MPa with chalk data at an effective pressure of 20 MPa (Figure 10) collected in the North Sea (Brevik, 1995) shows elastic moduli that follow similar trends, particularly between Asphalto, Cymric and the chalk. No correction was made for the different confining pressures.

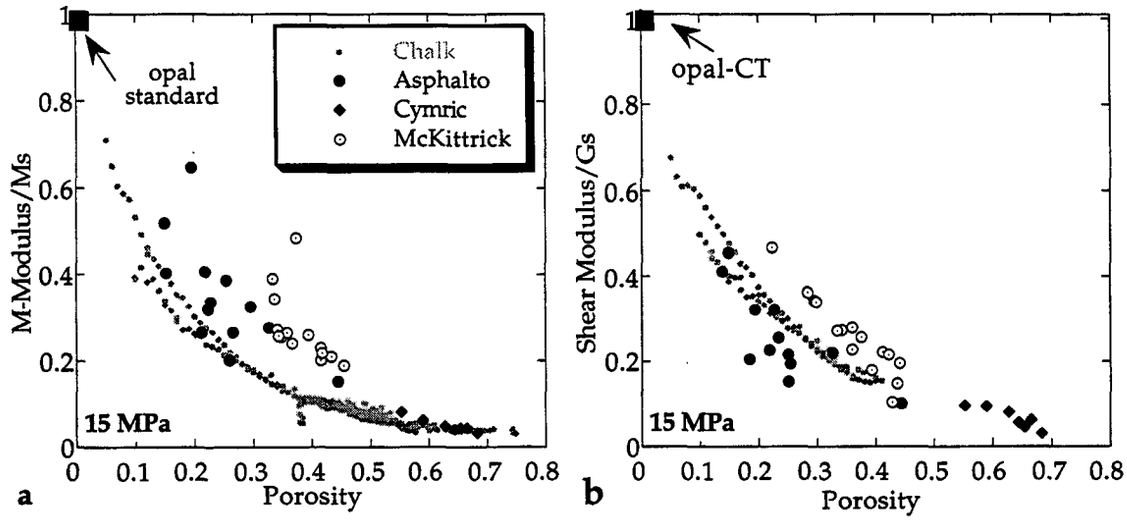


Figure 10. Normalized (a) $M$-modulus and (b) $G$-modulus of opaline rocks and chalks versus porosity.

A second comparison will be made to non-biogenic but silica-rich (clay content below 4%) sandstones (Figure 11). The sandstones are from the Troll (Blangy, 1992) and Oseberg fields (Strandenes, 1991) in the North Sea, and the Gulf of Mexico (Han, 1986). Because the sandstone grains are large and have low surface area, I expect these trends to be analogous to the Group 2 McKittrick data. The sandstone measurements were performed on dry samples at an effective pressure of 15 MPa.

In contrast to my expectations, from 20-30% porosity, the samples from Asphalto have both moduli close to those of clean Gulf and North Sea Oseberg sandstones. Furthermore, the samples from McKittrick have normalized moduli much greater than the sandstone datasets. Although this is not the expected result, the Group 2 samples from McKittrick do consistently plot along different normalized modulus-porosity trends than the Group 1 Asphalto samples.

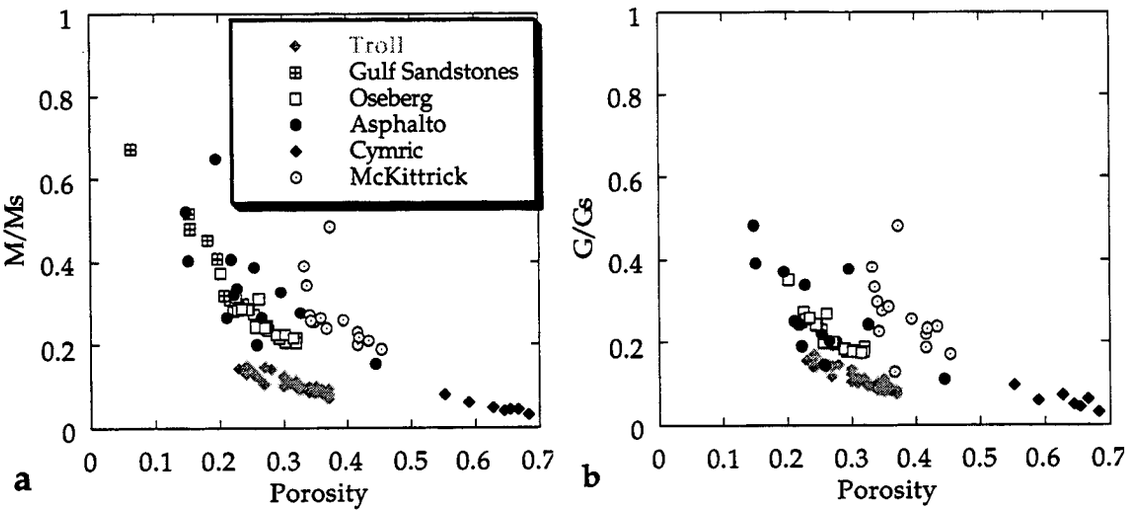


Figure 11. Normalized (a) $M$-modulus and (b) Shear-Modulus versus porosity for sandstone and opaline samples. The legend is the same in both graphs.

One goal of Chapter 1 is to identify Group 1 and Group 2 rocks by their variations in porosity, density, and mineral content. This work shows that Group 1 and Group 2 can be

One goal of Chapter 1 is to identify Group 1 and Group 2 rocks by their variations in porosity, density, and mineral content. This work shows that Group 1 and Group 2 can be separated based on their acoustic impedance or elastic moduli as well. Specifically, Group 1 has normalized elastic moduli similar to chalks whereas Group 2 does not overlap with the chalk data. Furthermore, Group 1 rocks are not likely to produce a BSR whereas Group 2 rocks may. Chapter 4 shows that these differences between Group 1 and Group 2 can be recognized not only with ultrasonic velocity data, but with sonic well log data as well.

## CONCLUSIONS

- The silica samples in this study exhibit a gradual increase in ultrasonic velocity with decreasing porosity, rather than abrupt changes due to the diagenetic transitions.
- The samples from Asphalto and McKittrick show little velocity-pressure dependence, while the samples from Cymric show some variation of velocity with pressure.
- The elastic moduli of the samples from Cymric and Asphalto (Group 1) have porosity dependence the same as chalks, whereas those from McKittrick (Group 2) have different moduli-porosity behavior.
- Between 20-30% porosity, the modulus-porosity trends of the Asphalto samples are similar to some clean sandstones.

## REFERENCES

Beyer, L. A., 1987, Porosity of unconsolidated sand, diatomite, and fractured shale reservoirs, South Belridge and West Cat Canyon Oil Fields, California, *in* Meyer, R.F., ed., Exploration for heavy crude oil and natural bitumen, **25**: Los Angeles, AAPG Studies in Geology, 395-413.

Blangy, J. P., 1992, Integrated seismic lithologic interpretation: The petrophysical basis: Ph.D. thesis, Stanford University.

Bohrmann, G., Spiess, V., Hinze, H., and Kuhn, G., 1992, Reflector "Pc" a prominent feature in the Maud Rise sediment sequence (eastern Weddell Sea): Occurrence, regional distribution and implications to silica diagenesis: Marine Geology, **106**, 69-87.

Brevik, I., 1995, Chalk data from the Tommeliten Gamma Field, paper presented at Effective Medium Workshop, University of Karlsruhe, Germany.

Castagna, J. P., Batzle, M. L., and Eastwood, R. L., 1985, Relationships between compressional and shear wave velocities in silicate rocks, Geophysics, **50**, 571-581.

Dandekar, D.P., 1968, Pressure dependence of the elastic constants of calcite: Phys. Rev., **172**, 873.

Graham, S. A. and Williams, L. A., 1985, Tectonic, depositional, and diagenetic history of Monterey Formation (Miocene), central San Joaquin Basin, California, AAPG Bull., **69**, 3, 385-411.

Hamilton, E. L., 1976, Variations of density and porosity with depth in deep-sea sediments: Journal of Sedimentary Petrology, **46**, 280-300.

Han, D.-H., 1986, Effects of porosity and clay content on acoustic properties of sandstones and unconsolidated sediments: Ph.D. thesis, Stanford University.

Hein, J. R., Scholl, D. W., Barron, J. A., Jones, M. G., and Miller, J., 1978, Diagenesis of late Cenozoic diatomaceous deposits and formation of the bottom simulating reflector in the southern Bering Sea: Sedimentology, **25**, 155-181.

Harville, D. G. and Freeman, D. L., 1988, The Benefits of Application of Rapid Mineral Analysis Provided by Fourier Transform Infrared Spectroscopy: SPE Conference Proceedings, 141-146.

Hughes, D. C., and Maurette, C., 1957, Variation of elastic wave velocities in basic igneous rocks with pressure and temperature: Geophysics, **22**, 23.

McSkimm, J. J., Andreatch, P., and Thurston, R.W., 1965, Elastic moduli of quartz versus hydrostatic pressure at 25°C and -195.8°C: J. Appl. Phys., **36**, 1624.

Murata, K.J., and Larson, R.R., 1975, Diagenesis of Miocene siliceous shales, Temblor Range, California: USGS Journal of Research, **3**, 553-566.

Nobes, D.C., Murray, R.W., Kuramoto, S., Pisciotto, K.A., and Holler, P., 1992, I. Impact of silica diagenesis on physical property variations, *in* Pisciotto, K.A., Ingle, J.C., Jr., von Breymann, M.T., Barron, J., eds., Proceedings of the ODP Scientific Results, **127,** Part I: Washington, D.C., NSF and Joint Oceanographic Institutions, 3-32.

Nur, A. M., Mavko, G., Dvorkin, J. P., and Gal, D., 1995, Critical porosity; the key to relating physical properties to porosity in rocks: Society of Exploration Geophysics, 65th annual international meeting, **65**, 878-881.

Ryzhova, T. V., Aleksandrov, K.S., 1965, The elastic properties of potassium-sodium feldspars, Bull. Acad. Sci. USSR Geophysics Series, **7**, 53.

Strandenes, S., 1991, Rock physics analysis of the Brent Group Reservoir in the Oseberg Field: Stanford Rock Physics and Borehole Geophysics Project.

Simmons, G., and Birch, F., 1963, Elastic constants of pyrite: J. Appl. Phys., **34**, 2736-2738.

Tada, R. and Iijima, A., 1983, Petrology and Diagenetic Changes of Neogene Siliceous Rocks in Northern Japan: Journal of Sedimentary Petrology, **53**, 3, p. 911-930.

Tribble, J. S., Mackenzie, F. T., Urmos, J., O'Brien, D. K., and Manghnani, M. H., 1992, Effects of biogenic silica on acoustic and physical properties of clay-rich marine sediments: AAPG Bull., **76**, 6, 792-804.

# CHAPTER 3

# ROCK PHYSICS MODELING OF ELASTIC MODULI DURING SILICA DIAGENESIS


## ABSTRACT

After porosity, $P$- and $S$-wave velocities, and mineralogy were measured in dry samples from the Miocene Monterey Formation of California, their elastic moduli were modeled using rock physics relations. Rather than bracket laboratory measurements, the aim of modeling is to closely approximate the elastic moduli. One goal of this modeling is to use the different physical assumptions which underlie the models as a tool for supporting hypotheses about the internal structure of rocks. Modeling supports the hypothesis that, in the samples studied, porosity reduction occurs along two pathways. These pathways represent two textures, where rocks composed of one microstructure contain solid grains whereas the other microstructure contains grains with such a large surface area that they behave mechanically like porous grains. The mechanical properties of this second group of rocks can be seen to be similar to that of chalks, another biogenic rock.


## INTRODUCTION

The most diagenetically unstable form of silica is amorphous opal (opal-A) which is usually produced by microorganisms as siliceous skeletal material. With burial, opal-A dissolves and alters to quartz, the stable phase, through an intermediate phase, opal-CT.

The three silica polymorphs have different petrophysical properties, of which density, porosity, and acoustic properties (velocity and elastic moduli) will be discussed here. In some environments, physical property differences among the three polymorphs are so pronounced that these properties serve as controls for identifying the dominant polymorph. For example, opal-A can sometimes be recognized solely by its high porosity, and the opal-

A/opal-CT transition can sometimes be recognized by an abrupt decrease in porosity or increase in bulk density (O'Brien et al., 1989; Guerin and Goldberg, 1996). Nobes et al. (1992) present Ocean Drilling Project (ODP) log data which clearly identifies the opal-A to opal-CT transition by a pronounced change in the slope of the velocity versus depth curve. However, in other wells in their study, Nobes et al. (1992) noticed that the opal-A/opal-CT transition could produce gradual changes in velocity, particularly in clay-rich sediments.

This chapter uses rock physics modeling to mimic the elastic moduli of samples from three reservoirs in California's San Joaquin Valley. In language borrowed from elasticity theory, the type of modeling done in this chapter is called effective medium modeling. This modeling uses idealized representations of rock texture (the arrangement of the solid and the pore space) to approximate effective elastic moduli measured in the laboratory using effective medium theories. The fit between measured and modeled values can be improved by explicitly taking into account the rock textures.

This thesis uses different arguments to illustrate that the porosity reduction patterns in siliceous rocks separate along two pathways. Each chapter presents additional methods for identifying which trends a particular dataset follow. Chapter 1 identifies the two patterns based on trends among porosity, density, and amount of various constituent minerals. Chapter 2 describes the methods and results of ultrasonic velocity measurements on dry samples from three cores, each from a different reservoir in the southwest San Joaquin Valley. The hypothesis tested in this chapter is whether the two porosity reduction patterns require two models, and if the physical basis of the models suggests that the samples in the two porosity reduction patterns have two textures. Modeling, microphotographs, and an analogy to other rocks suggest that the rocks in these two groups have different textures.

This chapter has several practical applications. For example, if an effective medium model can be found which closely approximates laboratory data, then if either porosity or elastic modulus is known, the other can be estimated. Finally, by identifying models which describe siliceous rocks under different textural and diagenetic constraints, this work

can introduce a theoretical quantitative basis for interpreting surface seismic data and well logs in this geologic environment.

## DEFINING PARAMETERS

The samples from the different porosity reduction patterns separate in graphs of either acoustic impedance of elastic moduli versus porosity even though velocity-porosity trends are linear (Chapter 2). This chapter will model elastic moduli. These moduli are $M$, the $P$-wave modulus, $G$, the shear modulus, and $K$, the bulk modulus, as defined $M = \rho Vp^2$; $G = \rho Vs^2$, and $K = M - (4/3)G$, where $\rho$ is the dry rock bulk density. The moduli predicted by different models will be compared to direct measurements (Figure 1), presented in tabulated form in Appendix D. All effective medium models operate in the modulus-porosity plane, and provide theoretical equations which connect the highest porosity point with the zero-porosity point.

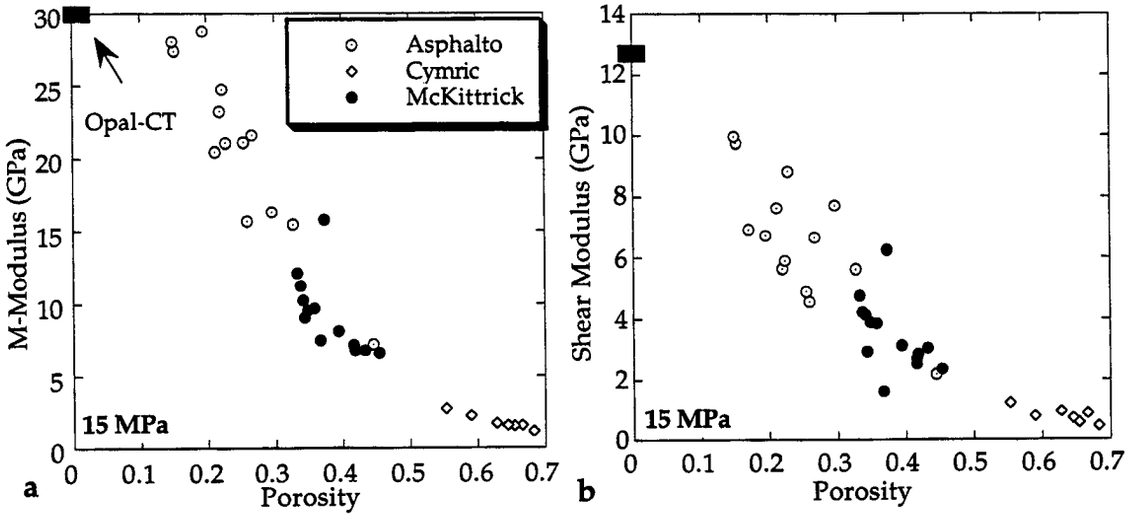


Figure 1. Dry (a) $M$ - modulus and (b) Shear modulus versus porosity.

A successful model will predict measured elastic moduli using theoretical constraints that have a reasonable physical underpinning. Because the purpose of this chapter is to reproduce laboratory measurements using different models, all data (and all models with a pressure term) will operate at the same pressure. In contrast, Chapter 4, which compares laboratory measurements to in-situ well log measurements, will use laboratory measurements at the appropriate in situ pressure.

Modeling rocks composed of more than one mineral requires calculating the moduli of the solid phase (the modulus if the sample had zero porosity) for each sample as a function of the abundance of the constituent minerals. The solid-phase moduli ( $K_s$, $G_s$ or $M_s$) is calculated according to the Hill (1952) average:

$$M_S = 0.5\left[\sum f_i M_i + \left(\sum {}^{f_i}\!/_{M_i}\right)^{-1}\right] \qquad (1)$$

where $f_i$ is the volume fraction of mineral $i$. The density, velocity, and moduli of the minerals which comprise the rocks in this study are found in Appendix B.

The mineral fractions were originally determined by weight but must be converted to volume fractions to calculate the solid phase moduli. The weight fraction of each mineral ( $w_i$) is converted to a volumetric fraction ( $v_i$) according to the formula

$$v_i = \frac{w_i}{\rho_i} \Big/ \sum_{i=1}^{n} \frac{w_i}{\rho_i},$$

where $\rho_i$ is the density of mineral $i$ at zero porosity. The weight fractions of the different constituent minerals and the solid phase moduli for all samples are shown below (Table 1).

Table 1. Porosity, (phi) bulk density, mineral abundance, and the bulk and shear modulus of the solid phase for the samples from the three reservoirs.

| DRY SAMPLE DATA FROM ASPHALTO FIELD (MINERAL ABUNDANCE IN WEIGHT FRACTION) | | | | | | | | | | | |
|---|---|---|---|---|---|---|---|---|---|---|---|
| Phi | Bulk Den g/cm$^3$ | Opal-A | Opal-CT | Quartz | Feldspar | Clay | Total carbonate | Pyrite | organ-ics | Ks (GPa) | Gs (GPa) |
| 0.219 | 1.992 | 0 | 0 | 0.548 | 0.145 | 0.22 | 0 | 0.032 | 0.04 | 26.52 | 23.08 |
| 0.266 | 1.864 | 0 | 0 | 0.7 | 0.15 | 0.13 | 0 | 0.02 | 0 | 37.44 | 32.62 |
| 0.212 | 1.970 | 0 | 0 | 0.65 | 0.14 | 0.18 | 0.01 | 0.02 | 0 | 36.53 | 30.24 |
| 0.223 | 1.958 | 0 | 0 | 0.67 | 0.12 | 0.18 | 0 | 0.03 | 0 | 36.18 | 30.82 |
| 0.152 | 2.145 | 0 | 0 | 0.46 | 0.18 | 0.31 | 0.02 | 0.03 | 0 | 34.92 | 24.85 |
| 0.17 | 1.881 | mineralogy not determined | | | | | | | | | |
| 0.149 | 2.162 | 0 | 0 | 0.423 | 0.162 | 0.296 | 0.044 | 0.034 | 0.043 | 26.43 | 20.64 |
| 0.259 | 1.882 | 0 | 0 | 0.67 | 0.13 | 0.17 | 0 | 0.03 | 0 | 36.52 | 31.15 |
| 0.327 | 1.723 | 0 | 0.146 | 0.57 | 0.096 | 0.115 | 0.022 | 0.018 | 0.035 | 25.03 | 23.03 |
| 0.254 | 1.902 | 0 | 0.186 | 0.545 | 0.105 | 0.097 | 0.013 | 0.017 | 0.029 | 24.94 | 22.16 |
| 0.195 | 1.956 | 0 | 0.464 | 0.362 | 0.074 | 0.06 | 0 | 0.012 | 0.023 | 20.21 | 18.13 |
| 0.445 | 1.421 | 0 | 0.31 | 0.446 | 0.033 | 0.132 | 0.033 | 0.014 | 0.039 | 21.06 | 19.19 |
| 0.228 | 1.961 | 0 | 0 | 0.664 | 0.126 | 0.136 | 0.012 | 0.024 | 0.036 | 28.09 | 25.91 |
| 0.296 | 1.816 | 0 | 0.321 | 0.44 | 0.057 | 0.106 | 0.038 | 0.017 | 0.025 | 22.74 | 20.48 |

| DRY SAMPLE DATA FROM MCKITTRICK FIELD (MINERAL ABUNDANCE IN WEIGHT FRACTION) | | | | | | | | | | | |
|---|---|---|---|---|---|---|---|---|---|---|---|
| Phi | Bulk Den g/cm$^3$ | Opal-A | Opal-CT | Quartz | Feldspar | Clay | Total carbonate | Pyrite | Anal-cime | Ks (GPa) | Gs (GPa) |
| 0.39 | 1.385 | 0 | 0.67 | 0 | 0.22 | 0.09 | 0 | 0.02 | 0 | 19.92 | 14.85 |
| 0.454 | 1.201 | 0 | 0.88 | 0 | 0.12 | 0 | 0 | 0 | 0 | 16.62 | 13.62 |
| 0.333 | 1.447 | 0 | 0.97 | 0 | 0 | 0.03 | 0 | 0 | 0 | 14.34 | 12.48 |
| 0.373 | 1.473 | 0 | 0.95 | 0 | 0.05 | 0 | 0 | 0 | 0 | 15.18 | 13.00 |
| 0.341 | 1.47 | 0 | 0.71 | 0 | 0.19 | 0.1 | 0 | 0 | 0 | 18.82 | 13.91 |
| 0.348 | 1.46 | 0 | 0.71 | 0 | 0.15 | 0.12 | 0 | 0.02 | 0 | 18.47 | 14.06 |
| 0.394 | 1.351 | 0 | 0.86 | 0 | 0 | 0.14 | 0 | 0 | 0 | 14.91 | 12.10 |
| 0.367 | 1.38 | 0 | 0.95 | 0 | 0 | 0.05 | 0 | 0 | 0 | 14.44 | 12.41 |
| 0.416 | 1.332 | 0 | 0.75 | 0 | 0.13 | 0.12 | 0 | 0 | 0 | 17.58 | 13.29 |
| 0.433 | 1.27 | 0 | 0.9 | 0 | 0.04 | 0.06 | 0 | 0 | 0 | 15.30 | 12.71 |
| 0.416 | 1.314 | 0 | 0.9 | 0 | 0 | 0.1 | 0 | 0 | 0 | 14.70 | 12.24 |
| 0.337 | 1.492 | 0 | 0.83 | 0 | 0.05 | 0.12 | 0 | 0 | 0 | 15.84 | 12.59 |
| 0.358 | 1.477 | 0 | 0.67 | 0 | 0.14 | 0.17 | 0.02 | 0 | 0 | 18.78 | 13.41 |
| 0.343 | 1.511 | 0 | 0.65 | 0 | 0.12 | 0.23 | 0 | 0 | 0 | 18.10 | 12.81 |
| 0.418 | 1.327 | 0 | 0.87 | 0 | 0 | 0.13 | 0 | 0 | 0 | 14.85 | 12.13 |

| DRY SAMPLE DATA FROM CYMRIC FIELD (MINERAL ABUNDANCE IN WEIGHT FRACTION) | | | | | | | | | | | |
|---|---|---|---|---|---|---|---|---|---|---|---|
| Phi | Bulk Den g/cm$^3$ | Opal-A | Opal-CT | Quartz | Feldspar | Clay | Total carbonate | Pyrite | Anal-cime | Ks (GPa) | Gs (GPa) |
| 0.666 | 0.748 | 0.53 | 0.25 | 0 | 0.08 | 0.11 | 0 | 0.01 | 0 | 16.90 | 13.49 |
| 0.628 | 0.844 | 0.25 | 0.47 | 0 | 0.10 | 0.18 | 0 | 0 | 0 | 17.30 | 12.81 |
| 0.683 | 0.697 | 0.57 | 0.28 | 0 | 0.05 | 0.0 | 0 | 0.01 | .09 | 17.23 | 14.01 |
| 0.654 | 0.775 | 0.0 | 0.77 | 0 | 0.08 | 0.15 | 0 | 0.0 | 0 | 16.66 | 12.74 |
| 0.645 | 0.802 | 0.23 | 0.49 | 0 | 0.14 | 0.12 | 0 | 0.02 | 0 | 18.23 | 13.97 |
| 0.553 | 1.010 | 0.0 | 0.78 | 0 | 0.07 | 0.15 | 0 | 0 | 0 | 16.44 | 12.65 |
| 0.59 | 0.939 | 0.0 | 0.64 | 0 | 0.13 | 0.22 | 0.01 | 0 | 0 | 18.58 | 13.04 |

Although calculating solid phase moduli is vital for effective medium modeling, approximations of mineral properties introduce some errors. For example, using the elastic properties of opal-CT for opal-A is a poor but necessary assumption. Furthermore, the physical properties of either polymorph can be quite variable. Different measurements of the density of opal-A vary from 1.9 to 2.2 g/cm$^3$ (Beyer, 1987; Corelabs) and opal-CT varies from 2.0 to 2.3 g/cm$^3$ (this study; Corelabs; Williams, pers. comm., 1997).

## DESCRIPTION OF THE HASHIN-SHTRIKMAN MODEL

The Hashin-Shtrikman model (Hashin and Shtrikman, 1963) is the foundation for all mathematical descriptions of this laboratory data. The primary value of the model is that it estimates elastic modulus within the narrowest bounds of all effective medium models which make no assumptions about grain size or shape. This model does not assume the rock is composed of spherical grains. However, one physical representation of the model is to visualize a rock composed of two fractions of material in spheres, one around the other (Figure 2). In the model, one fraction has the properties of the solid and the other fraction is either assumed to be void space or have the properties of a high-porosity sample.

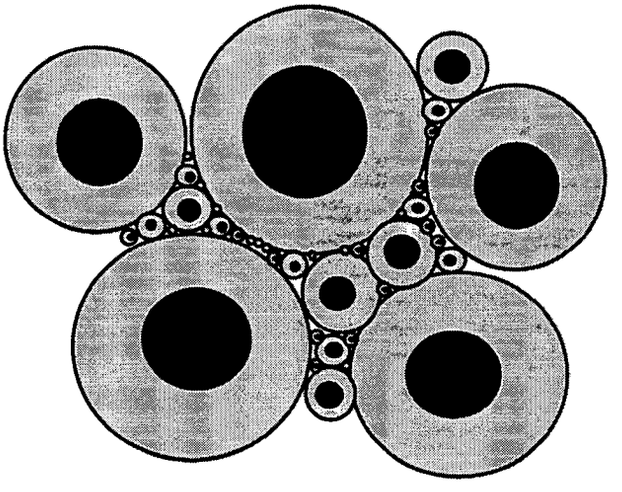

Figure 2. Physical interpretation of the Hashin-Shtrikman bounds for a two-phase material. (From Mavko et al, 1996).

The compressional and shear-wave velocities of these samples (Appendix E) exhibit a linear relationship with porosity. Linear regressions through the velocity data at 15 MPa give $V_P = 4.37 - 4.67\phi; R^2 = 0.930$ and $V_S = 2.39 - 2.25\phi; R^2 = 0.771$ where $\phi$ is porosity and $R^2$ is the correlation coefficient. These strongly linear trends indicate that sample velocity will approach zero as porosity approaches 100%. For a sample to transmit an acoustic pulse, it must be coherent; dry velocity approaches zero as the sample disaggregates. This porosity, beyond which a sample cannot exist as a solid, is termed critical porosity (Dvorkin and Nur, 1996).

These linear regressions in which velocity equals zero near 100% porosity requires one of two interpretations: (a) these samples are coherent until 100% porosity, meaning that the critical porosity is 100%, or (b) the variation in velocity with porosity is nonlinear within the range that is not sampled. In this interpretation, the velocity is zero at porosity above and equal to the critical porosity, and increases nonlinearly for some interval between critical porosity and the highest porosity documented in this study. In interpretation (a), the Hashin-Shtrikman model should be used because it connects the properties of the solid phase to those at 100% porosity (i.e., critical porosity is 100%); in (b), the modified Hashin-Shtrikman model is most appropriate because it connects the properties of the solid phase to those at a chosen critical porosity, $\phi_0$. Both models will be used; I begin with the simpler one.

The upper Hashin-Shtrikman (HS+) bound can be used to calculate the dry-rock effective bulk and shear moduli ($K_{Eff}^{UHS}$ and $G_{Eff}^{UHS}$, respectively) for any porosity between zero and 100% according to:

$$K_{Eff}^{UHS} = \left[\frac{\phi}{\frac{4}{3}G_s} + \frac{1-\phi}{K_s + \frac{4}{3}G_s}\right]^{-1} - \frac{4}{3}G_s; \quad G_{Eff}^{UHS} = \left[\frac{\phi}{Z_s} + \frac{1-\phi}{G_s + Z_s}\right]^{-1} - Z_s,$$
$$Z_s = \frac{G_s}{6}\frac{9K_s + 8G_s}{K_s + 2G_s}; \quad M_{Eff}^{UHS} = K_{Eff}^{UHS} + \frac{4}{3}G_{Eff}^{UHS}. \qquad (2)$$

where $K_s$ and $G_s$ are the solid phase moduli as shown in Table 1. Direct measurements and the HS+ bound for each sample (Figure 3) show that the upper Hashin-Shtrikman bound overestimates the $M$-modulus by an average of 40%, 44%, and 78% in the samples from McKittrick, Asphalto, and Cymric, respectively. The lower Hashin-Shtrikman bound is not shown because it calculates both moduli as approximately zero until porosity is almost zero.

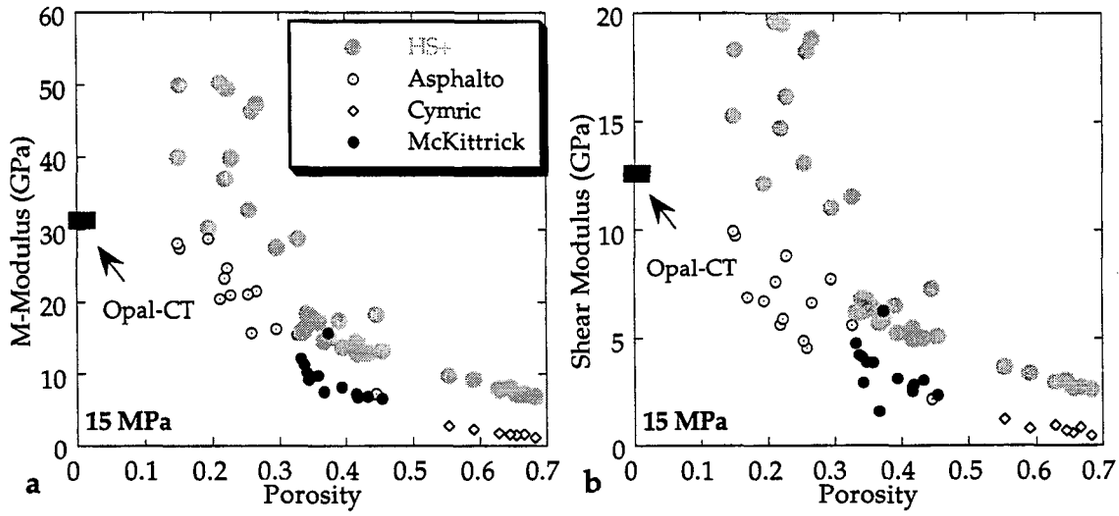


Figure 3. Upper Hashin Shtrikman (HS+) bounds and direct measurements for (a) $M$-modulus and (b) Shear modulus.

One purpose of the rock physics modeling is to infer the microstructure of the rocks using different theoretical models. Therefore, rather than using the models to bracket the elastic moduli, I attempt to replicate the laboratory values using the theoretical models. As a consequence of these goals, the Hashin-Shtrikman bounds are not sufficient. Therefore, I will use the modified Hashin-Shtrikman model next. The modified Hashin-Shtrikman bound is calculated assuming a critical porosity, $\phi_0$, that is less than 100%.

The modified Hashin-Shtrikman model connects the properties of a rock from its greatest porosity (where moduli are zero) to the solid-phase modulus at zero porosity. Estimation of the high porosity point, the critical porosity, is somewhat ambiguous. However, since the highest porosity sample from Cymric has a porosity of 68%, critical porosity must be greater than that value if one set of physical models can describe all samples. Contact cementation theory can be used to connect the moduli of the highest porosity sample (initial porosity) to critical porosity when the change in elastic modulus with porosity is non-linear between the two points. Therefore, contact cement theory (Digby, 1981; Dvorkin and Nur, 1996) will be used to estimate critical porosity.

## DESCRIPTION OF CONTACT CEMENT THEORY

In contact cement theory, the rock begins as an aggregate of loose particles of opal which are lithified by overgrowths of shells of silica cement. For this theory, I assume that the starting framework of opal is a pack of identical spherical grains with critical porosity $\phi_0$ and average number of contacts per grain $n$. Adding opal cement to the grains reduces porosity and increases the elastic moduli of the aggregate.

This is an imperfect model for opaline rocks for several reasons. First, this model suggests that lithification is occurring through overgrowth cements, where in reality, the rock is actually recrystallizing. Second, this model has a liability because the elastic moduli of 100% opal-A is not known, and so both opal-A and opal-CT have identical elastic properties in this, and all other approximations. While the second problem could be eliminated with additional raw data, the first issue remains.

The physical representation of contact cement theory, (Figure 4a) is more accurate for clastic rocks and overgrowth cements than chemical precipitates like opaline rocks. Since the value of the contact cementation model is descriptive, it is worthwhile to visualize the model according to a physical representation which can be adapted better to chemical precipitates. Initially, I will explain this model both using the original language of contact

cement theory with the language adapted here for rocks formed chemically in parenthesis. This adapted terminology is imperfect, however; I continue with this exercise because the purpose of this model is not to accurately model the change in elastic properties due to silica diagenesis, but to connect the properties at initial porosity to some critical porosity ($\phi_0$) and thereby choose $\phi_0$.

Visualize the initial grains in an unlithified rock as small particles of opal-A where the particle contacts have small cross-sectional areas. Rather than forming overgrowth cements like clastic rocks, these opaline particles dissolve and reprecipitate as opal-CT (Williams, et al., 1985). Since the amount of opal-CT increases through a combination of nucleation and growth (Williams, et al., 1985), some new particles will form and some particles will grow. Both of these processes, particularly the second, will result in particle contacts with larger cross-sectional areas. And, since both the "grains" and "cement" in this model are both composed of opal-CT ($K_s$ = 14.195 GPa, $G_s$=12.580 GPa), the physical representation can be adapted to describe changing elastic properties due to growing opaline particles.

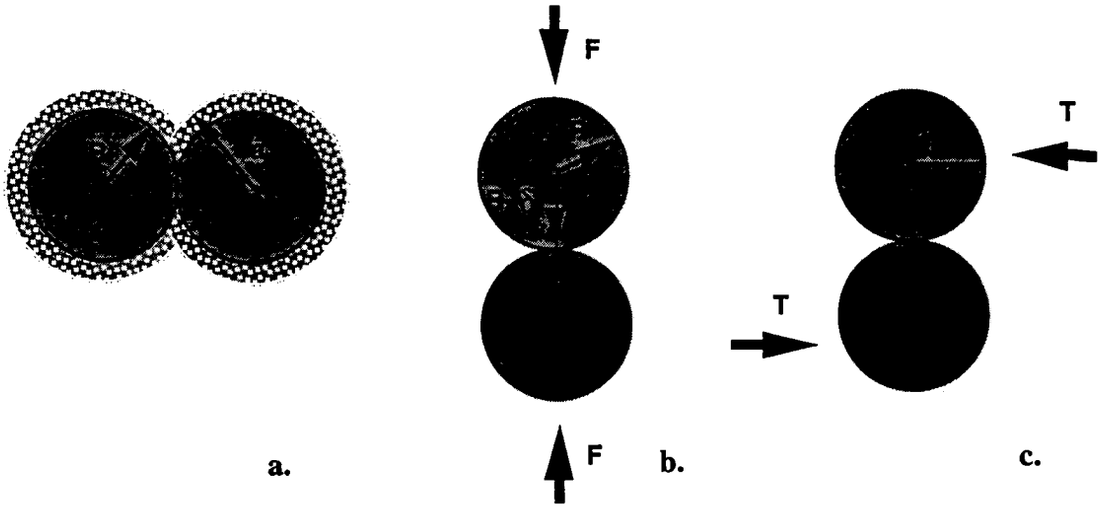


Figure 4. Cartoon describing the contact cementation model including (a) cement growth and the (b) normal and (c) tangential contact stiffness of a two-particle combination. (Adapted from Mavko et al., 1996.)

In contact cement theory the effective dry-rock bulk ($K_{eff}$) and shear ($G_{eff}$) moduli are:

$$K_{eff} = \frac{1}{6} n(1-\phi_0) M_c S_n, \quad G_{eff} = \frac{3}{5} K_{eff} + \frac{3}{20} n(1-\phi_0) G_c S_\tau,$$

where $M_c$ and $G_c$ are the compressional-wave and the shear moduli of the cement, respectively. Parameters $S_n$ and $S_\tau$ are proportional to the normal and shear stiffness, respectively, of a cemented two-grain combination, and their derivation will be shown below. As illustrated in Figures 4b and 4c, the stiffness, where $S_n = \partial F / \partial \delta$ and $S_\tau = \partial T / \partial \tau$, depends on the amount of the contact cement (the increased cross-sectional area of the particle contacts due to particle growth) and on the properties of the cement and grains (both of which are opal).

The amount of the new particle growth can be expressed through the ratio of the radius of the more mature particle $\alpha$ to that of the original particle $R$: $\alpha = a / R$ (Figure 4a). If opal-CT is evenly precipitated on the original particle surface, then at porosity $\phi$:

$$\alpha = [\frac{2}{3} \frac{(\phi_0 - \phi)}{(1-\phi_0)}]^{0.5}.$$

Finally, parameters $S_n$ and $S_\tau$ are:

$$S_n = A_n(\Lambda_n)\alpha^2 + B_n(\Lambda_n)\alpha + C_n(\Lambda_n), \quad S_\tau = A_\tau(\Lambda_\tau, \nu)\alpha^2 + B_\tau(\Lambda_\tau, \nu)\alpha + C_\tau(\Lambda_\tau, \nu);$$

$$A_n(\Lambda_n) = -0.024153 \cdot \Lambda_n^{-1.3646}, B_n(\Lambda_n) = 0.20405 \cdot \Lambda_n^{-0.89008}, C_n(\Lambda_n) = 0.00024649 \cdot \Lambda_n^{-1.9864};$$

$$A_\tau(\Lambda_\tau, \nu) = -10^{-2} \cdot (2.26\nu^2 + 2.07\nu + 2.3) \cdot \Lambda_\tau^{0.079\nu^2 + 0.1754\nu - 1.342},$$

$$B_\tau(\Lambda_\tau, \nu) = (0.0573\nu^2 + 0.0937\nu + 0.202) \cdot \Lambda_\tau^{0.0274\nu^2 + 0.0529\nu - 0.8765},$$

$$C_\tau(\Lambda_\tau, \nu) = 10^{-4} \cdot (9.654\nu^2 + 4.945\nu + 3.1) \cdot \Lambda_\tau^{0.01867\nu^2 + 0.4011\nu - 1.8186}.$$

$$\Lambda_n = [2/(\pi)][(1-\nu)^2/(1-2\nu)], \Lambda_\tau = 1/\pi.$$

In these formulas, $\nu$ is the Poisson's ratio of opal.

Figure 5 shows this model at critical porosity of both 70% and 80% and the modified upper Hashin-Shtrikman model for pure opal at critical porosity of 70% (Equation 3, below). The modified upper Hashin-Shtrikman line for pure opal at $\phi_0$= 80% is not shown because the line fits the data much poorer than at $\phi_0$= 70%. Only the experimental data from McKittrick and Cymric are shown because they are primarily composed of opal, whereas the samples from Asphalto are primarily quartz phase. From this exercise, I choose a critical porosity of 70%.

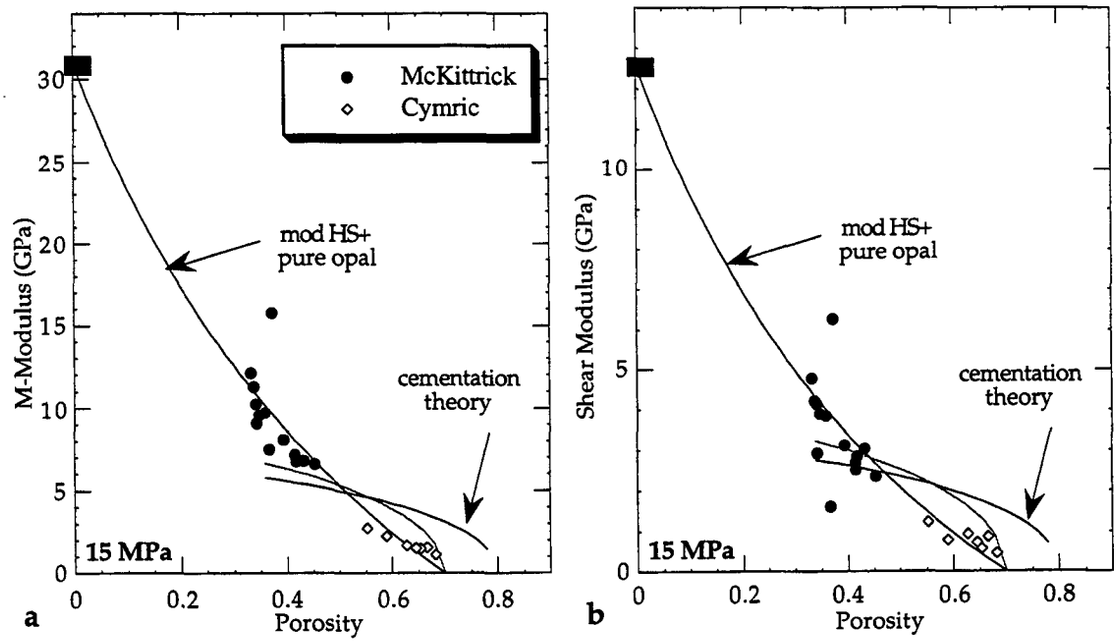


Figure 5. (a) $M$-modulus and (b) Shear modulus of the McKittrick and Cymric samples versus porosity, the modified HS+ bound for opal, and the cementation theory model where critical porosity is 70% and 80%.

## MODIFIED HASHIN-SHTRIKMAN MODEL AND EXPERIMENTAL DATA

At porosity $\phi$ between zero and critical porosity ($\phi_0$), the dry-rock effective bulk and shear moduli can be calculated with the modified upper Hashin-Shtrikman bound:

$$K_{Eff}^{UHS} = [\frac{\phi/\phi_0}{K_0 + \frac{4}{3}G_s} + \frac{1-\phi/\phi_0}{K_s + \frac{4}{3}G_s}]^{-1} - \frac{4}{3}G_s; \quad G_{Eff}^{UHS} = [\frac{\phi/\phi_0}{G_0 + Z_s} + \frac{1-\phi/\phi_0}{G_s + Z_s}]^{-1} - Z_s,$$
$$Z_s = \frac{G_s}{6}\frac{9K_s + 8G_s}{K_s + 2G_s}; \quad M_{Eff}^{UHS} = K_{Eff}^{UHS} + \frac{4}{3}G_{Eff}^{UHS}. \tag{3}$$

Similarly, the lower bounds for the dry-rock effective bulk and shear moduli are found using the modified lower Hashin-Shtrikman (mod HS-) bound:

$$K_{Eff}^{LHS} = [\frac{\phi/\phi_0}{K_0 + \frac{4}{3}G_0} + \frac{1-\phi/\phi_0}{K_s + \frac{4}{3}G_0}]^{-1} - \frac{4}{3}G_0; \quad G_{Eff}^{LHS} = [\frac{\phi/\phi_0}{G_0 + Z_0} + \frac{1-\phi/\phi_0}{G_s + Z_0}]^{-1} - Z_0,$$
$$Z_0 = \frac{G_0}{6}\frac{9K_0 + 8G_0}{K_0 + 2G_0}; \quad M_{Eff}^{LHS} = K_{Eff}^{LHS} + \frac{4}{3}G_{Eff}^{LHS}. \tag{4}$$

Once again, the modified lower Hashin-Shtrikman bound will not be calculated at this time because the calculated moduli will be zero until porosity is almost zero.

Equation (3) is used to calculate the modified upper Hashin-Shtrikman bounds (mod HS+) for all samples where critical porosity is 70% (Figure 6); in other words, $K_0, G_0 = 0$ and $\phi_0 = 0.70$. The average percent difference between the $M$-Modulus measured and modeled $(M_{meas} - M_{\text{mod}})/M_{\text{mod}}$ using the modified upper Hashin-Shtrkman bound is 30% for the 13 samples from Asphalto, 28% for the seven samples from Cymric, and 9% for the 14 samples from McKittrick. All of these fits are an improvement over the original upper Hashin-Shtrikman bound. However, the modified upper Hashin-Shtrikman model appears to only fit the samples from McKittrick well.

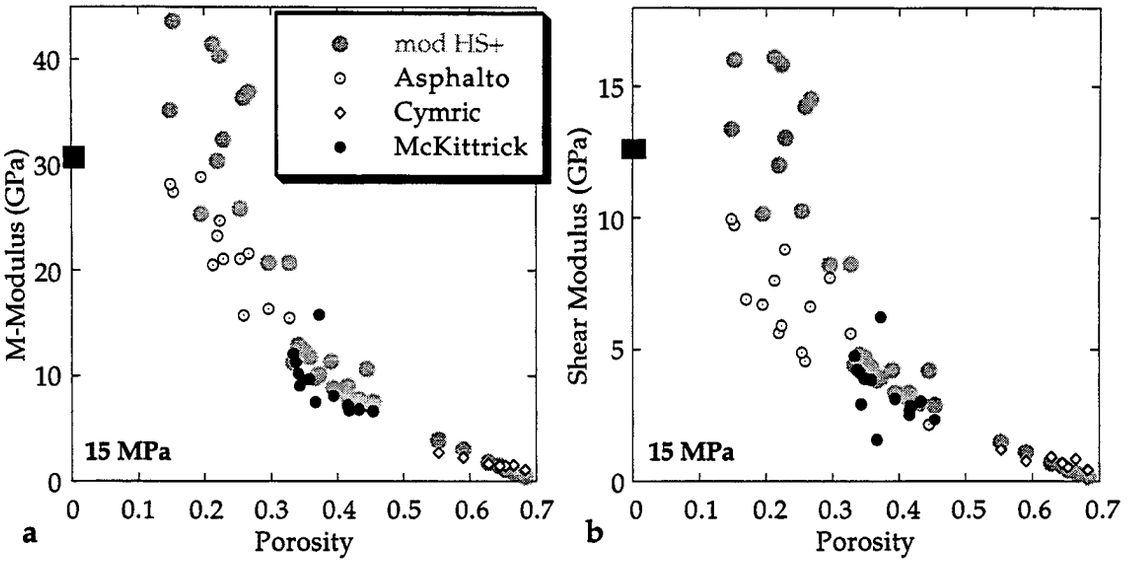


Figure 6. Measured elastic moduli and the modified upper Hashin-Shtrikman bounds for the (a) $M$ -modulus and (b) Shear Modulus.

There are two facts and one hypothesis why the model fits the data from McKittrick better than that from the other two reservoirs. Because the samples from McKittrick have a fairly homogeneous, opal-CT-rich composition (Table 1), there is more clustering in both the measured and modeled data. Furthermore, there may be large potential errors in the measurements on the samples from Cymric (see Chapter 2); the high porosity of the samples was responsible for poor waveforms, and therefore larger errors in determining velocity. My hypothesis is that the samples from Cymric and Asphalto have a different texture from the McKittrick samples, and that the differences is significant enough for the modified upper Hashin-Shtrikman model to be inappropriate. If the hypothesis is true, than use of another model will improve the fit between modeled and measured values. I will return to modeling the data from Asphalto and Cymric after discussing the robustness of this model for approximating the moduli for the McKittrick samples.

One way to test the robustness of the mod HS+ model in approximating the elastic moduli of the samples from McKittrick is to re-calculate the bound with less sample

information. Specifically, I substitute the moduli of opal-CT for $K_s$ and $G_s$ of all samples. These samples contain an average of 76% opal-CT; this test will see how much the non-opal-CT minerals affect elastic properties. Equation (3) can be used to connect the properties of solid opal ( $K_s$ = 14.195 GPa, $G_s$=12.580 GPa) to a modulus of zero at critical porosity. In Figure 5, the data from McKittrick are shown with the modified upper Hashin-Shtrikman bound for pure opal. The overlap of the modeled and measured values suggests that this model can be used to approximate the elastic moduli of opal-CT-rich samples from McKittrick or elsewhere.

Another method by which to assess the robustness of this model for describing the acoustic properties of the samples from McKittrick is to calculate other sample properties, such as the $V_P$ / $V_S$ ratio or Poisson's ratio, from the elastic moduli. The results are mixed: the percent error between measured and modeled values for Poisson's ratio and $V_P$ / $V_S$ ratio (Figure 7) are 22% and 5%, respectively. Since the error between measured and modeled $M$-Modulus was 9%, these graphs show that Poisson's ratio is extremely sensitive to small errors.

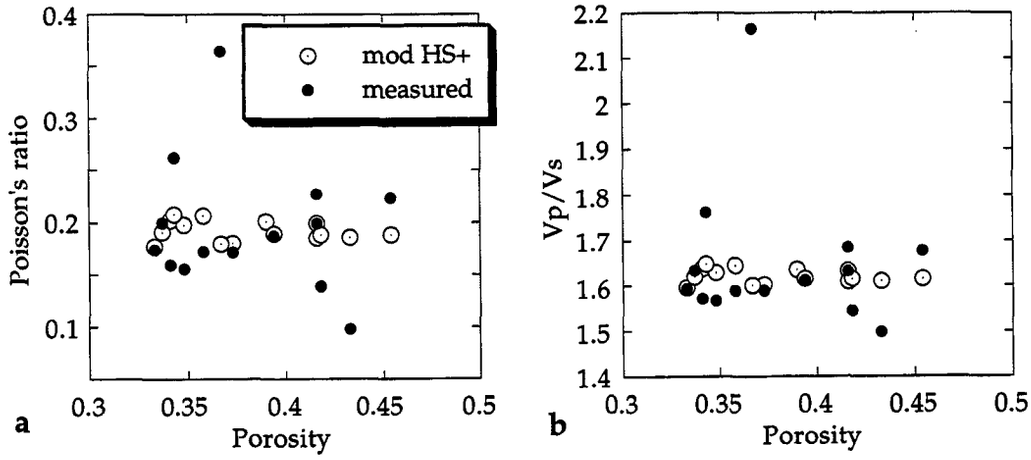


Figure 7. The measured data from McKittrick field and the (a) Poisson's ratio and (b) Vp/Vs ratio as predicted using the modified upper Hashin Shtrikman bound.

## Porosity Correction for Asphalto and Cymric

This thesis shows that porosity reduction occurs along one set of trends in the samples from Cymric and Asphalto and along another set of trends in the samples from McKittrick. This chapter argues that the elastic moduli of the different samples can be used to confirm that the two porosity reduction patterns result in rocks with different textures (arrangements of solid and pore space). Specifically, the samples from Cymric and Asphalto have high-surface area grains whereas the samples from McKittrick have low-surface area grains. This argument will be offered with both mechanical and physical evidence. The mechanical evidence will be offered first, through an analogy to chalk.

Chalks are rocks composed of calcareous microorganism skeletons, much like diatomite is a rock composed of siliceous (opal-A) microorganism skeletons. Both rocks have void spaces both between and within the grains; the porosity within the grains is the volume formerly occupied by the organic material of the microorganisms. Recognition that porosity exists within grains is important because hollow grains produce different moduli-porosity trends than do solid grains. After all, a rock composed of a random pack of solid spheres has mechanical properties near-identical to a rock composed of a random pack of hollow spheres. As a result, to model this type of rock, the porosity much be adjusted to reflect only the porosity between grains. This type of porosity correction was used by Nur et al., (1998) in modeling foam.

To compare siliceous and calcareous rocks, (Figure 8) the $M$- and shear modulus of each sample is normalized by its solid phase modulus. The chalk data, courtesy of Phillips Petroleum, is well log data from the North Sea. All data represent dry measurements. The effective pressure in the chalk data is about 30 MPa; the siliceous data from California is still presented at 15 MPa.

The Asphalto samples plot within the cloud of chalk data; the samples from McKittrick do not. Similar moduli between Asphalto and chalks suggest that both contain high surface area particles whereas the samples from McKittrick contain particles with much lower

surface area. Although the rocks from Asphalto do not contain hollow grains, Figure 8 suggests that, like chalk, some pore volumes in the Asphalto samples have an almost negligible impact on elastic modulus. Therefore, as if modeling rocks composed of hollow grains, the porosity of the Asphalto samples should also be corrected to reflect only the larger pore volumes.

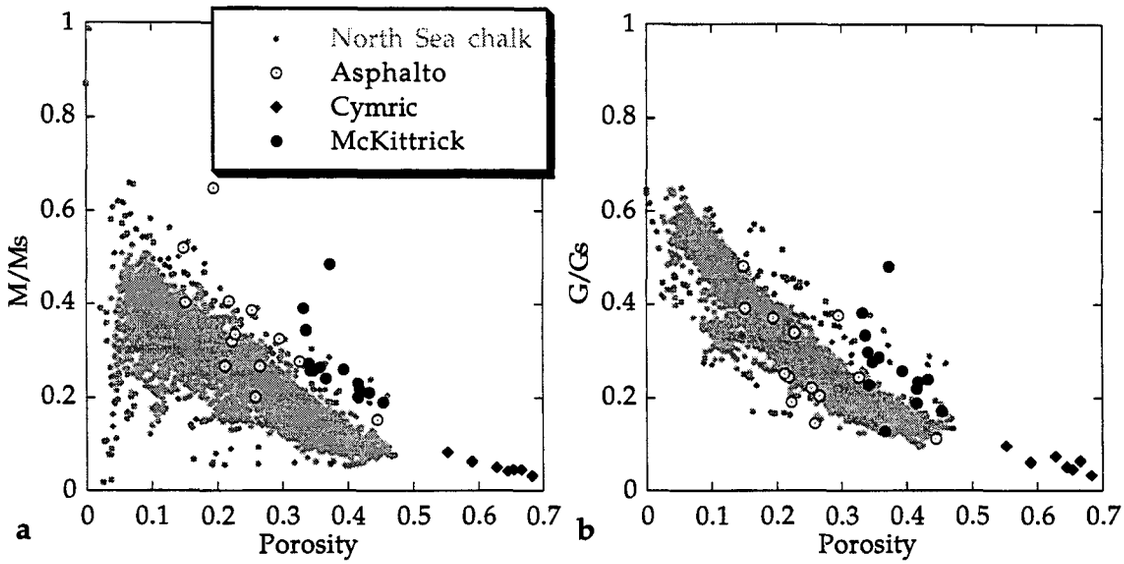


Figure 8. (a) $M$-modulus and (b) Shear modulus normalized by the moduli of the solid phase for the rocks in this study and chalks from the North Sea.

Although the porosity of the Cymric samples does not overlap with the chalk data, intuition suggests that the samples from Cymric are more likely than the other two datasets to have high surface area grains and also require this porosity correction. First, this analogy was initiated due to the similar textures of chalk and diatomite, since both are rocks composed of hollow microorganism skeletons. Since the samples from Cymric contain the only opal-A in this study, those samples are the only rocks which could be called diatomite. Furthermore, the samples from Cymric are the shallowest, have the highest porosity, and are the least diagenetically altered of the three siliceous datasets. Secondary electron

microprobe microphotos of a sample from Cymric (Figure 9) show the existence of high surface area grains. By analogy to the samples from Asphalto, the small pore volumes in the Cymric samples also should not have a large impact on elastic moduli.

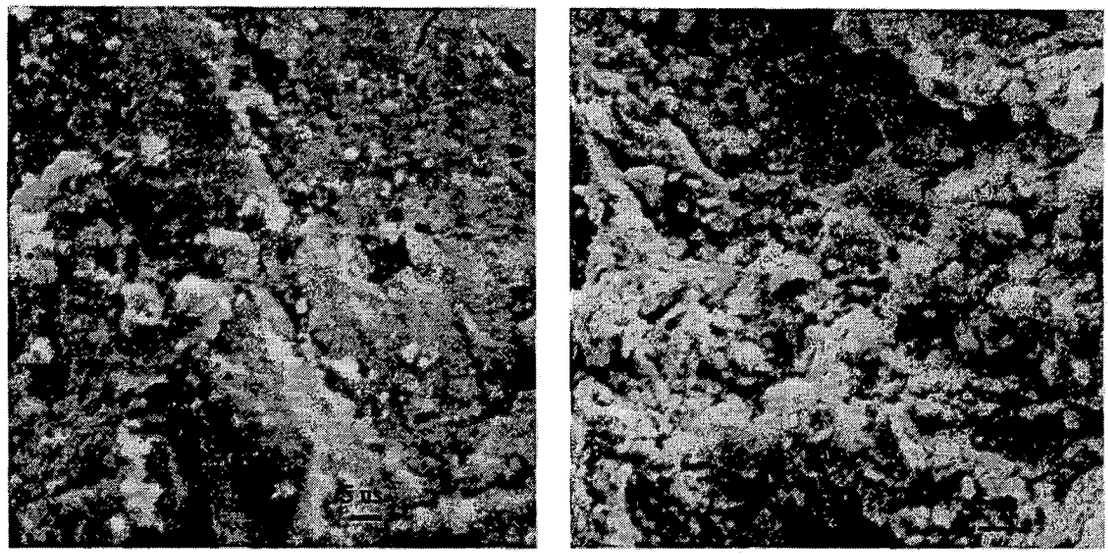

Figure 9. Secondary electron images of one sample from Cymric (porosity = 0.553) with (left) low surface area and (right) high surface area textures. Both scale bars are 5μm.

Figure 10 is a schematic cartoon of the textures in Figure 9.

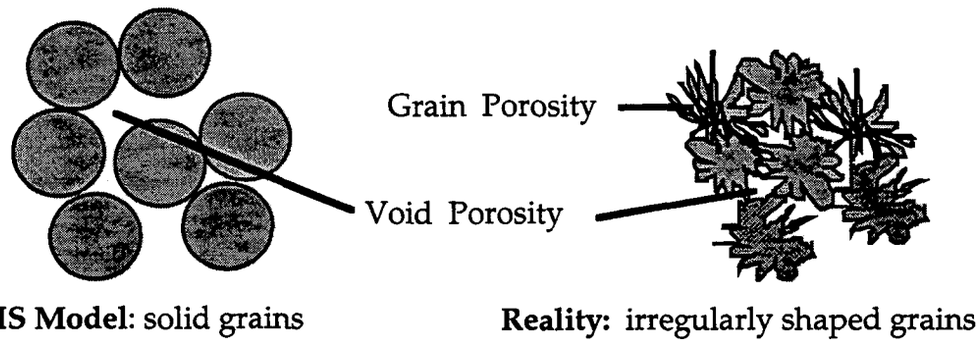


Figure 10. Textures shown in Figure 9.

Changes in the texture of opal-CT with maturity (e.g., Williams et al., 1985) may explain some textural differences between the samples from Cymric and McKittrick. Opal-CT often initially forms lepispheres, small clusters of crystals about 10 μm wide, giving early-formed opal-CT a lumpy texture (Figure 9, right) with a very large surface area to volume ratio. With continued diagenesis, opal-CT may look more like the photo on the left: smoother, with larger crystals, and a smaller surface area to volume ratio. Because these samples from McKittrick are at least 300 feet below the opal-A/opal-CT transition, they are more mature than those from Cymric, and are likely to have the texture on the left.

## Modified porosity

Although both grain packs in Figure 10 have large pore volumes between the grains (void porosity, $\phi_v$), only the diagram on the right has small pore volumes caused by irregular grain surfaces (grain porosity, $\phi_g$). As suggested by the two photomicrographs from Cymric, there will be some low surface area grains in all datasets; the question is whether or not high-surface area grains exist.

The physical and mechanical arguments suggest that the Cymric and Asphalto samples retain high surface area textures whereas the samples from McKittrick do not. Chalks are composed of hollow grains where pore volumes inside the grains have a minor impact on elastic properties. By analogy to the chalk, the samples from both Asphalto and Cymric have a fraction of pore volume which also does not significantly soften the rock (decrease elastic modulus). Therefore, effective medium modeling requires separating porosity into $\phi_v$ and $\phi_g$ where the elastic modulus is only a property of the large pore spaces (void porosity). This type of porosity correction has a precedent; Nur et al., (1998) use this procedure to calculate $K_g$ and $G_g$ for foam.

In modeling the behavior of the samples from Asphalto and Cymric, I first choose grain porosity, $\phi_g$. As shown in Figure 10, grain porosity is the fraction of the solid volume which contains small pore spaces. In contrast to $\phi_v$, the larger pore volumes between the

grains, grain porosity is much less significant in determining the stiffness of the rock. Void porosity is calculated from grain porosity. First, the rock is separated into porosity, $\phi$, and the solid fraction, $f_{solid} = 1 - \phi$. However, the high surface area solid takes up additional volume: $V_{solid} = 1 - \phi_v$. These two fractions exist such that

$$f_{solid} = V_{solid}(1 - \phi_g). \tag{5}$$

Substituting the definition of $V_{solid}$ into Equation (5) gives

$$\phi_v = 1 - \frac{1 - \phi}{1 - \phi_g} \tag{6}$$

where $\phi_g$ will vary depending on the microstructure of the rock.

However, because this model uses "modified minerals"-- minerals which take up extra volume due to the existence of grain porosity, the solid-grain moduli, $K_s$ and $G_s$, need to be recalculated. Calculating the modified-solid moduli, $K_g$ and $G_g$, at the given $\phi_g$ requires an upper Hashin-Shtrikman interpolation between the solid-grain moduli at zero porosity and an elastic moduli of zero at critical porosity $\phi_o$=1 (Equation 2). In this interpolation, the values where porosity is $\phi_g$ are the modified-solid moduli.

After calculating $K_g$ and $G_g$ at $\phi_g$, a new $Z_s$ is calculated for the new solid grain endmember, and the mod HS+ bounds are calculated Equation (3) using $\phi_v$ for porosity and moduli of zero at critical porosity of 70%. Using a non-zero $\phi_g$ increases the moduli calculated with the model because the moduli increases with decreasing effective porosity. Therefore, this exercise was first done conservatively, using $\phi_g$=0.1 for the samples from both Asphalto and Cymric. The modeled values overestimate the measured values, with an average percent difference of 36% and 26% for the reservoir rocks from Asphalto and Cymric, respectively. Since the average percent errors were 30% and 28% for the samples

from Asphalto and Cymric using the initial modified Hashin-Shtrikman model, the added complexity of the modified porosity concept does not improve modeling. However, another aspect of the physical constraints must be added to any model involving the samples from Cymric-- dependence of modulus on pressure.

**Pressure dependence**

One important difference between the samples from Cymric and the others is that the velocity of only the Cymric samples is greatly affected by pressure. Therefore, pressure-dependence is introduced by combining the modified Hashin-Shtrikman bounds with the porosity correction and a pressure-dependent model: Hertz-Mindlin (Mindlin, 1949). The pressure dependence of the samples from Asphalto is minor (see Chapter 2 or Appendix D), but introduction of pressure dependence will be attempted with these samples as well.

Hertz-Mindlin theory calculates the elastic moduli caused by exerting a given pressure on a random pack of spheres. The Hertz-Mindlin Hashin Shtrikman (HMHS) model assumes that the grains in a rock are held together by pressure and not by cement. Therefore, this model can be used to calculate the value of the initial bulk and shear moduli ($K_0$ and $G_0$) at a given pressure according to:

$$K_0 = \left[\frac{Pn^2(1-\phi_0)^2 G_s^2}{18\pi^2(1-\nu)^2}\right]^{1/3}, \quad G_0 = \left[\frac{5-4\nu}{5(2-\nu)}\frac{Pn^2(1-\phi_0)^2 G_s^2}{2\pi^2(1-\nu)^2}\right]^{1/3} \tag{7}$$

where $P$ is the effective pressure in GPa, $n$ is the number of grain contacts and is assumed to be 8.5 in a random dense pack of spheres (Murphy, 1982), $\phi_0$ is the critical porosity, assumed to be 0.36, and $\nu$ is the Poisson's ratio calculated from $K_s$ and $G_s$. Even though critical porosity is 0.70 in these samples, critical porosity must be 0.36 for the Hertz-Mindlin model. This is one reason the porosity correction will still be used; it will decrease the effective porosity such that this model can be used more legitimately.

This HMHS model requires repeating all of the steps used previously in modeling: choosing $\phi_g$, calculating $\phi_v$, and using Equation (2) to calculate $K_g$ and $G_g$ of the porous grains from an upper Hashin-Shtrikman interpolation. The new step in this model requires substituting $K_g$ and $G_g$ for $K_s$ and $G_s$ in Equation (7). Table 2 shows the original $K_s$ and $G_s$ for the samples from Cymric with the "modified solid" moduli. When $\phi_v < \phi_0$, (all cases) the modified lower Hashin-Shtrikman bound (Equation 4) is the appropriate formula for use in the HMHS model with $\phi_0$=0.36.

Once more, the fit between this model and the samples from Asphalto was extremely poor and will not be shown; the modified upper Hashin-Shtrikman model (Figure 3) gives the best fit for the Asphalto data of all three models presented. Unfortunately, no model is as successful in describing the moduli of the Asphalto samples as those from McKittrick. I attribute this to a much more variable mineralogy from sample to sample, especially a large amount of clay.

Table 2. The original solid-grain moduli and the modified solid moduli for the samples from Cymric. For all modified solids, $\phi_g$ (phig) is noted.

| porosity | solid grains | | phig = 0.55 | | phig = 0.5 | |
|---|---|---|---|---|---|---|
| | Ks (GPa) | Gs (GPa) | Kg (GPa) | Gg (GPa) | Kg (GPa) | Gg (GPa) |
| 0.666 | 16.90 | 13.49 | 5.01 | 3.90 | 5.75 | 4.48 |
| 0.628 | 17.30 | 12.81 | 5.00 | 3.72 | 5.74 | 4.27 |
| 0.683 | 17.23 | 14.01 | 5.14 | 4.04 | 5.90 | 4.64 |
| 0.654 | 16.66 | 12.74 | 4.87 | 3.69 | 5.59 | 4.24 |
| 0.645 | 18.23 | 13.97 | 5.33 | 4.05 | 6.12 | 4.65 |
| 0.553 | 16.44 | 12.65 | 4.82 | 3.67 | 5.53 | 4.21 |
| 0.59 | 18.58 | 13.04 | 5.27 | 3.80 | 6.06 | 4.37 |

The HMHS model with porosity correction was repeated with different values of $\phi_g$; 0.5 and 0.55 gave the best fit (Figure 11) with the Cymric samples. The percentage of error between the measured and modeled $M$-moduli (25% when $\phi_g$=0.55) is not a significant improvement upon the mod HS+ model (28%). However, this new model is an improvement upon the earlier one for two reasons: the moduli modeled using the HMHS

theory with the porosity correction have the appropriate slope and the model is constrained by the physical reality of pressure dependence.

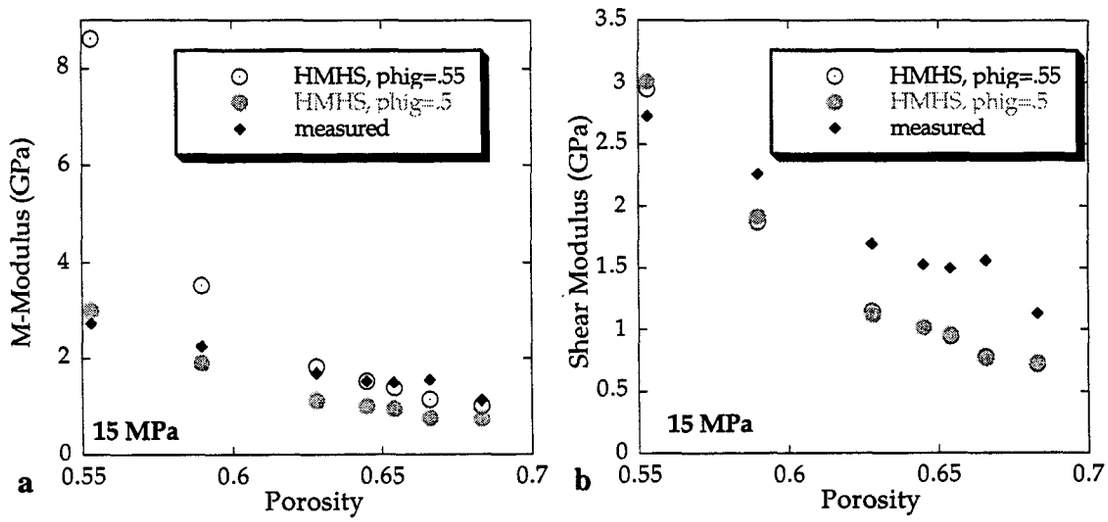


Figure 11. (a) $M$-modulus and (b) shear modulus measured on the Cymric samples versus porosity and the HMHS values ( $\phi_g$= 0.5 and 0.55) calculated from the solid grain moduli.

Repeating these calculations with the average solid-grain moduli for the Cymric samples caused almost no change in modeled modulus. Because this approximation has a minimal effect on effective medium modeling on samples with large porosity, only the modeled values from individually calculated solid phase moduli are shown in Figure 11.

## SUMMARY

The previous chapters document that porosity reduction in these three datasets occurs along two trends. In this chapter, microphotographs and analogies to rocks with known textures support the idea of two textures. One goal of this chapter was to show that not only do these rocks have two patterns of porosity reduction, but they also require two types

of effective medium modeling. Furthermore, the physical basis of the models supports the idea of two textures in these rocks.

Two models are necessary to describe the elastic moduli of the three datasets. Although both use the modified Hashin-Shtrikman model, they make different assumptions about the texture of the rocks. In the mod HS+ bound, all the porosity has an equal effect on the rock stiffness; the fit between modeled and measured values suggests that this is a good assumption in the samples from McKittrick, a mediocre assumption in the samples from Asphalto, and a poor assumption in the samples from Cymric. The datasets which do not fit this model well require a porosity correction because larger pore volumes between the grains are much more important than small pore volumes in determining elastic properties. Furthermore, the laboratory measurements in the samples from Cymric vary with pressure. When a porosity correction is added by separating porosity into grain and void porosity and a pressure term is added through Hertz-Mindlin theory, this Hertz-Mindlin Hashin-Shtrikman model with modified porosity fits the samples from Cymric well (Figure 12).

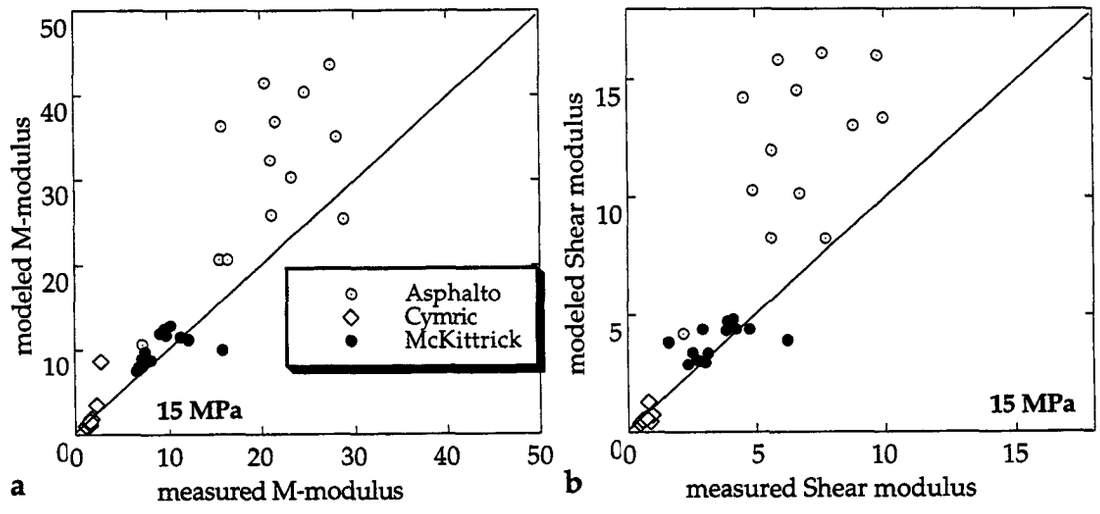


Figure 12. Modeled versus measured (a) $M$-Modulus and (b) Shear modulus for all samples.

## CONCLUSIONS

Different effective medium models describe the variation in elastic moduli with porosity for the samples from three reservoirs at different stages of silica diagenesis. All models use variations of the modified Hashin-Shtrikman bounds where critical porosity is 70%. With few assumptions, the samples from McKittrick are described well by the modified upper Hashin-Shtrikman bound; this model is also the best to describe the samples from Asphalto. Agreement with this model suggests that these datasets contain rocks composed of solid grains with low surface area to volume ratios.

The grains in the samples from Cymric and, to a lesser extent, Asphalto, have a highly irregular shape with small volumes of porosity near the irregular grain surface. One effect of this texture is that the existence of small pore volumes decreases the elastic modulus of the rock much less than the larger pore volumes. In contrast, all the porosity in the samples from McKittrick affects rock properties.

A porosity correction is necessary to model Cymric successfully because only some of the porosity has a significant effect on elastic moduli. Although an analogy to chalks suggests that the samples from Asphalto also require this porosity correction, it does not improve the estimation of the measured moduli. In addition, because the measurements from Cymric vary with pressure, pressure-dependence is added to the model by combining the Hashin-Shtrikman model with the porosity correction with Hertz-Mindlin theory. The samples from Cymric are modeled well by the Hertz-Mindlin Hashin-Shtrikman theory with a porosity correction. Agreement with this model confirms that this dataset is composed of pressure-dependent, high surface area particles.

## REFERENCES

Beyer, L. A., 1987, Porosity of unconsolidated sand, diatomite, and fractured shale reservoirs, South Belridge and West Cat Canyon Oil Fields, California, *in* Meyer, R.F., ed., Exploration for heavy crude oil and natural bitumen, **25**: Los Angeles, AAPG Studies in Geology, 395-413.

Digby, P. J., 1981, The effective elastic moduli of porous granular rocks, J. Appl, Mech., **48**, 803-808.

Dvorkin, J. and Nur, A, 1996, Elasticity of high porosity sandstones: Theory for two North Sea data sets: Geophysics, **61**, 1363-1370.

Guerin, G. and Goldberg, D. 1996, Acoustic and elastic properties of calcareous sediments across a siliceous diagenetic front on the eastern U.S. continental slope, Geophysical Research Letters, **23**, 19, 2697-2700.

Hashin, Z., and Shtrikman, S., 1963, A variational approach to the elastic behavior of multiphase materials, J. Mech. Phys. Solids, **11**, 127-140.

Hill, R., 1952, The elastic behavior of crystalline aggregate, Proc. Phys. Soc. London, A65, 349-354.

Mavko, G., Mukerji, T., and Dvorkin, J., 1996, Rock Physics Handbook.

Mindlin, R. D., 1949, Compliance of elastic bodies in contact, J. Appl. Mech., **16**, 259-268.

Murphy, W., III, 1982, Effects of Microstructure and Pore fluids on the Acoustic Properties of Granular Sedimentary Materials, Ph.D. dissertation, Stanford University.

Nobes, D.C., Murray, R. W., Kuramoto, S, Pisciotto, K. A., and Holler, P., 1992, I. Impact of silica diagenesis on physical property variations, in K. A. Pisciotto, J. C. Ingle, Jr., M. T. von Breymann, and J. Barron, eds., Proceedings of the ODP Scientific Results, Part I: Washington, D. C., NSF and Joint Oceanographic Institutions, **127**, 3-32.

Nur, A., Mavko, G., Dvorkin, J. and Galmudi, D., 1998, A key to relating physical properties to porosity in rocks: SEG/The Leading Edge, **17**, 3, 357-362.

O'Brien, D. K., Manghnani, M. H., and Tribble, J. S., 1989, Irregular trends of physical properties in homogenous clay-rich sediments of DSDP Leg 87 Hole 584, Midslope terrace in the Japan Trench: Marine Geology, **87**, 183-194.

Williams, L. A., Parks, G. A., and Crerar, D. A., 1985, Silica Diagenesis I. Solubility controls: Journal of Sedimentary Petrology, **55**, 3, 301-311.

# CHAPTER 4

# COMPARISON OF WELL LOG AND LABORATORY ULTRASONIC MEASUREMENTS AT DIFFERENT STAGES OF SILICA DIAGENESIS


## ABSTRACT

Laboratory measurements on Miocene Monterey formation samples undergoing silica diagenesis aid in well log interpretation of similar rocks. Both laboratory and well log measurements from three California Monterey Formation reservoirs are supplemented with data from other siliceous wells at various stages of silica diagenesis. Data from these reservoirs includes elastic wave velocities, porosity, density, and mineral content of laboratory samples; permeability data; and several well log curves. The observations are from the full sequence of silica diagenesis: from opal-A to opal-CT to quartz. One direct application of the laboratory results to well log interpretation is an improved ability to calculate porosity from the densitylog. A standard bulk density to porosity transformation does not work in siliceous reservoirs because the mineral density changes during diagenesis.


## INTRODUCTION

Siliceous shale reservoirs are important oil-producing rocks. The Miocene Monterey Formation, for example, is the primary source rock for hydrocarbons in California. However, production from these rocks is very difficult; better reservoir characterization may improve recovery. To this end, I have made laboratory measurements of ultrasonic velocity at different degrees of silica diagenesis.

One important aspect of these siliceous rocks is that they are primarily biochemical precipitates. Initially silica precipitates from seawater to form the skeletal material of

microorganisms in an X-ray amorphous form. This silica, called opal-A, readily dissolves and undergoes diagenetic transitions as it first precipitates as an intermediate phase called opal-CT, and then alters to quartz. Because each successive polymorph is less disordered, progressive silica diagenesis is often accompanied by increased grain density and reduced porosity. With the change from opal-A to opal-CT, grain density increases by about 0.1 $g/cm^3$ and porosity may reduce by 20% (Murata and Larson, 1975; Beyer, 1987).

Relationships among velocity, porosity, density, mineral content, and the stage of silica diagenesis have been recognized from laboratory and well log studies of opaline rocks (Beyer, 1987; O'Brien et al., 1989; Nobes et al., 1992b, c; Tribble et al., 1992; Guerin and Goldberg, 1996). The goal of this work is to evaluate how quantitative laboratory-derived relationships apply to well logs and, specifically, apply density-porosity transformations for opaline rocks to well log interpretation. To do so, I compare laboratory and well log data from three wells, each from a different reservoir in the Miocene Monterey Formation of California, two wells from the Norwegian North Sea, and one well from the Ocean Drilling Project (ODP) data collected in the Japan Sea (Nobes et al, 1992b).

Measurements of samples at different stages of silica diagenesis are recorded in all cores. Of the samples from the southwest San Joaquin Valley of California, the samples from Cymric traverse the opal-A/opal-CT transition, those from McKittrick are all opal-CT phase, and those from Asphalto field traverse the opal-CT/quartz transition. The samples from the Senja Ridge, in the Norwegian North Sea traverse the entire sequence, and those from the Sea of Japan range from opal-A to opal-CT.

Diagenetic silica transitions can be recognized from well logs because physical properties vary between the different polymorphs. For example, in Cymric field, opal-A can be recognized by its high porosity (for example, from a well log), and the opal-A/opal-CT transition can be recognized by a decrease in porosity and increase in velocity and/or bulk density (Tom Zalan, pers. comm., 1997); these patterns are noted in other reservoirs by O'Brien et al. (1989), and Guerin and Goldberg (1996). As another example, the

dominant silica polymorph can often be predicted by comparing neutron porosity and density with depth (i.e., Tom Zalan, pers. comm., 1997). Since bulk density increases and porosity decreases with diagenesis, a change in both parameters often signals a change from opal-A to opal-CT or a change from opal-CT to quartz (Figure 1).

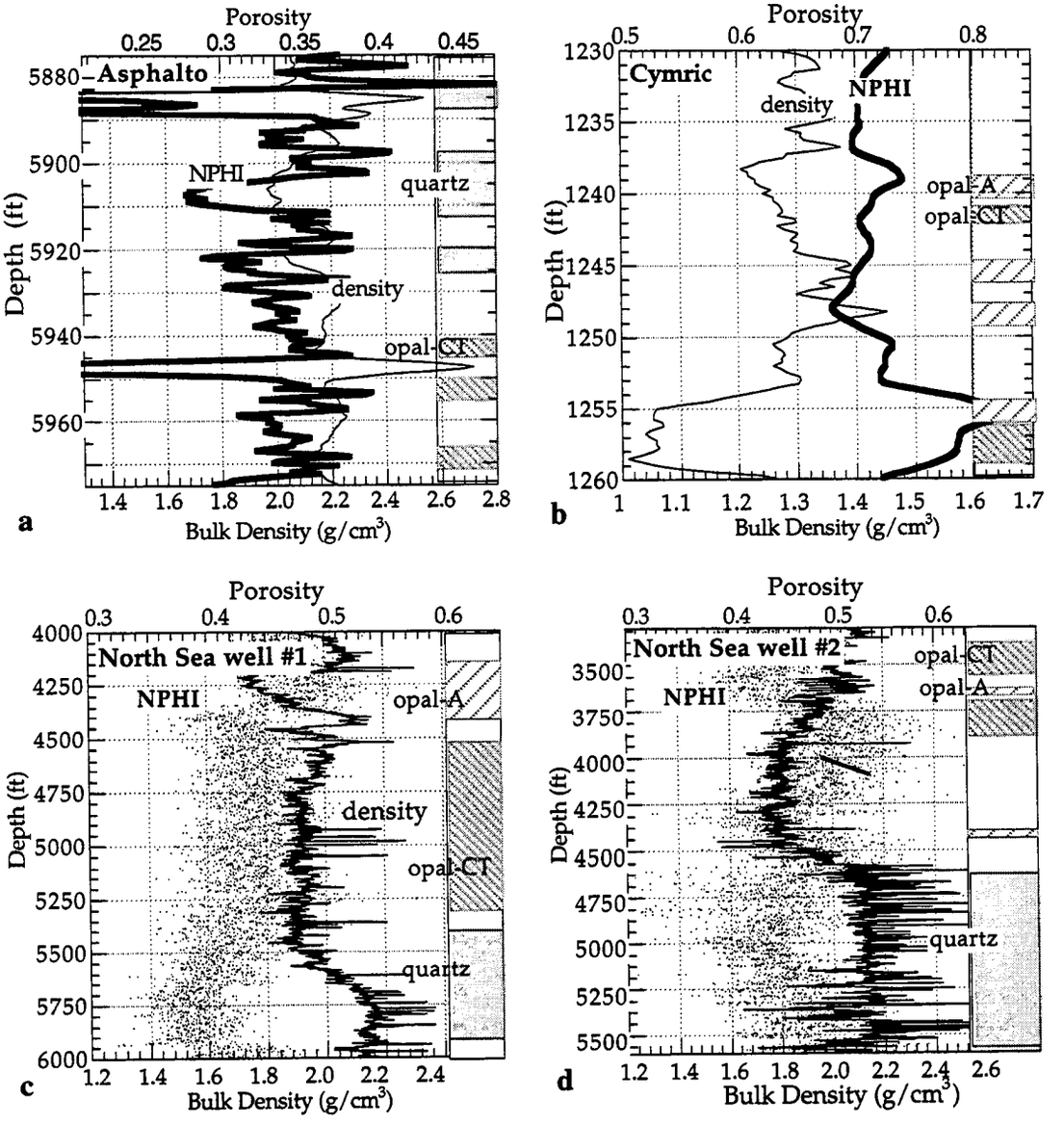


Figure 1. Neutron porosity and density-porosity for sampled intervals in the wells from Cymric, Asphalto, and the North Sea.

Figure 1 shows well log data from four wells which span diagenetic silica transitions. At depths where mineral content was identified, the dominant silica polymorph is noted; white space denotes depths at which mineral content was not analyzed. A depth characterized by given polymorph has a wide range of porosity or density because physical properties are also affected by factors such as the proportions and type of other minerals present, and the age, pressure, and texture of the rock. The narrow intervals presented from Cymric and Asphalto reveal the heterogeneity of the San Joaquin Valley reservoirs. Not only does the dominant silica polymorph change within narrow intervals, but the properties of each silica polymorph (such as the porosity of opal-CT in the different wells) are extremely variable.

Not only is it useful to identify the dominant silica polymorph through similarities in physical properties, but it is also useful to understand why physical properties of a given polymorph vary. Figure 2 shows permeability for the wells from McKittrick and Asphalto and a well from Cymric approximately 0.25 miles away from the sampled Cymric well.

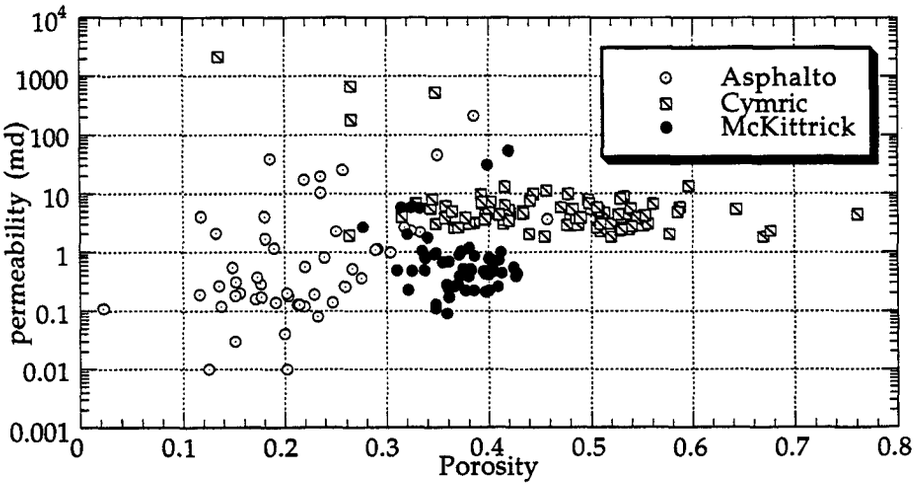


Figure 2. Permeability versus porosity for data from Asphalto, Cymric and McKittrick reservoirs.

At 40% porosity, permeability varies within two orders of magnitude. Although the majority of the silica in both wells is opal-CT, the permeability in the Cymric well exceeds that of the McKittrick well by an order of magnitude. Chapter 1 shows that porosity reduction associated with the diagenetic transition from opal-A to opal-CT in these two wells follows different paths. I speculate that the difference in porosity reduction patterns results in differing pore geometry, which, in turn, has an effect on permeability. Therefore, by identifying the diagenetic pathway, one can better predict permeability.

## LABORATORY PROCEDURE

Porosity, bulk and grain density is known for all laboratory samples. In addition, ultrasonic velocity was measured on the samples from California (Appendix D), and two samples from North Sea well #1. The abundance of the constituent minerals in the laboratory samples from California and sidewall samples from both North Sea wells were determined using Fourier Transform Infrared Spectroscopy (FTIR), described by Harville and Freeman (1988). Methods and measurements of porosity, bulk density, and mineralogy of all samples analyzed is described in Appendix A.

Measurements of porosity and density of the samples from the North Sea requires more explanation. Porosity could not be measured directly on the sidewall powders from the North Sea. However, FTIR determined the mineral content of the powders, and grain density, $\rho_s$, was calculated from the fractions of the different minerals. Saturated bulk density, $\rho_{b(sat)}$, from the well log, fluid density, $\rho_f$, of 1.02 g/cm$^3$ (Table 1), and the grain density were used in the relation $\rho_{b(sat)} = \rho_s(1-\phi) + \rho_f\phi$ to estimate porosity of the powdered samples. The porosity and density of the laboratory samples from the Sea of Japan is from Nobes et al., (1992a). Although this reference details corrections to the shipboard measurements, the data still contain errors; from the data presented, I cannot duplicate the measurements.

The core plugs samples (the samples from the three reservoirs in California) were cut parallel to bedding and cleaned with toluene to rid them of oil and interstitial brines. As a consequence, measurements were made on room-dry samples at atmospheric pore pressure. Ultrasonic (about 1 MHz) P- and S-wave velocities were measured by a pulse-transmission technique under hydrostatic pressure. The effective pressures at reservoir depth (1240 ft for Cymric, 3500 ft for McKittrick, and 6000 ft for Asphalto) are about 6 MPa, 25 MPa, and 30 MPa, respectively. Therefore, experimental pressures were raised to 30 MPa to bracket field conditions.

Velocities were measured during loading and unloading. If there was a difference between loading and unloading velocities, values obtained during the loading cycle were smaller that those during unloading. I attribute this difference to grain crushing, particularly in the samples from Cymric, at pressures much higher than in situ pressure. This is why well log data will be compared to loading velocity data.

## CONVERTING DRY ROCK DATA TO SATURATED ROCK DATA

Both rock and fluid properties affect ultrasonic velocity. Therefore, in order to best determine elastic properties of the solid, laboratory measurements from the three California reservoirs were made on dry samples. However, since well log measurements are from saturated rocks, the dry sample measurements are mathematically saturated using Gassmann's (1951) equation.

$P$- and $S$ wave velocity, $K_{dry}$, the dry bulk modulus, and $K_s$, the bulk modulus of the solid phase are required for Gassmann's equation. The dry bulk modulus is calculated from dry velocity data by the relationship $K_{dry} = \rho V_P^2 - \frac{4}{3}\rho V_S^2$, where $\rho$ is dry bulk density. The solid phase bulk modulus is calculated according to the Hill (1952) average:

$$K_s = .5\left[\sum_{i=1}^{N} f_i K_i + \left(\sum_{i=1}^{N} \frac{f_i}{K_i}\right)^{-1}\right]$$

where $f_i$ is the volume fraction of a mineral and $K_i$ is the modulus of that mineral.

With this necessary information, the transformation between the dry-rock bulk modulus and $K_{sat}$, the saturated-rock bulk modulus, is calculated with Gassmann's equation:

$$K_{Sat} = K_s \frac{\phi K_{Dry} - (1+\phi) K_f K_{Dry} / K_s + K_f}{(1-\phi) K_f + \phi K_s - K_f K_{Dry} / K_s}$$

where $\phi$ is porosity and the subscript "f" refers to the pore fluid.

If only $P$-wave velocity is available, Mavko et al. (1995) suggested an approximation by which the bulk modulus in Gassmann's relation is replaced with the $P$-wave (or $M$) modulus, calculated $M_{dry} = \rho V_P^2$. The modulus of the solid phase, $M_s$ is calculated according to Hill's average where $M_i$ is substituted for $K_i$; $M_{sat}$, the saturated $M$-modulus, is calculated according to:

$$M_{Sat} = M_s \frac{\phi M_{Dry} - (1+\phi) K_f M_{Dry} / M_s + K_f}{(1-\phi) K_f + \phi M_s - K_f M_{Dry} / M_s}.$$

Pore fluids have different petrophysical properties if they vary in composition, pressure, or temperature. Calculating the density and bulk modulus of the pore fluids requires information about the salinity, temperature, pressure, oil gravity, and the gas-to-oil ratio (GOR) in the pore fluid. The percentage of oil and the GOR for the California reservoirs was provided by Chevron. Where appropriate, the approximate depth of the opal-A/opal-CT transition is used for calculating pore pressure. Available information was used in a computer package (Petrotools, 1997) to calculate fluid density, $\rho_f$, and solid phase modulus, $K_f$ (Table 1).

Table 1. Estimation of fluid properties.

| Field/ Depth | Temperature | salinity | Oil Gravity | % oil | GOR | $\rho_f$ g/cm$^3$ | $K_f$ (GPa) |
|---|---|---|---|---|---|---|---|
| Asphalto 6000 ft. | 190 F (Wang & Munro, 1982; Sass et al., 1982) | <25,000 ppm (Zalan, pers. comm., 1997) | 13.5 (Bair, pers. comm., 1997) | 15% | 0.33 | 0.93 | 0.869 |
| Cymric 1250 ft. | 125 F (same gradient as Asphalto) | ~6000 ppm (Klinchuh, pers. comm., 1997) | 13.5 (same as Asphalto) | 60% | 0.0 | 0.98 | 2.12 |
| McKittrick 3500 ft. | 132 F (Muhlern et al., 1983) | use Cymric values | 14. (Muhlern et al., 1983) | 15-20% | 0.50 | 0.90 | 0.396 |
| North Sea 4450 ft. | 93 F (Johnstad, pers. comm., 1997) | ocean salinity 32000 ppm | NA | 0 | – | 1.02 | 0.26 |
| Japan Sea 700 ft | 118 F (Kuramoto et al., 1992) | ocean salinity 32000 ppm | NA | 0 | – | 1.01 | not used |

## COMPARISON OF DATA

Common problems which cause mismatches between log and laboratory values include depth mismatch, sampling bias, and/or anisotropy. The depths recorded by the well logging tool and the depths documented for the core samples are not perfectly aligned. For example, core data from Asphalto is shifted about 10 feet to match the log data (Bilodeau, pers. comm., 1996). No similar information was obtained on the other wells. Also, the well log tool samples rock properties at different intervals; properties are measured six times a foot in the data from McKittrick, twice a foot with the data from Asphalto, and once a foot in Cymric. The consequence of these two problems is that core data from a given depth may not document the same rock sampled by the well log tool.

Laboratory samples generally represent a biased subset of rocks: the samples tend to be taken from the most coherent regions of a well. If this bias is significant, laboratory data will have greater density and velocity and lower porosity than well log data.

Anisotropy, when velocity measured in one direction is different from velocity measured in another direction, also may cause mismatches between laboratory and log data.

Core plugs are generally taken perpendicular or subperpendicular to bedding; as a result, ultrasonic velocity measurements are taken at 90° to the sonic velocity measurements. The bedding parallel direction, the direction of the laboratory measurements, gives the fastest velocity in an anisotropic material.

These concerns are evaluated by comparing density, sonic velocity, and neutron porosity measured in the well with laboratory measurements of density, ultrasonic velocity at near in situ pressure, and porosity (Figures 3, 4, 5, and 6).

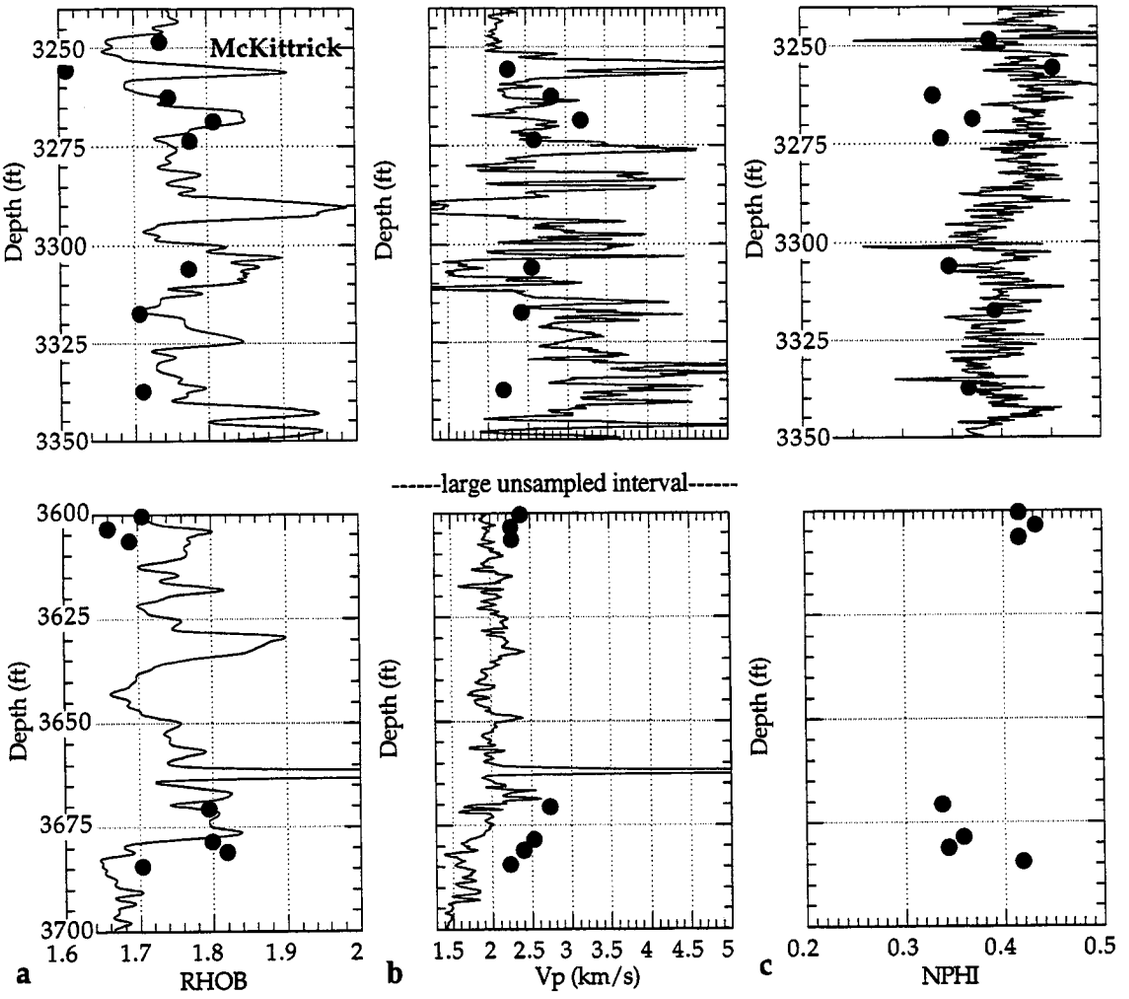


Figure 3. Well log and laboratory measurements from McKittrick including (a) saturated bulk density, (b) $P$-wave velocity (laboratory data at 30 MPa), and (c) porosity. Neutron porosity data was collected only in the shallower depths of the well.

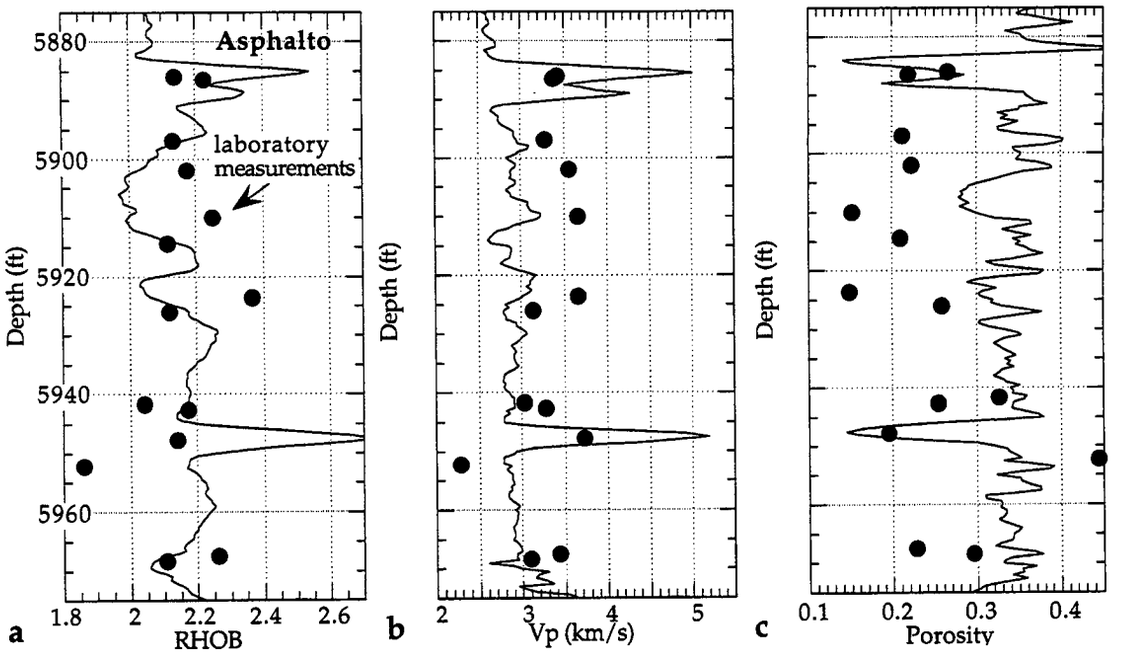


Figure 4. Well log and laboratory measurements from Asphalto including (a) saturated bulk density, (b) $P$ -wave velocity (laboratory data at 30 MPa), and (c) porosity.

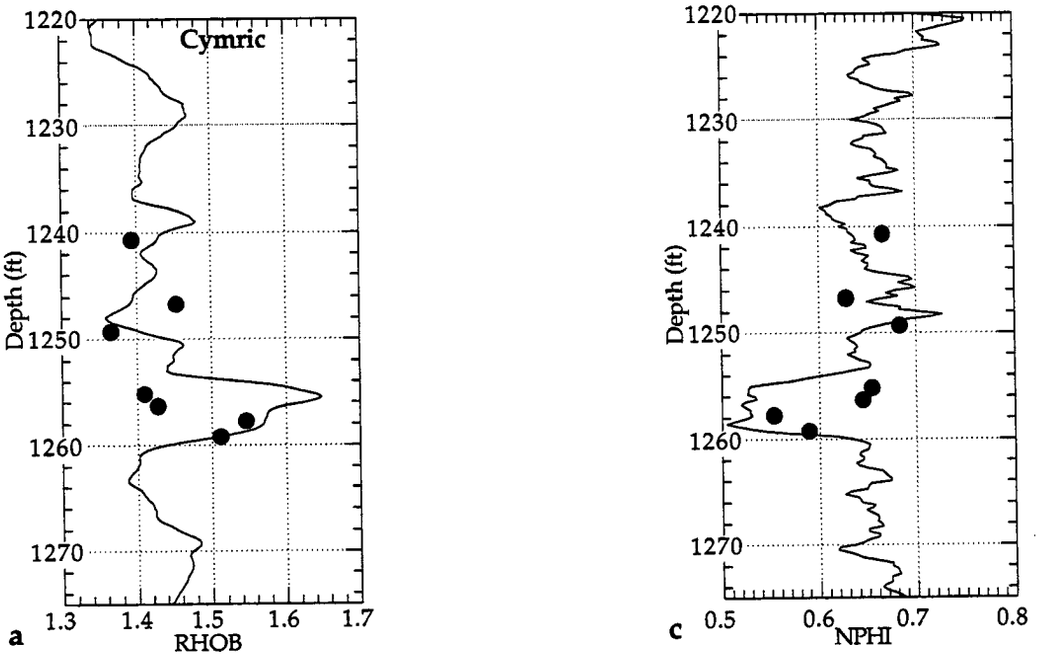


Figure 5. Well log and laboratory measurements from Cymric including (a) saturated bulk density and (c) porosity. No sonic velocity data was collected.

The laboratory and well log data are in greatest agreement with measurement of bulk density, one of the most trustworthy log measurements. The difference between well log and laboratory measurements of bulk density is small (at most 15%, with an average of about 8% for each well). Because the two measurements are similar, the samples in Figures 3, 4, and 5 are probably fresh. In contrast, the agreement between direct and logged properties for one North Sea well (Figure 6) is extremely poor. This well was logged in 1982, 16 years before the laboratory ultrasonic velocity measurements, and the laboratory sample properties are no longer representative of the in situ properties.

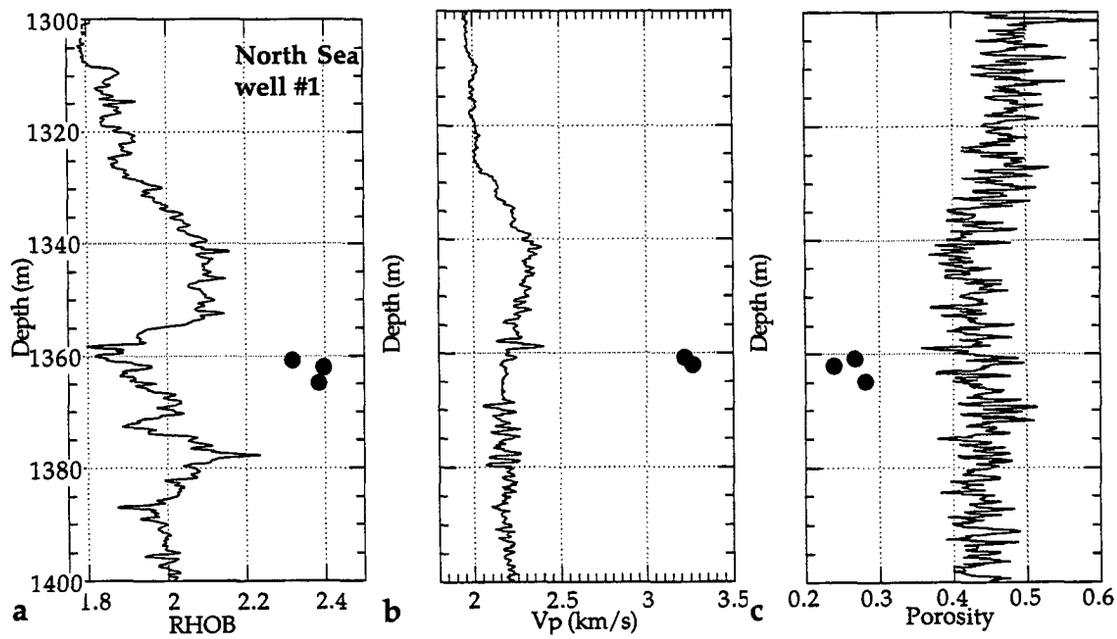


Figure 7. Same as Figure 4, but for the North Sea well #1.

Although laboratory and well log measurements of bulk density match well in the San Joaquin Valley wells, laboratory measurements of velocity and porosity are generally faster and smaller than well log measurements, respectively. Two possible causes of the velocity mismatch are depth mismatches or anisotropy.

A way to emphasize that depth mismatches are the most significant cause of deviation between laboratory and well log measurements is to present the data in graphs of velocity versus bulk density (Figure 7). Furthermore, although there is no sonic log data from the sampled well from Cymric, there is sonic velocity data from a well approximately 0.25 miles away. By plotting density versus velocity, the well log data of similar lithology plots near the Cymric laboratory data collected at 7.5 MPa. Again, the laboratory data from the North Sea well misalign with the log data.

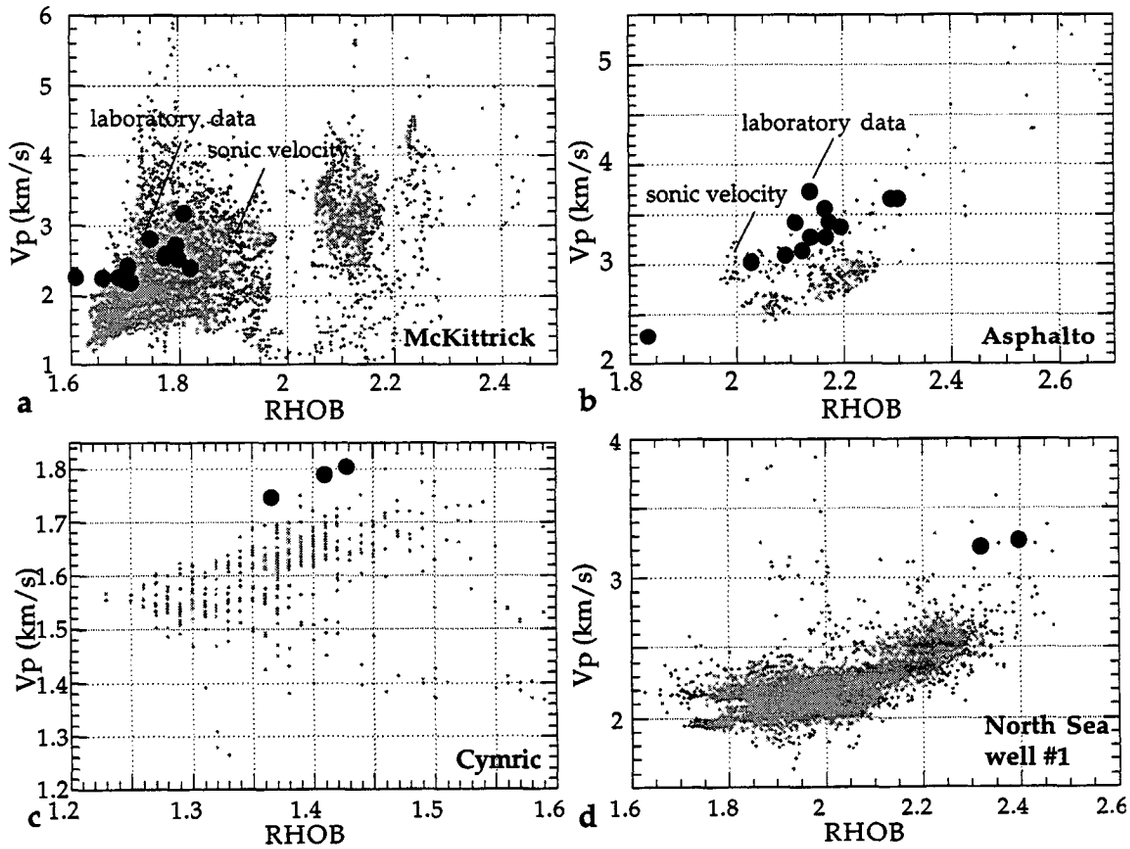


Figure 7. $P$-wave velocity as measured both by the well log and in the laboratory.

One of the causes of anisotropy is preferred orientation of minerals (Vernik and Nur, 1992); therefore, it is closely related to layered minerals such as clays. Therefore, if anisotropy is the cause of the velocity mismatch, the clay-rich Asphalto data should

overestimate the sonic velocity data much more than the clay-poor McKittrick data. Instead, the laboratory data overlaps with the higher-velocity, lower bulk density log data in both cases. Furthermore, because samples with laboratory porosity less than neutron porosity also are those with greater velocity, the laboratory data is probably recording properties of a slightly different material. Therefore, the mismatch between laboratory and in situ petrophysical properties is due to the sampling issues and not anisotropy.

## DENSITY TO POROSITY TRANSFORM

As discussed in Chapter 1, trends of dry-rock bulk density $\rho_b$ versus porosity $\phi$ from data from seven localities in California of the Monterey Formation produce two distinctive linear trends. These data are from the three reservoirs discussed here, supplemented with additional data from the Elk Hills reservoir (Reid and McIntyre, in prep), and Point Pedernales (Compton, 1991), near the Santa Barbara coast. Furthermore, data from reservoirs at North and South Belridge are from Shell and Mobil, respectively. All datasets have been restricted to samples with greater than 40% silica by volume to focus on the effect of silica diagenesis on physical property variations.

Since dry bulk density, $\rho_b$, can be converted to saturated bulk density, $\rho_{b(sat)}$, using $\rho_{b(sat)} = \rho_b + \rho_f \phi$, where $\rho_f$ is fluid density, the two high-correlation regressions in Chapter 1 can be used with saturated samples. Although the fluid density for the different reservoirs is shown in Table 1, if $\rho_f$ is simply assumed to be 1.0 g/cm$^3$, the saturated bulk density-porosity trends become

$$\rho_{b(sat)} = 2.581 - 1.725\phi; \qquad (1)$$

and

$$\rho_{b(sat)} = 2.061 - 0.926\phi; \qquad (2)$$

where density is in g/cm$^3$, and porosity is a volume fraction. Saturated bulk density versus porosity as calculated for the laboratory samples, the density log versus neutron porosity for three of the San Joaquin Valley reservoirs, and the lines described by Equations (1) and (2) are shown in Figure 8.

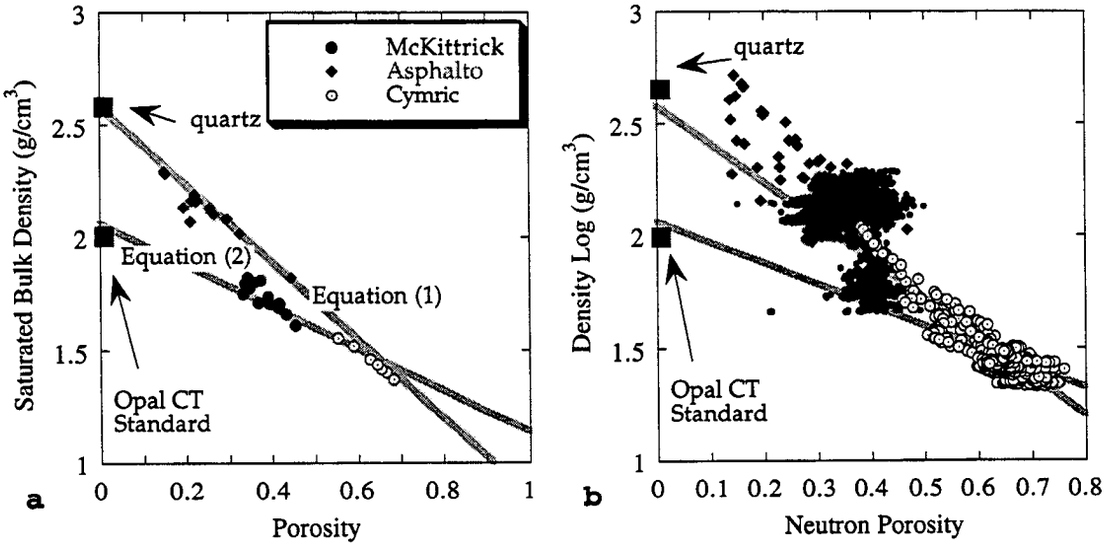


Figure 8. Density versus porosity as determined from (a) laboratory samples and (b) well logs on samples from three reservoirs in the San Joaquin Valley of California.

Figures 3, 4, and 5 show that although laboratory and well log measurements of density are similar, helium porosity and neutron porosity are often different. Neutron porosity is often larger than helium porosity because in addition to pore fluids, the tool also detects water bound by clay minerals (or opal). Therefore, the regression equations in Figure 8b, although shown, are not accurate for neutron porosity. However, it is clear from both laboratory and well log data that both laboratory and log data from Asphalto and Cymric follow Equation (1), and some of the data from McKittrick follows Equation (2). Although it is wise to make some laboratory measurements for greatest confidence whether

a dataset follows Equation (1) or Equation (2), direct well log information can often determine which pattern of porosity reduction a dataset follows.

The two porosity reduction trends also describe other wells in siliceous sediments: the ones from the North Sea and the Sea of Japan (Nobes et. al., 1992a, b; Figure 9). The samples from which helium porosity was measured in the North Sea wells were damaged, but the porosity of the sidewall powders was calculated indirectly. After identifying which trend a datasets follows, these equations can be an excellent bulk density to porosity transform for siliceous rocks that can be used with well logs.

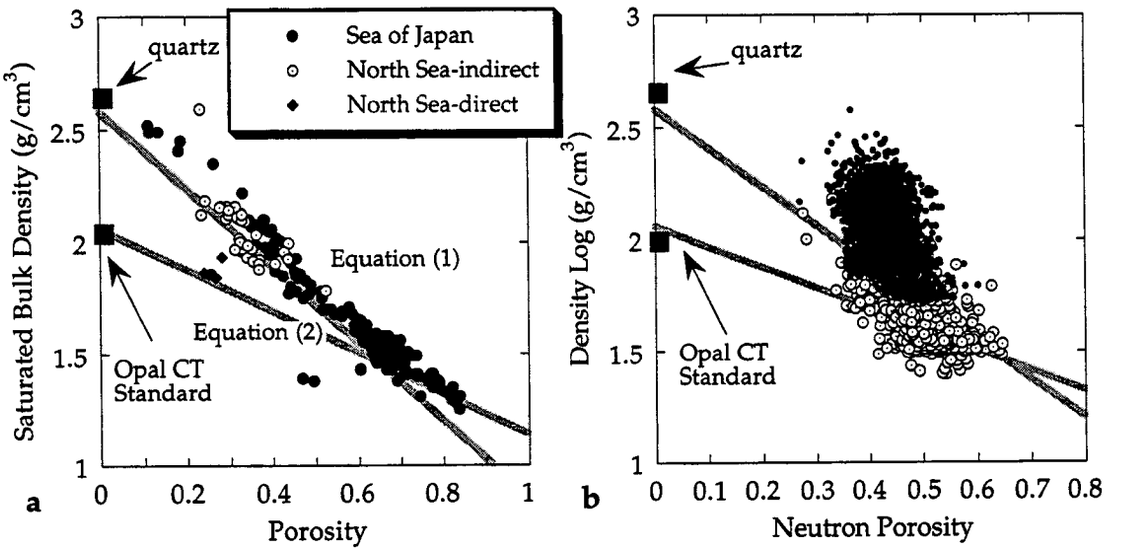


Figure 9. Density versus porosity as determined from (a) laboratory samples and (b) well logs on samples from the Sea of Japan and the North Sea.

The laboratory measurements from the North Sea well #1 (Figure 9a) suggest that the samples are fit by Equation (2). However, I have already determined that the laboratory samples have altered since coring and do not give measurements reflective of in situ conditions. Therefore, I use the density-porosity trend from the sidewall powders to analyze the samples from the North Sea. Figure 9a shows that both the data from the Sea of Japan and the North Sea are best fit by Equation (1).

These regressions are of particular use with these rocks because a common method of calculating porosity from density assumes constant grain density $\rho_s$. In this method, porosity is calculated: $\phi = (\rho_s - \rho_{b(sat)})/(\rho_s - \rho_f)$. Assuming grain density is constant is problematic because not only are the grain densities of opal-A, opal-CT, and quartz different from each other but also the grain density of opal is much less than most rock-forming minerals. Therefore, after determining whether a dataset follows Equation (1) or Equation (2), the regression equations can be a powerful density to porosity transform that can be used with well logs.

Depth versus porosity for the three wells from California (Figure 10) and the two North Sea wells plus one well from the Sea of Japan (Figure 11) present porosity measured in four different ways: (a) direct laboratory measurements of porosity on core samples, (b) neutron porosity from the log data, (c) density-porosity calculated from the density log where grain density is assumed to be 2.5 g/cm$^3$, and (d) porosity calculated from Equation (1) or (2). All samples but those from McKittrick use Equation (1); the samples from McKittrick use Equation (2).

The porosity determined with the porosity-density transform is at least as good as the other two well log-based methods in approximating the direct measurements. The one place where the transform consistently errs is in the shallower samples from the Sea of Japan. This is probably because these are unlithified sediments; the regressions were only determined on lithified rocks. However, with a larger dataset of unlithified sediments, more appropriate regression equations could likely be found. Therefore, this analysis of siliceous samples from three regions presents a density-to-porosity relationship can be useful in determining porosity from logs in any lithified region undergoing silica diagenesis.

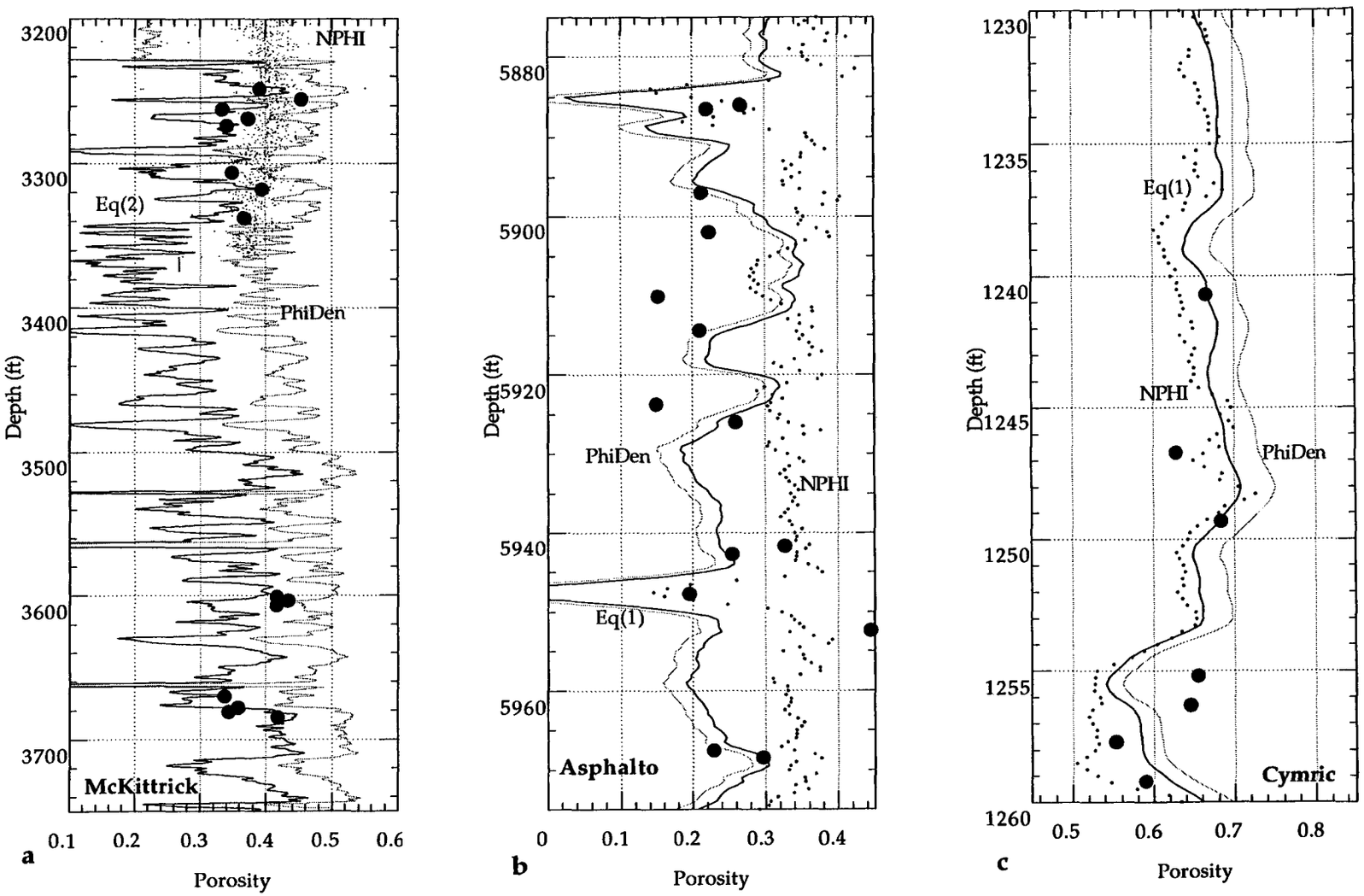


Figure 10. Porosity versus depth in the wells from (a) McKittrick, (b) Asphalto, and (c) Cymric along with the porosity of laboratory samples. Log porosity is presented as: neutron porosity (NPHI) as points, density porosity (PhiDen) where grain porosity is 2.5 g/cm$^3$ is a gray line, and porosity from the appropriate bulk density to porosity transform, denoted either Eq (1) or Eq (2) is shown as a black line.

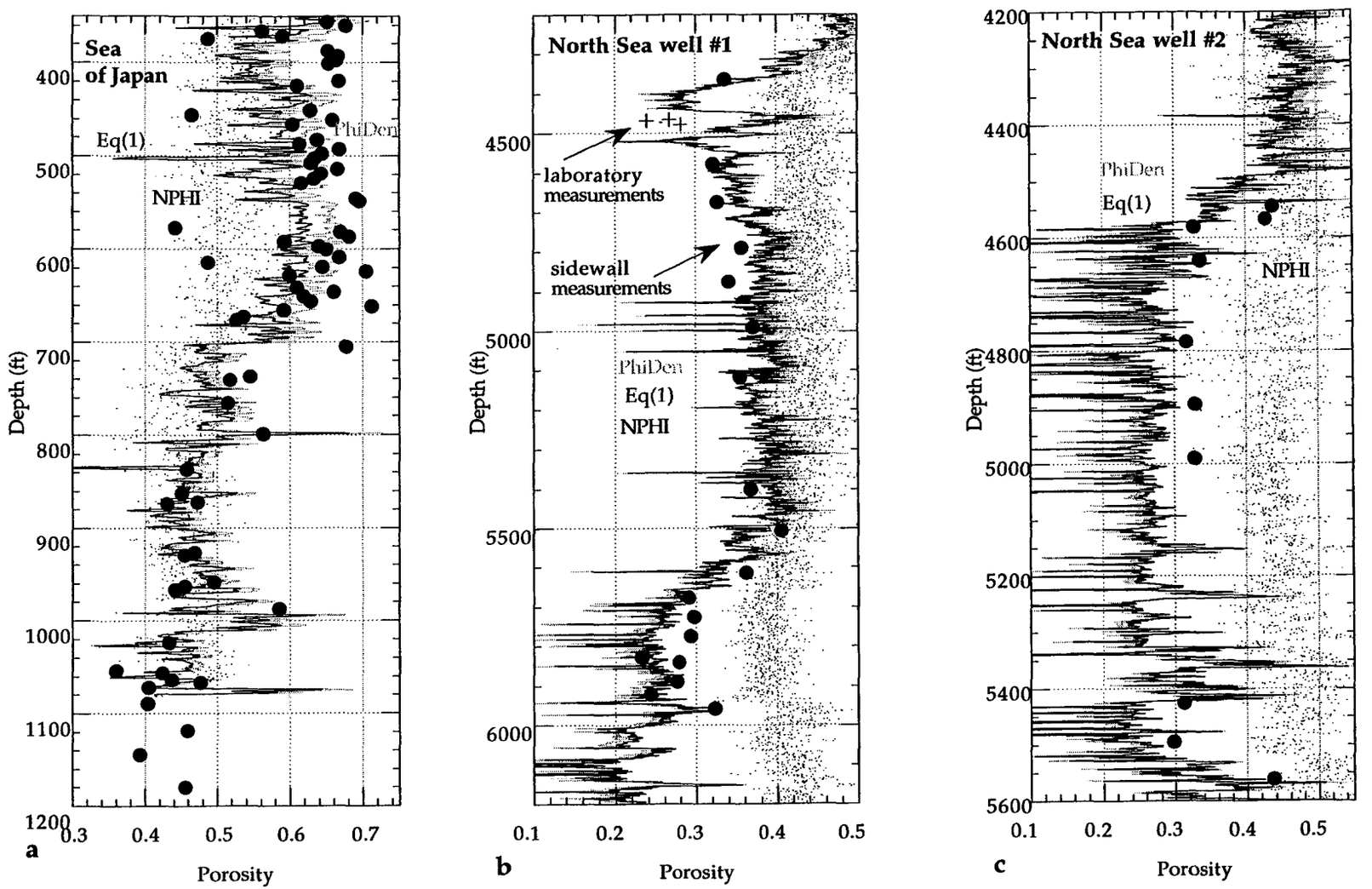


Figure 11. Laboratory and well log porosity versus depth in the wells from (a) the Sea of Japan, (b) North Sea well #1, and (c) North Sea well #2. Like Figure 10, log porosity is presented in three ways.

## CONCLUSIONS

Well log and laboratory information from different regions undergoing silica diagenesis were compiled to improve characterization of these rocks using log information. The greatest amount of data is from three Monterey Formation reservoirs in the southwest San Joaquin Valley, California. Data from these reservoirs includes elastic wave velocities, porosity, density, and mineral content of laboratory samples; permeability data; and several well log curves. Laboratory measurements of density and velocity agree with well log measurements from these wells.

Measurements of both laboratory and log bulk density versus porosity reveal two trends. The regression equations through the laboratory data yield a transform that can be used on well logs. This transform estimates log porosity at least as accurately as neutron porosity and density porosity. Furthermore, this transform is not specific to the Monterey Formation; it also estimates porosity successfully in wells from the North Sea and the Japan Sea.

## REFERENCES

Beyer, L. A., 1987, Porosity of unconsolidated sand, diatomite, and fractured shale reservoirs, South Belridge and West Cat Canyon Oil Fields, California, *in* Meyer, R.F., ed., Exploration for heavy crude oil and natural bitumen: AAPG Studies in Geology, **25**, 395-413.

Compton, J. S., 1991, Porosity reduction and burial history of siliceous rocks from the Monterey and Sisquoc Formations, Point Pedernales area, California: Geological Society of America Bulletin, **103**, 625-636.

Gassmann, F., 1951, Uber die elastizitat poroser medien, Vier. der Natur Gesellschaft, **96**, 1-23.

Guerin, G. and Goldberg, D. 1996, Acoustic and elastic properties of calcareous sediments across a siliceous diagenetic front on the eastern U.S. continental slope, Geophysical Research Letters, **23**, 19, 2697-2700.

Harville, D. G. and Freeman, D. L., 1988, The Benefits of Application of Rapid Mineral Analysis Provided by Fourier Transform Infrared Spectroscopy: SPE Conference Proceedings, 141-146.

Hill, R., 1952, The elastic behavior of crystalline aggregate, Proc. Phys. Soc. London, A65, 349-354.

Kuramoto, S., Tamaki, K, Langseth, M. G., Nobes, D. C., Tokuyama, H., Pisciotto, K. A., and Taira, A, 1992, Can opal-A/opal-CT BSR be an indicator of the thermal structure of the Yamato Basin, Japan Sea? *in* Pisciotto, et al., eds., Proceedings of the Ocean Drilling Program Scientific Results, Vol 127/128, Pt. 2, 1145-1155.

Mavko, G., Chan, C., and Mukerji, T., 1995, Fluid substitution: estimating changes in Vp without knowing Vs: Geophysics, **60**, 6, 1750-1755.

Mulhern, M. E., Eacmen, J. C., Jr., and Lester, G. K., 1983, Geology and oil occurrence of displaced Diatomite Member, Monterey Formation, McKittrick oil field, in Isaacs, C. M., and Garrison, R. E., eds., Petroleum generation and occurrence in the Miocene Monterey Formation, California: SEPM Pacific Section, Los Angeles, 17-37.

Murata, K. J., and Larson, R. R., 1975, Diagenesis of Miocene siliceous shales, Temblor Range, California: U.S. Geological Survey Journal of Research, **3,** p. 553-566.

Nobes, D. C., Langseth, M. G., Kuramoto, S., Holler, P., 1992, Identification and correction of a systematic error in index property measurements, *in* Pisciotto, K. A, et al., eds., Proceedings of the Ocean Drilling Program Scientific Results, Vol 127/128, Pt. 2, 985-1016.

Nobes, D. C., Langseth, M. G., Kuramoto, S., Holler, P. and Hirata, N., 1992, Comparison and correlation of Physical-Property results from Japan Sea Basin and Rise sites, Legs 127 and 128, *in* Pisciotto, K. A. et al., eds., Proceedings of the Ocean Drilling Program Scientific Results, Vol 127/128, Pt. 2, 1275-1296.

Nobes, D. C., Murray, R. W., Kuramoto, S., Pisciotto, K. A., and Holler, P., 1992, Impact of Silica Diagenesis on Physical Property variations, *in* Pisciotto, K. A., et al., eds., Proceedings of the Ocean Drilling Program Scientific Results, Vol 127/128, Pt. 1, 3-31.

O'Brien, D. K., M. H. Manghnani, and J. S. Tribble, 1989, Irregular trends of physical properties in homogenous clay-rich sediments of DSDP Leg 87 Hole 584, Midslope terrace in the Japan Trench: Marine Geology, **87**, 183-194.

Petrotools 2.5, 1997, Petrosoft, Inc.

Sass, J.H., Gananis, S.P.,Jr., Munroe, R. J., 1982, Measurement of heat flow by a downhole probe technique in the San Joaquin Valley, California: USGS Open-File Report 82-819.

Tribble, J. S., Mackenzie, F. T., Urmos, J., O'Brien, D. K., and Manghnani, M. H., 1992, Effects of Biogenic Silica on Acoustic and Physical Properties of Clay-Rich Marine Sediments: AAPG Bulletin, **76**, 6, 792-804.

Vernik, L. and Nur, A., 1992, Ultrasonic velocity and anisotropy of hydrocarbon source rocks: Geophysics, **57**, 5, 727-735.

Wang, J., and Munroe, R. J., 1982, Heat flow and sub-surface temperatures in the Great Valley, California: USGS Open File Report 82-844.

# CHAPTER 5

# STRESS-SENSITIVITY OF SANDSTONES


## ABSTRACT

Laboratory measurements show that the sensitivity of elastic moduli and velocities in sandstone to effective hydrostatic pressure increases with decreasing porosity: The difference between dry-rock elastic moduli measured at high and low stress, spans (at a fixed porosity value) an interval. This interval is close to zero as porosity approaches the critical porosity value (about 0.38 for sandstones), and reaches its maximum as porosity approaches zero. We explain this observation by using a combination of two heuristic models -- the critical porosity model and the modified solid model. The former is based on the observation that the elastic-modulus-versus-porosity relation can be approximated by a trajectory that connects two points in the modulus-porosity plane: the modulus of the solid phase at zero porosity, and zero at critical porosity. The second one reflects the fact that at constant effective stress, low-porosity sandstones (even with small amounts of clay) exhibit large variability of elastic moduli. We attribute this variability to compliant cracks which hardly affect porosity, but strongly affect the stiffness. We used this combined model to give a practical recipe for estimating P- and S-wave velocities versus stress from a single measurement.


## INTRODUCTION

Effective stress in a reservoir, defined as the difference between confining stress and pore pressure, is subject to large variations during production. For example, during hydrofracturing pore pressure is elevated to reach the confining stress, resulting in zero (or

even negative) effective stress. During depletion effective stress may increase due to decreasing pore pressure. This can lead to rock's mechanical instability (e.g., sanding).

Variation of both P- and S-wave velocities with stress may be very large. Consider, for example, Weber sandstone of 9.5% porosity (Coyner, 1984). P-wave velocity ($V_p$) in the dry rock increases from 3 km/s to 4 km/s as effective stress varies between 10 MPa and 40 MPa (Figure 1). At the same time, the low-frequency P-wave velocity in the saturated rock changes from 3.75 km/s to 4.3 km/s, and the ultrasonic P-wave velocity in the saturated rock changes from 4.3 km/s to 4.6 km/s. Variations of stress induce also large changes in S-wave velocity ($V_s$). These velocity changes can be definitely detected by sonic loging, and crosswell and surface seismic. Therefore, obtaining functional relations between velocity and stress may lead to a stress-prediction-from-seismics theory. Currently, such predictions are based on purely statistical correlations (e.g., Eberhart-Phillips and Han, 1989) and thus resist generalization.

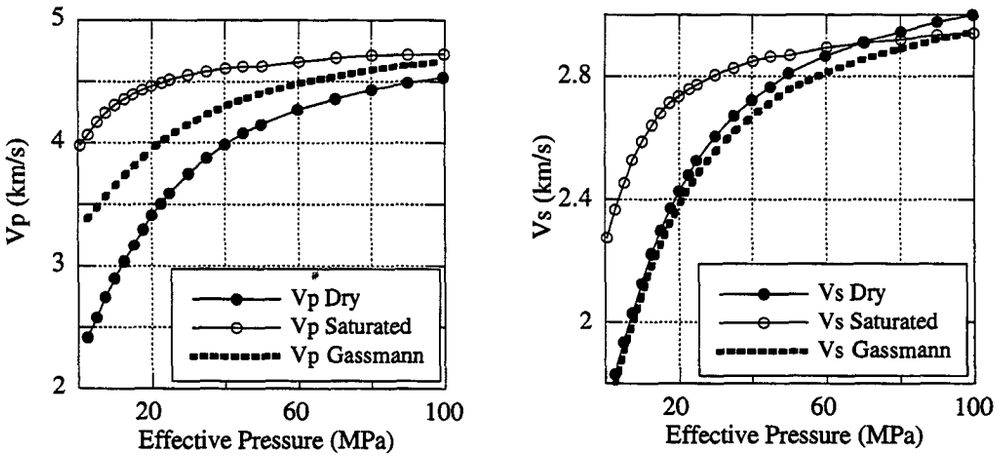


Figure 1. P- and S-wave velocities in Weber sandstone. Filled circles -- measured velocities in the dry rock; open circles -- measured ultrasonic velocities in the saturated rock; dashed lines -- calculated (Gassmann's equation) seismic velocities in the saturated rock.

We base our analysis of velocity-stress dependence on a dataset (Dataset 1) that includes more than 60 sandstone samples of porosity spanning from about 5% to 30%, and volumetric clay content spanning from 0 to 50% (measured by D.-H. Han, SRB Database). P- and S-wave velocities in the dry rocks were measured at effective hydrostatic pressure varying from 5 MPa to 50 MPa. In addition, we use a dataset (Dataset 2) that includes about 40 unconsolidated and weakly-cemented samples of porosity varying between 23 % and 38% (Blangy, 1992). In our analysis we deal with elastic moduli rather that with velocities. The M- and G-moduli are calculated from $V_p$ and $V_s$ as:

$$M = \rho V_p^2, G = \rho V_s^2, \tag{1}$$

where $\rho$ is the rock's density.

By plotting the difference between elastic moduli at two values of effective stress versus porosity, we obtain a somewhat counter-intuitive picture (Figure 2): this difference is close to zero at high porosity, and steadily increases with decreasing porosity. In other words, low-porosity sandstones are more sensitive to effective stress that high-porosity sandstones.

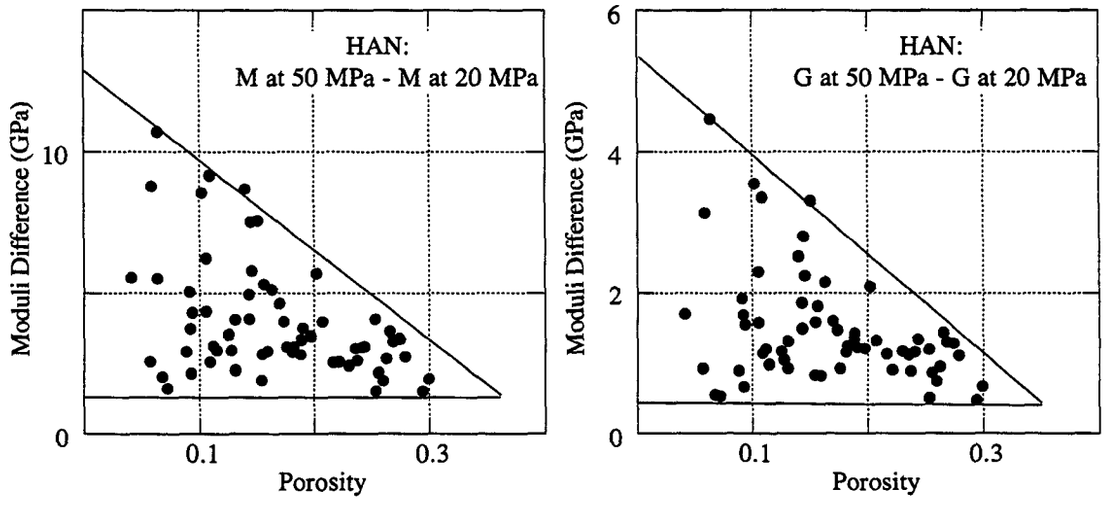


Figure 2. Dataset 1. Moduli difference between 50 MPa and 20 MPa.

The effect is surprising because one would expect that at zero porosity rock becomes pure solid whose elastic moduli should be only weakly stress-dependent. We explain this effect by suggesting that adding thin compliant cracks to solid grains will hardly change their local porosity (zero) but at the same time will significantly reduce their stiffness. Therefore, there is a "stiff" solid and a "soft" (cracked) solid. The elastic properties of these two hypothetical entities serve as the upper bound and the lower bound, respectively, for the actual solid phase of rock (Figure 3).

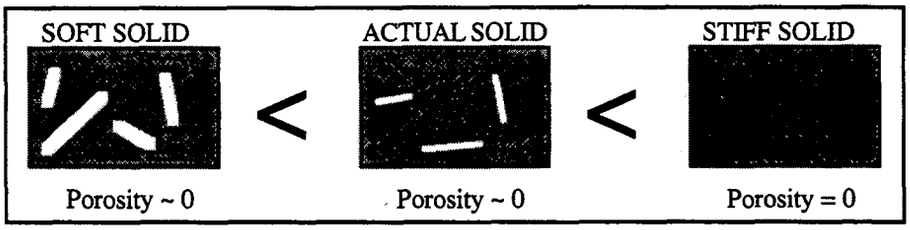


Figure 3. Soft solid, actual solid, and stiff (pure) solid. The values of the elastic moduli of the actual solid are between those of the soft solid and of the stiff solid.

Based on this observation we introduce a modified solid that is the "end member" at zero porosity. The elastic moduli of the modified solid are lower (due to microcracks) than those of the pure solid phase.

Finally, we quantify moduli-stress relations and suggest a recipe for constraining a velocity value at arbitrary effective stress from a single-point measurement (at given stress). The span between the upper and lower bounds in this estimate may be fairly large for low-porosity sandstones, but becomes narrow as porosity increases.

## CRITICAL POROSITY: IDEAS

Many advanced effective medium theories do not make explicit use of the fact that at zero confining pressure, in dry unconsolidated, uncemented granular materials elastic

moduli are zero and wave velocities are nonexistent. Therefore, elastic moduli curves (in the moduli-porosity plane) have to intercept the porosity axis at a certain terminal (critical) porosity ($\phi_c$). In sands, this critical porosity is about 0.38 -- the value close to the porosity of randomly packed identical spheres. Nur et al. (1991) state that this critical porosity value is a natural physical boundary for using effective medium relations in sandstones and sands. In other words, the predictive power of these relations may increase if they are used in porosity range between 0 and $\phi_c$, rather than between 0 and 1.

An example of using the critical porosity concept for modifying an effective medium theory is the modified Voigt average. In this case one has to operate in the domain $0 < \phi < \phi_c$ instead of $0 < \phi < 1$. The Voigt average can be interpreted as a linear interpolation between two end members -- one at $\phi = 0$ and another at $\phi = \phi_c$. The elastic modulus of rock (ether M- or G-modulus) approaches that of pure solid ($M_s$) at $\phi = 0$: $M = M_s$. It is zero (if effective stress $P$ is zero) at $\phi = \phi_c$: $M = 0$. By connecting these two points we arrive at the following relation between the modulus and porosity (line $P = 0$ in Figure 4, left):

$$M = M_s\left(1 - \frac{\phi}{\phi_c}\right) \tag{2}$$

It is reasonable to assume that the critical-porosity values of elastic moduli ($M_c$) are zero only at zero effective stress. They become positive ($M_c > 0$) and increase with increasing effective stress (Figure 4, left). In this case we modify formula (2) as:

$$M(P,\phi) = M_s(P)\left(1 - \frac{\phi}{\phi_c}\right) + M_c(P)\frac{\phi}{\phi_c}, \tag{3}$$

where we assume that the modulus of the solid phase also depends on the effective stress.

Let us finally assume that at any given effective stress, and for any fixed mineral composition this (the solid phase) modulus can vary between the modulus of the soft solid ($M_{sl}$) and that of the stiff solid ($M_{su}$): $M_{sl} < M_s < M_{su}$. At the same time we assume that the critical-porosity modulus $M_c$ is constant at given effective stress. By combining the last inequity with equation (3) we arrive at the following inequity:

$$M_{sl}(P)\left(1-\frac{\phi}{\phi_c}\right)+M_c(P)\frac{\phi}{\phi_c} < M(P,\phi) < M_{su}(P)\left(1-\frac{\phi}{\phi_c}\right)+M_c(P)\frac{\phi}{\phi_c}. \qquad (4)$$

This formula can be represented by a triangular region in the $(M,\phi)$ plane (Figure 4, right).

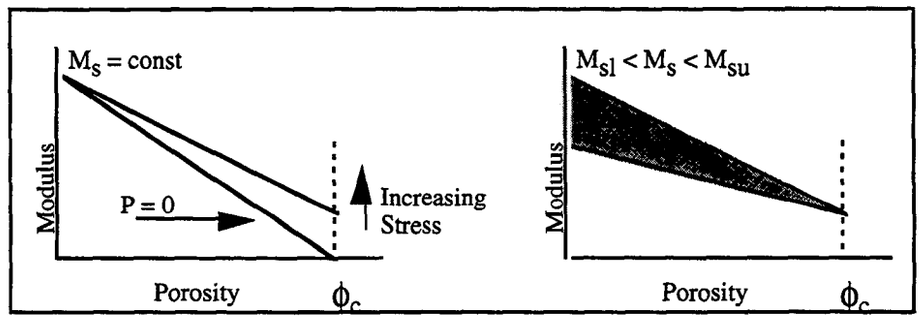


Figure 4. Left: Nur's critical porosity model with a constant solid phase modulus. Right: Varying solid phase modulus.

## CRITICAL POROSITY: FACTS

The heuristic speculations of the previous section can be justified only if they robustly explain the observed experimental trends.

In fact, these trends (Dataset 1) fit well into the framework provided by relation (4): in Figure 5 we can clearly see the triangles in the $(M,\phi)$ plane at effective stresses 5, 20, and 50 MPa, and for both M- and G-moduli.

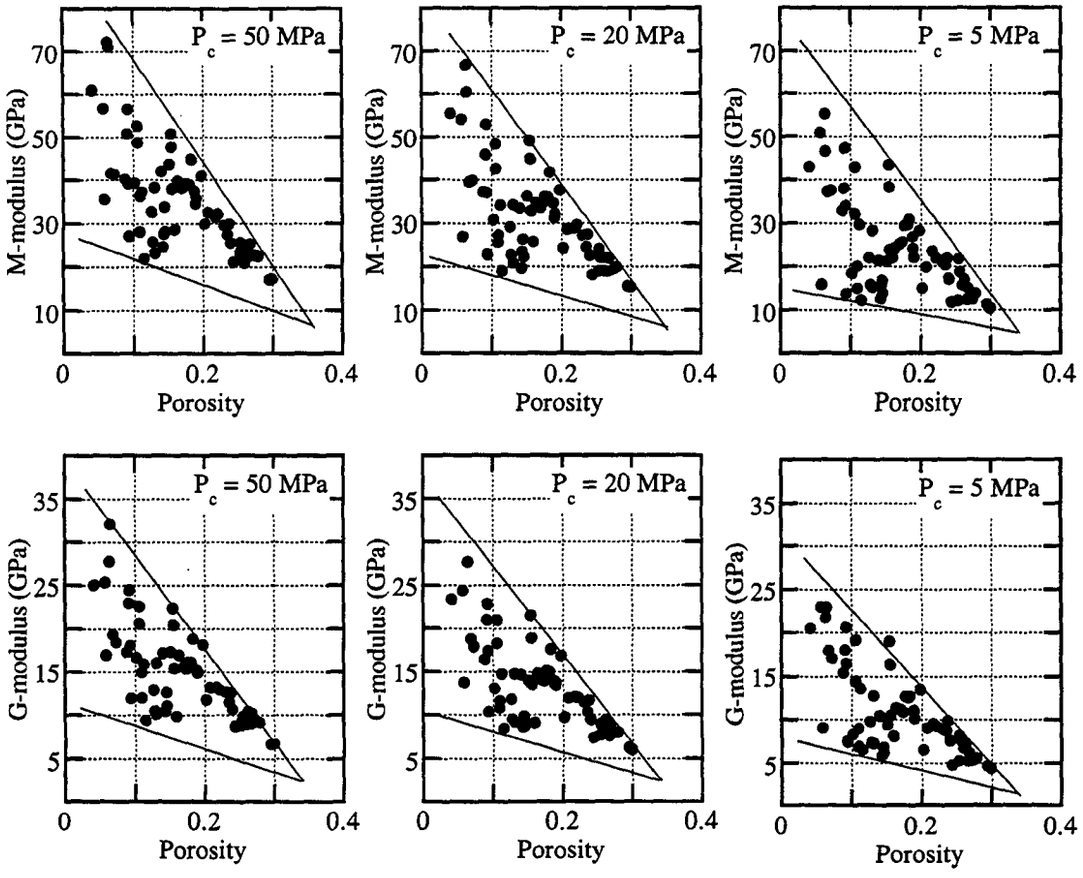


Figure 5. Dry-rock moduli from Dataset 1 at varying effective stress.

The large span of dry-rock moduli at small porosity, as observed in Figure 5, is not only due to the fact that there are "soft" and "stiff" solids, but also because of the varying mineralogy of the samples in Dataset 1: the volumetric clay content spans from 0 to 0.5. A convincing evidence to support the modified solid concept can be seen in Figure 6 where a subset of Dataset 1 is used. Here we used the relatively clean samples with clay content below 0.1. Still, the data points (for both M- and G-moduli) can be placed inside the triangles that have been produced based on the modified solid concept.

Similar triangles can be also seen if we raise the clay content window to cover the samples with clay content between 0.1 and 0.2 (Figure 7, left). In Figure 7, right, we give, for reference, the distribution of clay content for different porosities (Dataset 1).

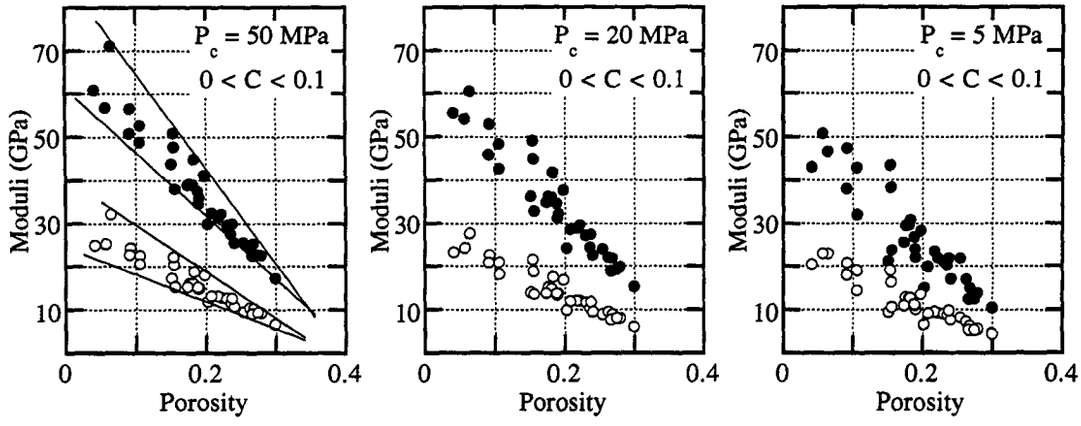


Figure 6. Elastic moduli for relatively clean samples from Dataset 1 at varying effective stress. Filled symbols: M-moduli; open symbols: G-moduli.

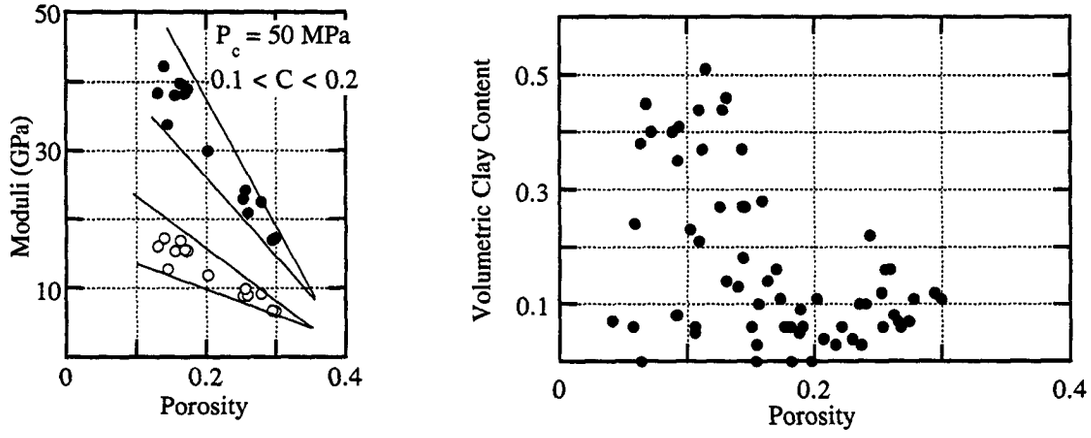


Figure 7. Dataset 1. Left: elastic moduli versus porosity at 50 MPa effective stress for the samples with clay content varying between 0.1 and 0.2. M-moduli -- filled circles, G-moduli -- open circles. Right: volumetric clay content versus porosity for all samples.

## STRESS SENSITIVITY OF MODULI

Below, we plot the difference between the elastic moduli at effective stress $P_1$ and effective stress $P_2$ for Dataset 1. We use $P_2$ = 10 MPa and vary $P_1$ between 20 MPa and

50 MPa. Again, the data points fit well inside triangles that open up as porosity approaches zero (Figures 8, 9, 10, and 11). It is interesting that the spans of these differential triangles do not depend on the amount of clay, although the absolute values of the elastic moduli do. Apparently, it is due to the fact that the spans of the solid phase elastic moduli only weakly depend on mineralogy (compare Figure 6, left, with $0 < C < 0.1$ to Figure 7, left, with $0.1 < C < 0.2$).

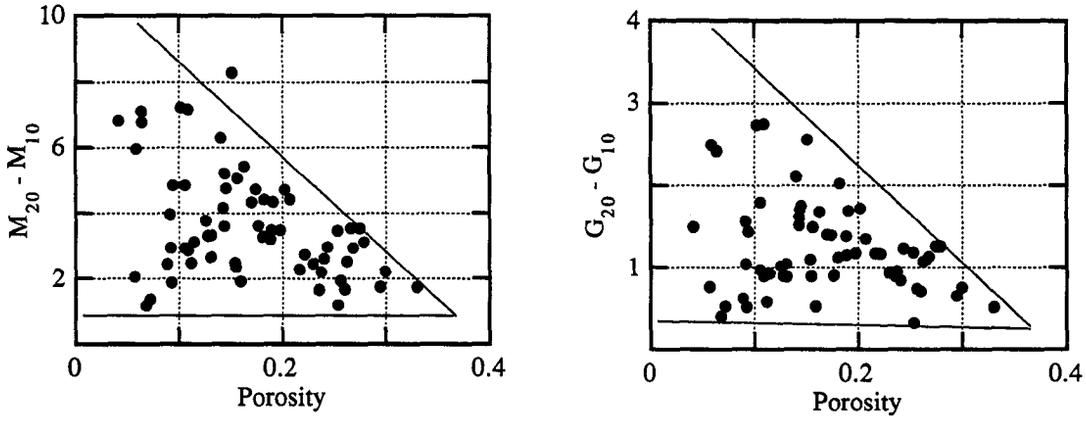


Figure 8. Dataset 1. M- and G-moduli difference between 20 MPa and 10 MPa.

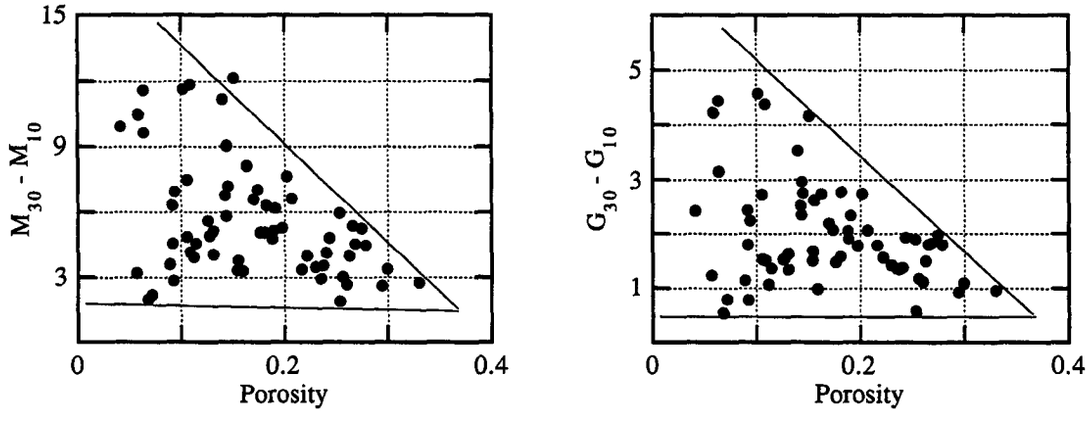


Figure 9. Dataset 1. M- and G-moduli difference between 30 MPa and 10 MPa.

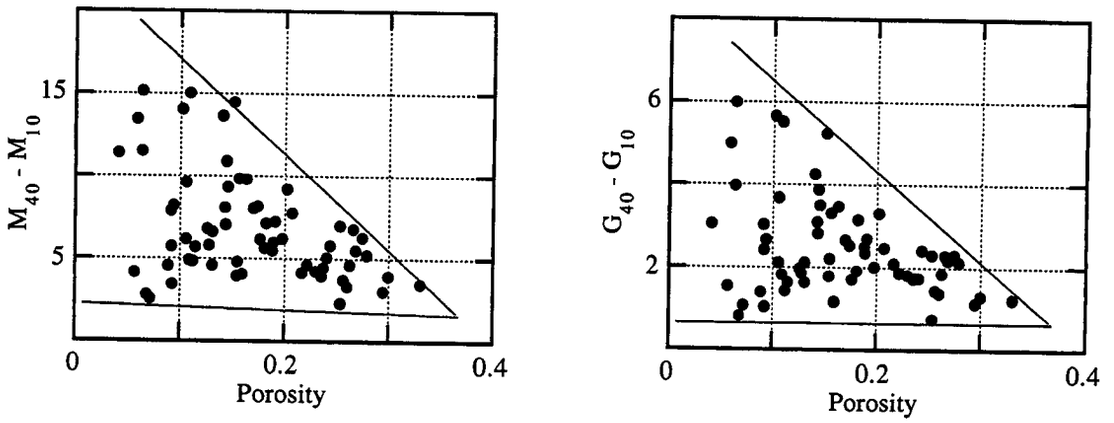


Figure 10. Dataset 1. M- and G-moduli difference between 40 MPa and 10 MPa.

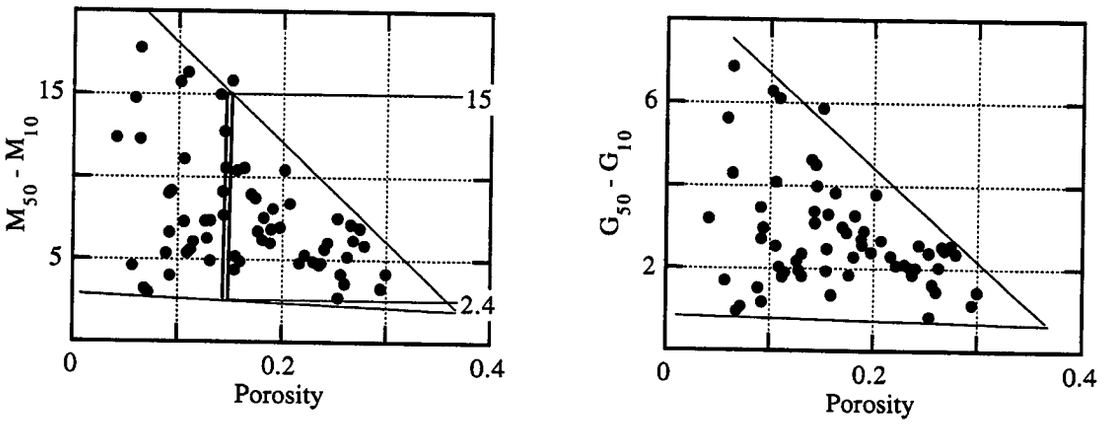


Figure 11. Dataset 1. M- and G-moduli difference between 50 MPa and 10 MPa.

A similar type of a differential-moduli-porosity relation can be seen in Figure 12 where we plotted the difference of the elastic moduli at 30 MPa and at 15 MPa for Dataset 1 and Dataset 2. Again, the sensitivity of the elastic moduli to stress increases with decreasing porosity.

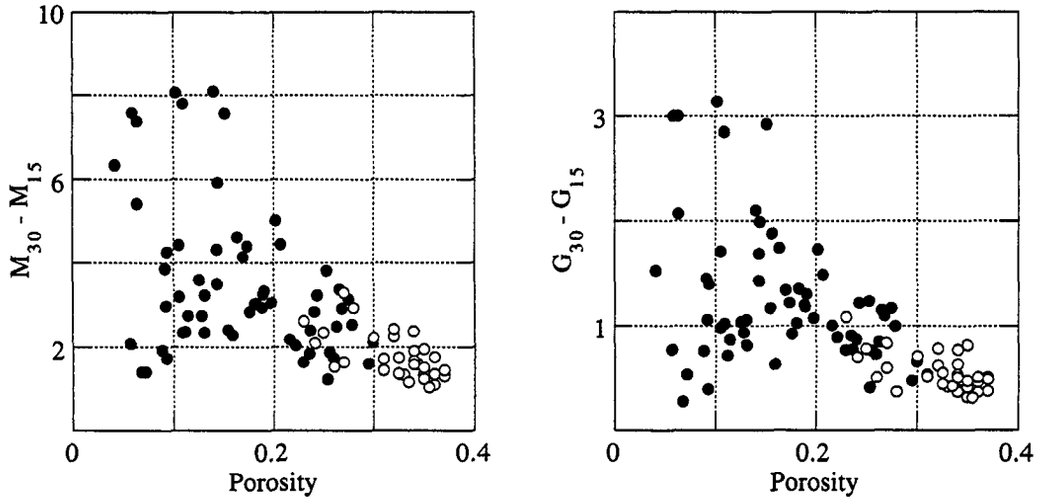


Figure 12. Datasets 1 and 2. M- and G-moduli difference between 30 MPa and 15 MPa. Filled circles -- Dataset 1, open circles -- Dataset 2.

The mathematical description of the differential triangles is readily available from formula (4): at effective stress $P_1$ we have

$$M_{sl}(P_1)\left(1-\frac{\phi}{\phi_c}\right)+M_c(P_1)\frac{\phi}{\phi_c}<M(P_1,\phi)<M_{su}(P_1)\left(1-\frac{\phi}{\phi_c}\right)+M_c(P_1)\frac{\phi}{\phi_c}, \quad (5)$$

at effective stress $P_2$ we have

$$M_{sl}(P_2)\left(1-\frac{\phi}{\phi_c}\right)+M_c(P_2)\frac{\phi}{\phi_c}<M(P_2,\phi)<M_{su}(P_2)\left(1-\frac{\phi}{\phi_c}\right)+M_c(P_2)\frac{\phi}{\phi_c}. \quad (6)$$

By subtracting formula (6) from formula (5) we arrive at the desired inequity

$$\left[M_{sl}(P_1)-M_{sl}(P_2)\right]\left(1-\frac{\phi}{\phi_c}\right)+\left[M_c(P_1)-M_c(P_2)\right]\frac{\phi}{\phi_c}<M(P_1,\phi)-M(P_2,\phi)$$
$$<\left[M_{su}(P_1)-M_{su}(P_2)\right]\left(1-\frac{\phi}{\phi_c}\right)+\left[M_c(P_1)-M_c(P_2)\right]\frac{\phi}{\phi_c}.$$

It is clear from the last formula that at critical porosity the difference between the two moduli (at stress $P_1$ and at stress $P_2$) is constant because the lower bound becomes equal to the upper bound. The largest span between the upper and the lower bounds takes place at zero porosity.

## PREDICTING VELOCITY FROM STRESS

Problem: Predict $V_p$ and $V_s$ at effective stress $P_1$ given $V_p$, $V_s$, and density $\rho$ at effective stress $P_2$. The porosity of the rock is $\phi$.

Solution: From a triangle similar to those in Figures 8 - 11 we find that at porosity $\phi$, the difference between two moduli $M(P_1,\phi)$ and $M(P_2,\phi)$ varies between the lower bound $A$ and the upper bound $B$:

$$A < M(P_1,\phi) - M(P_2,\phi) < B. \tag{7}$$

From inequity (7) we can find that

$$\frac{A}{M(P_2,\phi)} + 1 < \frac{M(P_1,\phi)}{M(P_2,\phi)} < \frac{A}{M(P_2,\phi)} + 1. \tag{8}$$

Finally, assuming that density is approximately constant at varying confining stress, we transform inequity (8) to the desired estimate for $V_p$ at $\phi$ and $P_1$:

$$\sqrt{\frac{A}{\rho} + V_p{}^2(P_2,\phi)} < V_p(P_1,\phi) < \sqrt{\frac{B}{\rho} + V_p{}^2(P_2,\phi)}. \tag{9}$$

Here moduli should be in GPa, density in kg/cm$^3$, and velocity in km/s.

A similar estimate can be derived for $V_s$.

Example: Consider a sandstone sample of porosity 0.15, dry-rock density 2.24 kg/cm$^3$, and dry-rock velocities $V_p$ = 3.53 km/s and $V_s$ = 2.26 km/s at effective stress 10 MPa. We find from Figures 8 - 11 (see illustration in Figure 11, left):

$$2.4 < M(50,0.15) - M(10,0.15) < 15, \qquad 0.8 < G(50,0.15) - G(10,0.15) < 5.5;$$

$$1.9 < M(40,0.15) - M(10,0.15) < 14, \qquad 0.6 < G(40,0.15) - G(10,0.15) < 5.4;$$

$$1.7 < M(30,0.15) - M(10,0.15) < 11, \qquad 0.5 < G(30,0.15) - G(10,0.15) < 4.3;$$

$$0.9 < M(20,0.15) - M(10,0.15) < 7, \qquad 0.3 < G(20,0.15) - G(10,0.15) < 2.8;$$

where the units of the elastic moduli are GPa, and those of effective pressure are MPa.

By substituting the above relations into formula (9) we arrive at the following estimates for velocities:

$$3.59 < V_p(20,0.15) < 3.95, \qquad 2.29 < V_s(20,0.15) < 2.52;$$
$$3.63 < V_p(30,0.15) < 4.17, \qquad 2.31 < V_s(30,0.15) < 2.65;$$
$$3.65 < V_p(40,0.15) < 4.32, \qquad 2.32 < V_s(40,0.15) < 2.74;$$
$$3.68 < V_p(50,0.15) < 4.37, \qquad 2.33 < V_s(50,0.15) < 2.75;$$

These estimates are plotted in Figure 13 for $V_p$ and $V_s$: if the velocities in sandstone are $V_p$ = 3.53 km/s and $V_s$ = 2.26 km/s at effective stress 10 MPa, then at higher stress their values lie within the bands between the upper and the lower bounds. These uncertainty intervals are fairly wide. Nevertheless, they reliably confine expected velocity-stress curves for sandstones. These intervals will become even wider for smaller porosities and will narrow for larger porosities. We recommend that these estimates be used for porosities varying from 0.05 to 0.3.

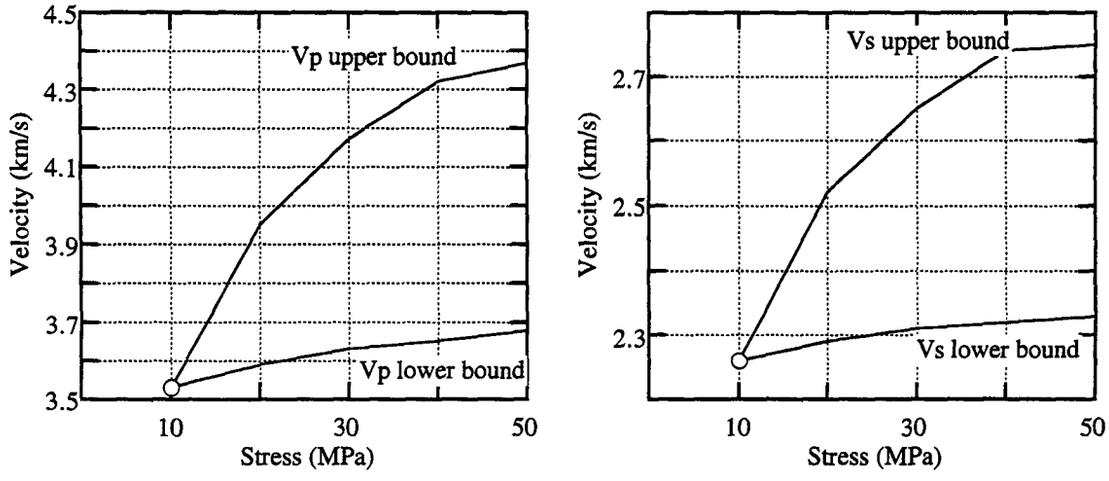


Figure 13. Predicted bounds for velocities in Example 1. Left: $V_p$, right: $V_s$.

## REFERENCES

Blangy, J. P., 1992, Integrated seismic lithologic interpretation: The petrophysical basis, Ph.D. thesis, Stanford University.

Coyner, K. B., 1977, Effects of stress, pore pressure, and pore fluids on bulk strain, velocity, and permeability in rocks, Ph.D. thesis, MIT.

Eberhart-Phillips, D. and Han, D.-H., 1989, Empirical relationships among seismic velocity, effective pressure, porosity, and clay content in sandstone, Geophysics, **54,** 82-89.

Nur, A., Marion, D., and Yin, H., 1991, Wave velocities in sediments, *in* Hovem, J. M., Richardson, M. D., and Stoll, R. D., eds., Shear waves in marine sediments: Kluwer Academic Publishers.

# APPENDIX A

## POROSITY, DENSITY, AND MINERAL CONTENT ABUNDANCE

The previously unpublished data from five Monterey Formation reservoirs in the San Joaquin Valley (Cymric, Asphalto, McKittrick, North and South Belridge) have similar modes of sample preparation for measurements of porosity, density, and mineral content abundance. The properties of the Cymric, Asphalto, and McKittrick reservoir samples were determined for this study; the North and South Belridge data were supplied by Shell and Mobil.

The weight percent of the minerals which in all these samples were determined with Fourier Transform Infrared Spectroscopy (FTIR), discussed by Harville and Freeman, (1988). Weight percents of different minerals are reproducable within 5%. Pore fluids in all samples were removed by Dean Stark by Corelabs, which involves cleaning the samples with boiling toluene at approximately 115° C and then removing the remainder of the oil with methylene chloride which boils at about 45° C. All samples were dried in either a humidity controlled oven or a convection oven at approximately 115° C for between four and 48 hours. FTIR analyses show that waters of hydration remain bound to both opal and clay minerals. The samples from Cymric, McKittrick, and Asphalto were cut into cylinderical plugs with a saw blade lubricated with liquid nitrogen. After preparation, all samples were kept room-dry.

In determining porosity and density, the weight of the matrix was determined after all pore fluids were extracted; both grain volume and porosity were determined using Boyle's law and helium as the gaseous medium. Dry ulk density ($\rho_b$) was calculated from porosity ($\phi$) and grain density ($\rho_s$) according to $\rho_b = \rho_s(1-\phi)$.

# FTIR DATA IN WEIGHT PERCENT

CYMRIC FIELD (well 1407R-1Y, Sec1-T29S/R21E)

| depth (ft) | phi | bulk density | opal-A | opal-CT | quartz | albite | ksp | andes-ine | total fsp | kaol | chl | ill+ smc | total clay | calcite | pyrite | anal-cime |
|---|---|---|---|---|---|---|---|---|---|---|---|---|---|---|---|---|
| 1240.3 | 0.52 | 1.09 | 0.42 | 0 | 0 | 0.06 | 0 | 0.10 | 0.16 | 0 | 0 | 0 | 0 | 0 | 0.01 | 0.41 |
| 1240.7 | 0.666 | 0.75 | 0.53 | 0.25 | 0.02 | 0 | 0.08 | 0 | 0.08 | 0.01 | 0.03 | 0.07 | 0.11 | 0 | 0.01 | 0 |
| 1242.8 | 0.625 | 0.89 | 0 | 0.74 | 0 | 0.08 | 0.04 | 0 | 0.12 | 0 | 0.07 | 0.07 | 0.14 | 0 | 0 | 0 |
| 1246.7 | 0.628 | 0.84 | 0.25 | 0.47 | 0 | 0.05 | 0.05 | 0 | 0.1 | 0 | 0.06 | 0.12 | 0.18 | 0 | 0 | 0 |
| 1248.7 | 0.656 | 0.80 | 0.41 | 0.36 | 0 | 0.06 | 0.04 | 0 | 0.1 | 0 | 0.05 | 0.08 | 0.13 | 0 | 0 | 0 |
| 1249.0 | 0.646 | 0.80 | 0.72 | 0.16 | 0 | 0 | 0.04 | 0 | 0.04 | 0 | 0.04 | 0.04 | 0.08 | 0 | 0 | 0 |
| 1249.3 | 0.683 | 0.70 | 0.57 | 0.28 | 0 | 0 | 0 | 0.05 | 0.05 | 0 | 0 | 0 | 0 | 0 | 0.01 | 0.09 |
| 1255.2 | 0.654 | 0.78 | 0 | 0.77 | 0 | 0.08 | 0 | 0 | 0.08 | 0 | 0.07 | 0.08 | 0.15 | 0 | 0 | 0 |
| 1256.3 | 0.645 | 0.80 | 0.23 | 0.49 | 0 | 0.07 | 0.07 | 0 | 0.14 | 0 | 0.06 | 0.06 | 0.12 | 0 | 0.02 | 0 |
| 1257.7 | 0.553 | 1.01 | 0 | 0.78 | 0 | 0.07 | 0 | 0 | 0.07 | 0 | 0.08 | 0.07 | 0.15 | 0 | 0 | 0 |
| 1259.2 | 0.59 | 0.94 | 0 | 0.64 | 0 | 0.10 | 0.03 | 0 | 0.13 | 0 | 0.10 | 0.12 | 0.22 | 0.01 | 0 | 0 |

ASPHALTO (well 332X-25Z, Sec25-T30S/R22E)

| depth (ft) | phi | bulk density | opal-CT | quartz | albite | andes-ine | ksp | total fsp | kaol | chl | ill+ smc | total clay | carb-onate | apatite +halite | pyrite | organ-ics |
|---|---|---|---|---|---|---|---|---|---|---|---|---|---|---|---|---|
| 5874.5 | 0.219 | 1.99 | 0 | 0.548 | 0.101 | 0 | 0.044 | 0.145 | 0.071 | 0.023 | 0.13 | 0.22 | 0 | 0.005 | 0.032 | 0.04 |
| 5876.5 | 0.266 | 1.86 | 0 | 0.7 | 0 | 0.06 | 0.09 | 0.15 | 0.03 | 0 | 0.1 | 0.13 | 0 | 0 | 0.02 | 0 |
| 5887.3 | 0.212 | 1.97 | 0 | 0.65 | 0.04 | 0.03 | 0.07 | 0.14 | 0.03 | 0 | 0.15 | 0.18 | 0.01 | 0 | 0.02 | 0 |
| 5892.5 | 0.223 | 1.96 | 0 | 0.67 | 0 | 0.04 | 0.08 | 0.12 | 0.03 | 0 | 0.15 | 0.18 | 0 | 0 | 0.03 | 0 |
| 5900.4 | 0.152 | 2.15 | 0 | 0.46 | 0.06 | 0.04 | 0.08 | 0.18 | 0.07 | 0 | 0.24 | 0.31 | 0.02 | 0 | 0.03 | 0 |
| 5904.4 | 0.210 | 1.88 | mineralogy not determined | | | | | | | | | | | | | |
| 5913.7 | 0.149 | 2.16 | 0 | 0.423 | 0.104 | 0 | 0.058 | 0.162 | 0.093 | 0. 44 | 0.159 | 0.296 | 0.044 | 0.006 | 0.034 | 0.043 |
| 5916.5 | 0.259 | 1.88 | 0 | 0.67 | 0.06 | 0.02 | 0.05 | 0.13 | 0.05 | 0 | 0.12 | 0.17 | 0 | 0 | 0.03 | 0 |
| 5931.5 | 0.327 | 1.72 | 0.146 | 0.57 | 0.063 | 0 | 0.033 | 0.096 | 0.035 | 0. 28 | 0.052 | 0.115 | 0.022 | 0.004 | 0.018 | 0.035 |
| 5932.5 | 0.254 | 1.90 | 0.186 | 0.545 | 0.07 | 0 | 0.035 | 0.105 | 0.032 | 0. 21 | 0.044 | 0.097 | 0.013 | 0.005 | 0.017 | 0.029 |
| 5937.5 | 0.195 | 1.96 | 0.464 | 0.362 | 0.055 | 0 | 0.019 | 0.074 | 0.014 | 0.011 | 0.035 | 0.06 | 0 | 0.004 | 0.012 | 0.023 |
| 5942.1 | 0.445 | 1.42 | 0.31 | 0.446 | 0.033 | 0 | 0 | 0.033 | 0.019 | 0.016 | 0.097 | 0.132 | 0.033 | 0.006 | 0.014 | 0.039 |
| 5957.3 | 0.228 | 1.96 | 0 | 0.664 | 0.084 | 0 | 0.042 | 0.126 | 0.046 | 0.028 | 0.062 | 0.136 | 0.012 | 0.004 | 0.024 | 0.036 |
| 5958.2 | 0.296 | 1.82 | 0.321 | 0.44 | 0.054 | 0 | 0.003 | 0.057 | 0.013 | 0.009 | 0.084 | 0.106 | 0.038 | 0.004 | 0.017 | 0.025 |

Abbreviations: phi: porosity, ksp: potassium feldspar, kaol: kaolinite, chl: chlorite, ill: illite, smc: smectite

MCKITTRICK FIELD (well 342-17Z at Sec17Z-T30S/R22E)

| depth (ft) | Phi | bulk density | opal-A | opal-CT | crist-obalite | albite | kspar | oligo-clase | total fsp | kaol | smc | chl | total clay | cal-cite | pyrite |
|---|---|---|---|---|---|---|---|---|---|---|---|---|---|---|---|
| 3248.5 | 0.390 | 1.38 | 0 | 0.67 | 0 | 0 | 0.04 | 0.18 | 0.22 | 0.03 | 0.06 | 0 | 0.09 | 0 | 0.02 |
| 3255.5 | 0.454 | 1.20 | 0 | 0.88 | 0 | 0 | 0 | 0.12 | 0.12 | 0 | 0 | 0 | 0 | 0 | 0 |
| 3262.5 | 0.333 | 1.45 | 0 | 0.97 | 0 | 0 | 0 | 0 | 0 | 0 | 0 | 0.03 | 0.03 | 0 | 0 |
| 3268.5 | 0.373 | 1.47 | 0 | 0.95 | 0 | 0 | 0 | 0.05 | 0.05 | 0 | 0 | 0 | 0 | 0 | 0 |
| 3273.5 | 0.341 | 1.47 | 0 | 0.71 | 0 | 0 | 0.02 | 0.17 | 0.19 | 0.01 | 0.09 | 0 | 0.1 | 0 | 0 |
| 3306.0 | 0.348 | 1.46 | 0 | 0.71 | 0 | 0.1 | 0.05 | 0 | 0.15 | 0.05 | 0.04 | 0.03 | 0.12 | 0 | 0.02 |
| 3317.5 | 0.394 | 1.35 | 0 | 0.86 | 0 | 0 | 0 | 0 | 0 | 0.02 | 0.05 | 0.07 | 0.14 | 0 | 0 |
| 3337.5 | 0.367 | 1.38 | 0 | 0.95 | 0 | 0 | 0 | 0 | 0 | 0 | 0 | 0.05 | 0.05 | 0 | 0 |
| 3600.5 | 0.416 | 1.33 | 0 | 0.75 | 0 | 0 | 0.02 | 0.11 | 0.13 | 0.01 | 0.06 | 0.05 | 0.12 | 0 | 0 |
| 3603.5 | 0.433 | 1.27 | 0 | 0.9 | 0 | 0 | 0.04 | 0 | 0.04 | 0 | 0 | 0.06 | 0.06 | 0 | 0 |
| 3606.5 | 0.416 | 1.31 | 0 | 0.9 | 0 | 0 | 0 | 0 | 0 | 0.03 | 0 | 0.07 | 0.10 | 0 | 0 |
| 3670.5 | 0.337 | 1.49 | 0 | 0.72 | 0.11 | 0 | 0.05 | 0 | 0.05 | 0.01 | 0.04 | 0.07 | 0.12 | 0 | 0 |
| 3678.5 | 0.358 | 1.48 | 0 | 0.67 | 0 | 0.08 | 0.02 | 0.04 | 0.14 | 0.04 | 0.09 | 0.04 | 0.17 | 0.02 | 0 |
| 3681.0 | 0.343 | 1.51 | 0 | 0.65 | 0 | 0.12 | 0 | 0 | 0.12 | 0.05 | 0.14 | 0.04 | 0.23 | 0 | 0 |
| 3684.5 | 0.418 | 1.33 | 0 | 0.76 | 0.11 | 0 | 0 | 0 | 0 | 0.03 | 0 | 0.1 | 0.13 | 0 | 0 |

NORTH BELRIDGE (SWEPI well 565S1, Sec1-T28S/R20E)

| depth (ft) | Phi | bulk density | opal-A | opal-CT | quartz | albite | ksp | andes-ine | total fsp | kaol | ill+smc | total clay | dolo-mite | pyrite |
|---|---|---|---|---|---|---|---|---|---|---|---|---|---|---|
| 1257 | 0.614 | 0.922 | 0.53 | 0 | 0.05 | 0.08 | 0.07 | 0.09 | 0.24 | 0.03 | 0.21 | 0.24 | 0.04 | 0.02 |
| 1301 | 0.475 | 1.323 | 0.21 | 0 | 0.2 | 0 | 0.11 | 0.19 | 0.30 | 0 | 0.16 | 0.16 | 0 | 0.02 |
| 1350 | 0.52 | 1.186 | 0.3 | 0 | 0.05 | 0.09 | 0.14 | 0.20 | 0.43 | 0.07 | 0.22 | 0.29 | 0.02 | 0.02 |
| 1695 | 0.55 | 1.107 | 0.36 | 0 | 0.08 | 0 | 0.16 | 0.10 | 0.26 | 0 | 0.20 | 0.20 | 0 | 0.01 |
| 1745 | 0.615 | 0.916 | 0.49 | 0 | 0.09 | 0.09 | 0.08 | 0.08 | 0.25 | 0 | 0.26 | 0.26 | 0 | 0 |
| 1761 | 0.634 | 0.871 | 0.57 | 0 | 0.08 | 0 | 0.08 | 0.08 | 0.16 | 0.03 | 0.12 | 0.15 | 0 | 0.02 |
| 1796 | 0.552 | 1.093 | 0.42 | 0 | 0.12 | 0 | 0.07 | 0.07 | 0.14 | 0.04 | 0.22 | 0.26 | 0 | 0.02 |
| 1920 | 0.686 | 0.725 | 0.66 | 0 | 0.06 | 0 | 0.06 | 0.06 | 0.12 | 0.02 | 0.13 | 0.15 | 0 | 0 |
| 1975 | 0.535 | 1.116 | 0.33 | 0.21 | 0.07 | 0 | 0.06 | 0.06 | 0.12 | 0.06 | 0.17 | 0.23 | 0 | 0.01 |
| 2010 | 0.567 | 1.048 | 0 | 0.61 | 0.02 | 0 | 0.05 | 0.05 | 0.10 | 0.04 | 0.14 | 0.18 | 0 | 0.02 |
| 2107 | 0.495 | 1.242 | 0 | 0.47 | 0 | 0 | 0.11 | 0.11 | 0.22 | 0.05 | 0.21 | 0.26 | 0 | 0.03 |
| 2121 | 0.415 | 1.48 | 0 | 0.29 | 0.07 | 0 | 0.07 | 0.07 | 0.14 | 0.08 | 0.33 | 0.41 | 0.02 | 0.02 |
| 2493 | 0.445 | 1.387 | 0 | 0.35 | 0.06 | 0.07 | 0.12 | 0.12 | 0.31 | 0.05 | 0.21 | 0.26 | 0 | 0.02 |

SOUTH BELRIDGE (Belridge V well 8360A-2, Sec2-T29S/R21E

| depth (ft) | Phi | bulk density | opal-A | opal-CT | quartz | albite | kspar | andes-ine | total fsp | kaol | smc | chl | total clay | carb-onate | pyrite |
|---|---|---|---|---|---|---|---|---|---|---|---|---|---|---|---|
| 1694 | 0.577 | 0.981 | 0.44 | 0 | 0.08 | 0 | 0.12 | 0.04 | 0.16 | 0.05 | 0.23 | 0 | 0.28 | 0 | 0.04 |
| 1714 | 0.572 | 1.001 | 0.42 | 0 | 0.1 | 0 | 0.11 | 0.03 | 0.14 | 0.04 | 0.25 | 0 | 0.29 | 0 | 0.05 |
| 1820 | 0.46 | 1.312 | 0.32 | 0 | 0.09 | 0 | 0.11 | 0.06 | 0.17 | 0.05 | 0.31 | 0 | 0.36 | 0.03 | 0.03 |
| 1832 | 0.532 | 1.119 | 0.34 | 0 | 0.08 | 0 | 0.14 | 0.1 | 0.24 | 0.05 | 0.25 | 0 | 0.3 | 0 | 0.04 |
| 1836 | 0.586 | 0.973 | 0.36 | 0 | 0.09 | 0 | 0.14 | 0.08 | 0.22 | 0.05 | 0.25 | 0 | 0.3 | 0 | 0.03 |
| 1846 | 0.522 | 1.147 | 0.4 | 0 | 0.08 | 0 | 0.11 | 0.06 | 0.17 | 0.07 | 0.24 | 0 | 0.31 | 0.02 | 0.02 |
| 1852 | 0.477 | 1.281 | 0.23 | 0 | 0.07 | 0 | 0.13 | 0.1 | 0.23 | 0.07 | 0.35 | 0 | 0.42 | 0.03 | 0.02 |
| 1882 | 0.606 | 0.894 | 0.36 | 0.21 | 0 | 0.04 | 0.07 | 0.05 | 0.16 | 0.04 | 0.18 | 0.03 | 0.25 | 0 | 0.02 |
| 1895 | 0.57 | 0.989 | 0.27 | 0.25 | 0.02 | 0.05 | 0.07 | 0.03 | 0.15 | 0.05 | 0.21 | 0 | 0.26 | 0.02 | 0.03 |
| 1906 | 0.443 | 1.287 | 0 | 0.41 | 0.04 | 0.06 | 0.09 | 0 | 0.15 | 0.08 | 0.24 | 0.04 | 0.36 | 0.02 | 0.02 |
| 1930 | 0.411 | 1.443 | 0.19 | 0.23 | 0 | 0.07 | 0.08 | 0.06 | 0.21 | 0.07 | 0.23 | 0.04 | 0.34 | 0 | 0.03 |
| 1956 | 0.503 | 1.158 | 0 | 0.28 | 0.07 | 0.07 | 0.09 | 0.05 | 0.21 | 0.09 | 0.28 | 0.02 | 0.39 | 0.03 | 0.02 |
| 1976 | 0.44 | 1.316 | 0 | 0.37 | 0 | 0.08 | 0.08 | 0 | 0.16 | 0.09 | 0.27 | 0.07 | 0.43 | 0.02 | 0.02 |

NORWEGIAN NORTH SEA #1 (well 7117/9-1)

| depth (m) | bulk density | opal-A | opal-CT | chert | quartz | albite | ksp | andes-ine | oligo-clase | total fsp | kaol | smc | chl | total clay | calcite | pyrite |
|---|---|---|---|---|---|---|---|---|---|---|---|---|---|---|---|---|
| 1330 | 2.47 | 0.34 | 0 | 0 | 0.13 | 0 | 0.08 | 0 | 0 | 0.08 | 0.07 | 0.36 | 0 | 0.43 | 0 | 0.02 |
| 1395 | 2.49 | 0 | 0.34 | 0 | 0.12 | 0.08 | 0.07 | 0 | 0 | 0.15 | 0.09 | 0.21 | 0.07 | 0.37 | 0.02 | 0 |
| 1425 | 2.42 | 0 | 0.58 | 0 | 0 | 0 | 0.06 | 0 | 0 | 0.06 | 0.07 | 0.23 | 0.04 | 0.34 | 0 | 0.02 |
| 1460 | 2.41 | 0 | 0.59 | 0 | 0 | 0 | 0.09 | 0 | 0 | 0.09 | 0.11 | 0.15 | 0.06 | 0.32 | 0 | 0 |
| 1486 | 2.41 | 0 | 0.63 | 0 | 0 | 0 | 0.07 | 0 | 0.03 | 0.1 | 0.09 | 0.11 | 0.07 | 0.27 | 0 | 0 |
| 1521 | 2.45 | 0 | 0.55 | 0 | 0 | 0 | 0.05 | 0 | 0 | 0.05 | 0.09 | 0.18 | 0.11 | 0.38 | 0 | 0.02 |
| 1560 | 2.41 | 0 | 0.59 | 0 | 0 | 0 | 0.08 | 0 | 0.05 | 0.13 | 0.1 | 0.15 | 0.03 | 0.28 | 0 | 0 |
| 1646 | 2.42 | 0 | 0.57 | 0.07 | 0 | 0 | 0.09 | 0 | 0 | 0.09 | 0.07 | 0.13 | 0.07 | 0.27 | 0 | 0 |
| 1678 | 2.51 | 0 | 0.26 | 0.14 | 0.2 | 0 | 0.09 | 0 | 0 | 0.09 | 0.08 | 0.18 | 0.05 | 0.31 | 0 | 0 |
| 1711 | 2.61 | 0 | 0 | 0.35 | 0.18 | 0 | 0.07 | 0 | 0 | 0.07 | 0.08 | 0.27 | 0.05 | 0.4 | 0 | 0 |
| 1730 | 2.55 | 0 | 0.13 | 0.52 | 0.03 | 0 | 0.05 | 0 | 0 | 0.05 | 0.06 | 0.17 | 0.04 | 0.27 | 0 | 0 |
| 1745 | 2.59 | 0 | 0 | 0.69 | 0 | 0 | 0.03 | 0 | 0 | 0.03 | 0.06 | 0.19 | 0.03 | 0.28 | 0 | 0 |
| 1760 | 2.63 | 0 | 0 | 0.13 | 0.5 | 0.06 | 0.08 | 0.01 | 0 | 0.15 | 0 | 0.1 | 0 | 0.1 | 0.12 | 0 |
| 1776 | 2.59 | 0 | 0 | 0.45 | 0.02 | 0 | 0 | 0 | 0.18 | 0.18 | 0.03 | 0.28 | 0.04 | 0.35 | 0 | 0 |
| 1780 | 2.6 | 0 | 0 | 0.61 | 0 | 0 | 0 | 0 | 0.08 | 0.08 | 0 | 0.24 | 0.07 | 0.31 | 0 | 0 |
| 1795 | 2.59 | 0 | 0 | 0.61 | 0 | 0 | 0 | 0 | 0 | 0 | 0.09 | 0.24 | 0.06 | 0.39 | 0 | 0 |
| 1805 | 2.56 | 0 | 0.12 | 0.44 | 0 | 0 | 0.03 | 0.05 | 0 | 0.08 | 0.07 | 0.23 | 0.03 | 0.33 | 0.03 | 0 |
| 1816 | 2.62 | 0 | 0 | 0.17 | 0.42 | 0.08 | 0.09 | 0 | 0 | 0.17 | 0.01 | 0.15 | 0.03 | 0.19 | 0.05 | 0 |

| NORWEGIAN NORTH SEA #2 (well 7117/9-2) | | | | | | | | | | | | | | | | |
|---|---|---|---|---|---|---|---|---|---|---|---|---|---|---|---|---|
| depth (m) | bulk density | opal-A | opal-CT | chert | quartz | albite | ksp | andes-ine | oligo-clase | total fsp | kaol | smc | chl | total clay | calcite | pyrite |
| 1025.0 | 2.44 | 0 | 0.52 | 0 | 0 | 0.08 | 0 | 0 | 0 | 0.08 | 0.03 | 0.35 | 0 | 0.38 | 0 | 0.02 |
| 1089.0 | 2.47 | 0 | 0.34 | 0 | 0.07 | 0.09 | 0.03 | 0 | 0 | 0.12 | 0.08 | 0.39 | 0 | 0.47 | 0 | 0 |
| 1105.0 | 2.49 | 0 | 0.31 | 0 | 0.16 | 0.06 | 0.09 | 0 | 0 | 0.15 | 0.01 | 0.37 | 0 | 0.38 | 0 | 0 |
| 1113.0 | 2.46 | 0.29 | 0 | 0 | 0.09 | 0 | 0.14 | 0.03 | 0 | 0.17 | 0 | 0.45 | 0 | 0.45 | 0 | 0 |
| 1125.0 | 2.49 | 0 | 0.36 | 0 | 0.06 | 0 | 0.08 | 0 | 0.05 | 0.13 | 0.09 | 0.3 | 0.04 | 0.43 | 0.02 | 0 |
| 1132.0 | 2.4 | 0 | 0.62 | 0 | 0 | 0 | 0.06 | 0 | 0.05 | 0.11 | 0.09 | 0.12 | 0.06 | 0.27 | 0 | 0 |
| 1165.0 | 2.38 | 0 | 0.68 | 0 | 0 | 0 | 0.08 | 0 | 0 | 0.08 | 0.05 | 0.15 | 0.04 | 0.24 | 0 | 0 |
| 1195.0 | 2.62 | 0 | 0 | 0 | 0.33 | 0 | 0.07 | 0 | 0 | 0.07 | 0.1 | 0.41 | 0.09 | 0.6 | 0 | 0 |
| 1385.0 | 2.76 | 0 | 0 | 0.15 | 0.14 | 0.09 | 0.1 | 0 | 0 | 0.19 | 0.09 | 0.29 | 0 | 0.38 | 0 | 0.14 |
| 1392.0 | 2.66 | 0.2 | 0 | 0 | 0.15 | 0 | 0.08 | 0 | 0 | 0.08 | 0.08 | 0.31 | 0.04 | 0.43 | 0 | 0.14 |
| 1396.0 | 2.64 | 0 | 0 | 0 | 0.4 | 0.13 | 0.13 | 0.02 | 0 | 0.28 | 0.1 | 0.16 | 0.04 | 0.3 | 0 | 0.02 |
| 1414.0 | 2.64 | 0 | 0 | 0 | 0.22 | 0.13 | 0.06 | 0.05 | 0 | 0.24 | 0.08 | 0.29 | 0.11 | 0.48 | 0.04 | 0.02 |
| 1458.0 | 2.62 | 0 | 0 | 0 | 0.26 | 0.11 | 0.05 | 0.03 | 0 | 0.19 | 0.15 | 0.27 | 0.11 | 0.53 | 0.02 | 0 |
| 1492.0 | 2.63 | 0 | 0 | 0.1 | 0.25 | 0.17 | 0.08 | 0.06 | 0 | 0.31 | 0.06 | 0.21 | 0.06 | 0.33 | 0 | 0.01 |
| 1521.0 | 2.66 | 0 | 0 | 0.13 | 0.06 | 0.14 | 0.04 | 0.05 | 0 | 0.23 | 0.08 | 0.45 | 0 | 0.53 | 0 | 0.05 |
| 1654.0 | 2.68 | 0 | 0 | 0.15 | 0.11 | 0.11 | 0.05 | 0 | 0 | 0.16 | 0.13 | 0.33 | 0.06 | 0.52 | 0 | 0.06 |
| 1675.0 | 2.62 | 0 | 0 | 0.11 | 0.27 | 0.2 | 0.07 | 0 | 0.06 | 0.33 | 0.08 | 0.16 | 0.05 | 0.29 | 0 | 0 |
| 1695.0 | 2.63 | 0 | 0 | 0.16 | 0.12 | 0.17 | 0.07 | 0.03 | 0 | 0.27 | 0.1 | 0.31 | 0.03 | 0.44 | 0 | 0.01 |

Additional abbreviations: carbonate: calcite+ dolomite

# APPENDIX B

# DENSITY & SOLID-PHASE MODULI OF ROCK-FORMING MINERALS

In modeling any rock composed of more than one mineral, it is necessary to calculate the moduli of the solid phase for each sample as a function of the abundance of the constituent minerals. These rocks contain opal-A, opal-CT, quartz, several clay minerals, feldspars, carbonates, pyrite, analcime, and organic matter. The references for the elastic moduli of these minerals are shown in the table below. The elastic moduli of opal-CT at zero porosity were determined from two plugs of a hydrothermally formed sample from Nevada (this study). Because no ultrasonic velocities were measured on a sample of 100% opal-A, the same properties are used for opal-A and opal-CT. The assumption that the elastic properties of opal-CT can be used for opal-A is a poor but necessary assumption. The data for clay minerals is from a montmorillonite/illite mixutre.

| | opal-A/CT | quartz | fsp $Or_{79}Ab_{19}An_2$ | Clay | carbonate (calcite) | pyrite | organics | analcime |
|---|---|---|---|---|---|---|---|---|
| rho (g/cc) | 2.0 | 2.649 | 2.56 | 2.6 | 2.712 | 5.1 | 1.3 | 2.712 |
| Vp (km/s) | 3.935 | 6.05 | 5.91 | 3.6 | 6.53 | 7.3 | 2.25 | 5.78 |
| Vs (km/s) | 2.508 | 4.09 | 3.25 | 1.85 | 3.36 | 5.2 | 1.45 | 3.11 |
| K (GPa) | 14.219 | 37.88 | 53.36 | 21.83 | 74.82 | 87.91 | 2.937 | 55.629 |
| G (GPa) | 12.580 | 44.31 | 27.04 | 8.899 | 30.62 | 137.9 | 2.733 | 26.231 |
| reference | this study | McSkimm et al, 1965 | Ryzhova, et al, 1965 | Castagna et al, 1985 | Dandekar, 1968 | Simmons and Birch, 1963 | Blangy, 1992 | Hughes and Maurette, 1957 |

Before calculating the modulus of the solid phase for each sample, the constants in this table are used to convert the abundances of the rock forming minerals in each sample from weight fraction, shown in Appendix A, to volume fraction. The volume fraction of each mineral, $v_i$, is

$$v_i = \frac{w_i}{\rho_i} \Big/ \sum_{i=1}^{N} \frac{w_i}{\rho_i}$$

where $w_i$ is the weight fraction and $\rho_i$ is the density of each mineral. Because the solid-phase moduli is only used in modeling the ultrasonic velocities of the samples, this exercise is only performed for those samples where ultrasonic velocities were measured. Furthermore, since there is less than 1% halite + apatite in these samples, it is eliminated from this conversion.

The bulk density and $P$- and $S$-wave velocity for the different constituent minerals are used to calculate the elastic moduli of each mineral. The bulk modulus, $K$, and the shear modulus, $G$, are calculated $K = \rho V_P^2$ and $G = \rho V_S^2$. To calculate the modulus of the solid phase (the modulus if the sample had a porosity of zero), the moduli of the constituent minerals of each sample and the volume fraction of those minerals are used with the Hill (1952) average:

$$M_H = .5\left[\sum_{i=1}^{N} f_i M_i + \left(\sum_{i=1}^{N} \frac{f_i}{M_i}\right)^{-1}\right]$$

where $f_i$ is the volume fraction of a mineral in the solid phase and $M_i$ is the modulus (either $K$ or $G$) of that mineral. The volume fractions of the constituent minerals for the relevant samples, together with the bulk and shear moduli of the solid phase, are shown in Appendix C.

## REFERENCES

Blangy, J.P., 1992, Integrated seismic lithologic interpretation: The petrophysical basis: Ph.D. thesis, Stanford University.

Castagna, J. P., Batzle, M. L., and Eastwood, R. L., 1985, Relationships between compressional and shear wave velocities in silicate rocks, Geophysics, **50**, 571-581.

Dandekar, D.P., 1968, Pressure dependence of the elastic constants of calcite, Phys. Rev, **172**, 873.

Hill, R., 1952, The elastic behavior of crystalline aggregate, Proc. Phys. Soc. London, A65, 349-354.

McSkimm, J. J., Andreatch, P., Jr., and Thurston, R.N.l, 1965, Elastic moduli of quartz vs. hydrostatic pressure at 25 and 195.8 degrees Celsius, J. Appl. Phys., **36**, 1632.

Ryzhova, T. V., Aleksandrov, K.S., 1965, The elastic properties of potassium-sodium feldspars, Bull. Acad. Sci. USSR Geophysics Series, **7**, 53.

# APPENDIX C

# FTIR DATA IN VOLUME FRACTION & SOLID MODULI

ASPHALTO (well 332X-25Z, Sec25-T30S/R22E)

| depth (ft) | phi | opal-A | opal-CT | quartz | total fsp | total clay | calcite | pyrite | org | Ks (GPa) | Gs (GPa) |
|---|---|---|---|---|---|---|---|---|---|---|---|
| 5874.5 | 0.219 | 0 | 0 | 0.537 | 0.147 | 0.220 | 0 | 0.016 | 0.080 | 26.52 | 23.08 |
| 5876.5 | 0.266 | 0 | 0 | 0.701 | 0.156 | 0.133 | 0 | 0.010 | 0 | 37.44 | 32.62 |
| 5887.3 | 0.212 | 0 | 0 | 0.651 | 0.145 | 0.184 | 0.010 | 0.010 | 0 | 36.53 | 30.24 |
| 5892.5 | 0.223 | 0 | 0 | 0.675 | 0.125 | 0.185 | 0 | 0.016 | 0 | 36.18 | 30.82 |
| 5900.4 | 0.152 | 0 | 0 | 0.461 | 0.187 | 0.317 | 0.020 | 0.016 | 0 | 34.92 | 24.85 |
| 5913.7 | 0.149 | 0 | 0 | 0.407 | 0.161 | 0.290 | 0.041 | 0.017 | 0.084 | 26.43 | 20.64 |
| 5916.5 | 0.259 | 0 | 0 | 0.675 | 0.135 | 0.174 | 0 | 0.016 | 0 | 36.52 | 31.15 |
| 5931.5 | 0.327 | 0 | 0.179 | 0.527 | 0.092 | 0.108 | 0.020 | 0.009 | 0.066 | 25.03 | 23.03 |
| 5932.5 | 0.254 | 0 | 0.228 | 0.505 | 0.101 | 0.092 | 0.012 | 0.008 | 0.055 | 24.94 | 22.16 |
| 5937.5 | 0.195 | 0 | 0.526 | 0.310 | 0.066 | 0.052 | 0 | 0.005 | 0.040 | 20.21 | 18.13 |
| 5942.1 | 0.445 | 0 | 0.359 | 0.390 | 0.030 | 0.118 | 0.028 | 0.006 | 0.069 | 21.06 | 19.19 |
| 5957.3 | 0.228 | 0 | 0 | 0.644 | 0.127 | 0.134 | 0.011 | 0.012 | 0.071 | 28.09 | 25.91 |
| 5958.2 | 0.296 | 0 | 0.377 | 0.390 | 0.052 | 0.096 | 0.033 | 0.008 | 0.045 | 22.74 | 20.48 |

MCKITTRICK FIELD (well 342-17Z at Sec17?-T30S/R22E)

| depth (ft) | phi | bulk density | opal-A | opal-CT | quartz | total fsp | total clay | cal-cite | pyrite | org | Ks (GPa) | Gs (GPa) |
|---|---|---|---|---|---|---|---|---|---|---|---|---|
| 3248.5 | 0.390 | 1.394 | 0 | 0.729 | 0 | 0.187 | 0.075 | 0 | 0.009 | 0 | 22.01 | 15.83 |
| 3255.5 | 0.454 | 1.219 | 0 | 0.904 | 0 | 0.096 | 0 | 0 | 0 | 0 | 19.43 | 16.08 |
| 3262.5 | 0.333 | 1.421 | 0 | 0.977 | 0 | 0 | 0.023 | 0 | 0 | 0 | 15.135 | 12.96 |
| 3268.5 | 0.373 | 1.491 | 0 | 0.961 | 0 | 0.039 | 0 | 0 | 0 | 0 | 15.719 | 13.53 |
| 3273.5 | 0.341 | 1.416 | 0 | 0.759 | 0 | 0.159 | 0.082 | 0 | 0 | 0 | 20.485 | 14.57 |
| 3306.0 | 0.348 | 1.480 | 0 | 0.766 | 0 | 0.126 | 0.100 | 0 | 0.008 | 0 | 19.976 | 14.46 |
| 3317.5 | 0.394 | 1.365 | 0 | 0.889 | 0 | 0 | 0.111 | 0 | 0 | 0 | 16.377 | 12.18 |
| 3337.5 | 0.367 | 1.234 | 0 | 0.961 | 0 | 0 | 0.039 | 0 | 0 | 0 | 16.639 | 13.73 |
| 3600.5 | 0.416 | 1.321 | 0 | 0.795 | 0 | 0.108 | 0.098 | 0 | 0 | 0 | 19.598 | 13.89 |
| 3603.5 | 0.433 | 1.287 | 0 | 0.921 | 0 | 0.032 | 0.047 | 0 | 0 | 0 | 17.38 | 13.86 |
| 3606.5 | 0.416 | 1.254 | 0 | 0.921 | 0 | 0 | 0.079 | 0 | 0 | 0 | 16.98 | 13.07 |
| 3670.5 | 0.337 | 1.517 | 0 | 0.863 | 0 | 0.041 | 0.096 | 0 | 0 | 0 | 16.80 | 12.63 |
| 3678.5 | 0.358 | 1.450 | 0 | 0.724 | 0 | 0.118 | 0.141 | 0.016 | 0 | 0 | 20.45 | 13.50 |
| 3681.0 | 0.343 | 1.475 | 0 | 0.706 | 0 | 0.102 | 0.192 | 0 | 0 | 0 | 19.58 | 12.46 |
| 3684.5 | 0.418 | 1.266 | 0 | 0.897 | 0 | 0 | 0.103 | 0 | 0 | 0 | 16.83 | 12.52 |

CYMRIC FIELD (well 1407R-1Y, Sec1-T29S/R21E)

| depth (ft) | phi | opal-A | opal-CT | quartz | total fsp | total clay | cal-cite | pyrite | anal-cime | Ks (GPa) | Gs (GPa) |
|---|---|---|---|---|---|---|---|---|---|---|---|
| 1240.3 | 0.520 | 0.493 | 0 | 0 | 0.147 | 0.000 | 0 | 0.005 | 0.355 | 68.41 | 33.27 |
| 1240.7 | 0.666 | 0.560 | 0.264 | 0.016 | 0.066 | 0.089 | 0 | 0.004 | 0 | 25.58 | 18.35 |
| 1242.8 | 0.625 | 0.000 | 0.786 | 0 | 0.100 | 0.114 | 0 | 0 | 0 | 17.49 | 13.13 |
| 1246.7 | 0.628 | 0.267 | 0.502 | 0 | 0.083 | 0.148 | 0 | 0 | 0 | 18.85 | 13.33 |
| 1248.7 | 0.656 | 0.432 | 0.380 | 0 | 0.082 | 0.105 | 0 | 0 | 0 | 21.14 | 15.06 |
| 1249 | 0.646 | 0.740 | 0.164 | 0 | 0.032 | 0.063 | 0 | 0 | 0 | 35.86 | 25.15 |
| 1249.3 | 0.683 | 0.594 | 0.292 | 0 | 0.041 | 0.000 | 0 | 0.004 | 0.069 | 27.37 | 21.84 |
| 1255.2 | 0.654 | 0.000 | 0.812 | 0 | 0.066 | 0.122 | 0 | 0 | 0 | 16.66 | 12.74 |
| 1256.3 | 0.645 | 0.247 | 0.527 | 0 | 0.118 | 0.099 | 0 | 0.008 | 0 | 19.70 | 14.63 |
| 1257.7 | 0.553 | 0.000 | 0.821 | 0 | 0.058 | 0.121 | 0 | 0 | 0 | 16.44 | 12.65 |
| 1259.2 | 0.590 | 0.000 | 0.697 | 0 | 0.111 | 0.184 | 0.008 | 0 | 0 | 18.58 | 13.04 |

Abbreviations: Bulk, (Ks), and shear, (Gs), moduli of the solid phase. Density is in g/cm$^3$.

# APPENDIX D

# DRY ULTRASONIC VELOCITY DATA

ASPHALTO (well 332X-25Z, Sec25-T30S/R22E)

| depth (ft) | porosity | Vp 7.5 MPa (km/s) | Vs 7.5 MPa (km/s) | Vp 10 MPa (km/s) | Vs 10 MPa (km/s) | Vp 15 MPa (km/s) | Vs 15 MPa (km/s) | Vp 30 MPa (km/s) | Vs 30 MPa (km/s) |
|---|---|---|---|---|---|---|---|---|---|
| 5874.5 | 0.219 | 3.409 | 1.845 | 3.411 | 1.664 | 3.416 | 1.682 | 3.473 | 1.701 |
| 5876.5 | 0.266 | 3.362 | 1.867 | 3.376 | 1.879 | 3.403 | 1.888 | 3.467 | 1.920 |
| 5887.3 | 0.212 | 3.206 | 1.927 | 3.222 | 1.943 | 3.223 | 1.967 | 3.244 | 1.988 |
| 5892.5 | 0.223 | 3.523 | 1.543 | 3.526 | 1.721 | 3.554 | 1.736 | 3.569 | 1.765 |
| 5900.4 | 0.152 | 3.548 | 2.121 | 3.564 | 2.123 | 3.575 | 2.130 | 3.610 | 2.166 |
| 5913.7 | 0.149 | 3.520 | 2.104 | 3.556 | 2.108 | 3.603 | 2.146 | 3.654 | 2.181 |
| 5916.5 | 0.259 | 2.771 | 1.709 | 2.832 | 1.724 | 2.887 | 1.557 | 3.024 | 1.831 |
| 5931.5 | 0.327 | 2.929 | 1.767 | 2.951 | 1.784 | 2.994 | 1.806 | 3.036 | 1.863 |
| 5932.5 | 0.254 | 3.306 | 1.591 | 3.305 | 1.598 | 3.329 | 1.601 | 3.809 | 1.634 |
| 5937.5 | 0.195 | 3.842 | 1.844 | 3.849 | 1.856 | 3.835 | 1.854 | 3.923 | 1.864 |
| 5942.1 | 0.445 | 2.165 | 1.183 | 2.210 | 1.202 | 2.247 | 1.231 | 2.295 | 1.275 |
| 5957.3 | 0.228 | 3.251 | 2.188 | 3.278 | 2.192 | 3.275 | 2.119 | 3.358 | 2.225 |
| 5958.2 | 0.296 | 3.027 | 1.997 | 3.025 | 2.038 | 2.998 | 2.062 | 3.050 | 2.115 |

MCKITTRICK FIELD (well 342-17Z at Sec17?-T30S/R22E)

| depth (ft) | porosity | Vp 7.5 MPa (km/s) | Vs 7.5 MPa (km/s) | Vp 10 MPa (km/s) | Vs 10 MPa (km/s) | Vp 15 MPa (km/s) | Vs 15 MPa (km/s) | Vp 30 MPa (km/s) | Vs 30 MPa (km/s) |
|---|---|---|---|---|---|---|---|---|---|
| 3248.5 | 0.390 | 2.341 | 1.404 | | | | | | |
| 3255.5 | 0.454 | 2.325 | 1.382 | 2.329 | 1.388 | 2.341 | 1.397 | 2.363 | 1.408 |
| 3262.5 | 0.333 | 2.883 | 1.802 | 2.886 | 1.814 | 2.889 | 1.814 | 2.911 | 1.821 |
| 3268.5 | 0.373 | 3.266 | 2.058 | 3.270 | 2.058 | 3.271 | 2.059 | 3.286 | 2.069 |
| 3273.5 | 0.341 | 2.628 | 1.658 | 2.629 | 1.665 | 2.636 | 1.678 | 2.664 | 1.696 |
| 3306.0 | 0.348 | 2.534 | 1.610 | 2.537 | 1.618 | 2.557 | 1.633 | 2.624 | 1.658 |
| 3317.5 | 0.394 | 2.375 | 1.507 | 2.390 | 1.513 | 2.445 | 1.517 | 2.488 | 1.560 |
| 3337.5 | 0.367 | 2.163 | | 2.195 | 1.073 | 2.326 | 1.074 | 2.387 | 1.150 |
| 3600.5 | 0.416 | 2.238 | 0.8653 | 2.288 | 1.367 | 2.310 | 1.372 | 2.375 | 1.532 |
| 3603.5 | 0.433 | 2.302 | 1.446 | 2.302 | 1.446 | 2.313 | 1.544 | 2.353 | 1.509 |
| 3606.5 | 0.416 | 2.307 | 1.414 | 2.320 | 1.419 | 2.335 | 1.430 | 2.353 | 1.452 |
| 3670.5 | 0.337 | 2.692 | 1.611 | 2.713 | 1.626 | 2.745 | 1.681 | 2.825 | 1.724 |
| 3678.5 | 0.358 | 2.539 | 1.582 | 2.549 | 1.598 | 2.564 | 1.613 | 2.615 | 1.631 |
| 3681.0 | 0.343 | 2.371 | 1.368 | 2.418 | 1.377 | 2.448 | 1.390 | 2.539 | 1.414 |
| 3684.5 | 0.418 | 2.218 | 1.442 | 2.220 | 1.450 | 2.257 | 1.461 | 2.288 | 1.481 |

CYMRIC FIELD (well 1407R-1Y, Sec1-T29S/R21E)

| depth (ft) | porosity | Vp 7.5 MPa (km/s) | Vs 7.5 MPa (km/s) | Vp 10 MPa (km/s) | Vs 10 MPa (km/s) | Vp 15 MPa (km/s) | Vs 15 MPa (km/s) | Vp 30 MPa (km/s) | Vs 30 MPa (km/s) |
|---|---|---|---|---|---|---|---|---|---|
| 1240.7 | 0.666 | 1.313 | 1.045 | 1.355 | 1.056 | 1.443 | 1.073 | 1.631 | 1.109 |
| 1246.7 | 0.628 | 1.366 | 1.028 | 1.388 | 1.039 | 1.416 | 1.050 | 1.566 | 1.040 |
| 1249.3 | 0.683 | 1.186 | 0.7945 | 1.221 | 0.7986 | 1.271 | 0.8078 | | |
| 1255.2 | 0.654 | 1.341 | 0.8296 | 1.333 | 0.8381 | 1.390 | 0.8535 | | |
| 1256.3 | 0.645 | 1.308 | | 1.306 | 0.9269 | 1.380 | 0.9418 | | |
| 1257.7 | 0.553 | 1.594 | | 1.604 | | 1.643 | | | |
| 1259.2 | 0.59 | 1.433 | 0.8921 | 1.466 | 0.9021 | 1.549 | 0.9165 | 1.650 | 0.9580 |

# APPENDIX E

# RAW WAVEFORMS

Chapter 2 presents waveforms from ultrasonic velocity measurements from one of the opal samples and two samples each from the Cymric, Asphalto, and McKittrick reservoirs. This appendix presents waveforms at multiple pressures together with tables of time picks and length information. All waveforms are from loading experiments unless noted. Therefore, the pressure designated is the greatest pressure experienced in the laboratory.

The travel times cannot be directly transferred into velocity because a lag time exists for the signal to travel from the pulse generator to the transducers. In addition, parrafilm was used on both ends of each sample as a coupling material. In the tables below, compressional-wave velocity was picked on the first trough, for which the lag time is 10 μs; shear-wave velocity was picked on the first peak, for which the lag time is 21.24 μs.

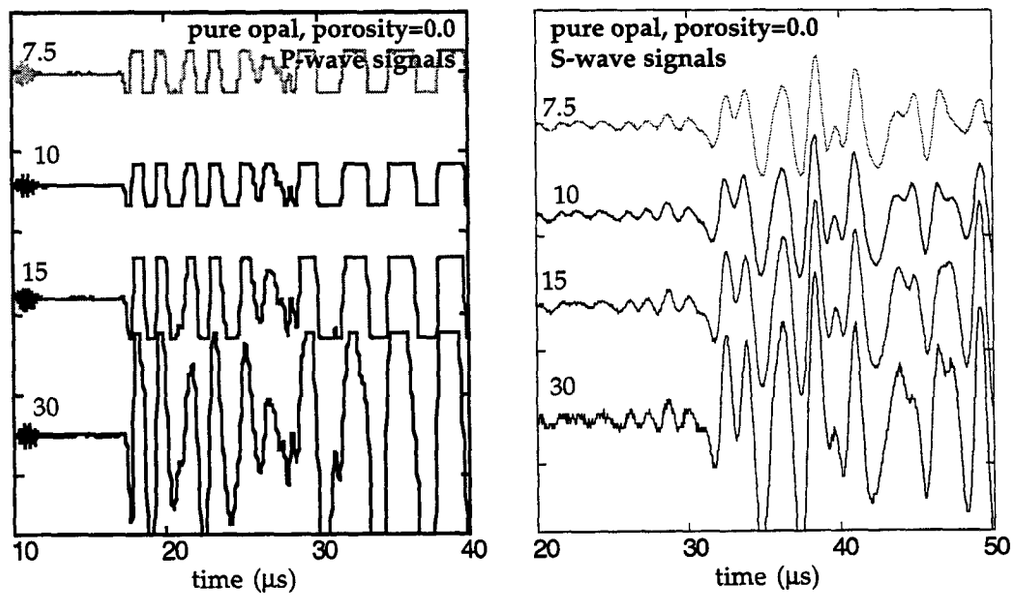


| Pressure (MPa) | sample length (mm) | tp (μs) | ts (μs) | Vp (km/s) | Vs (km/s) |
|---|---|---|---|---|---|
| 7.5 | 28.255 | 17.22 | 32.56 | 3.91 | 2.50 |
| 10 | 28.255 | 17.22 | 32.51 | 3.91 | 2.51 |
| 15 | 28.245 | 17.20 | 32.51 | 3.92 | 2.51 |
| 30 | 28.215 | 17.17 | 32.49 | 3.94 | 2.51 |

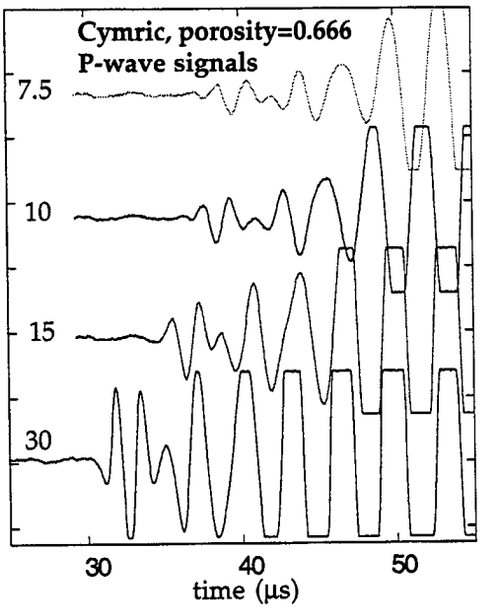


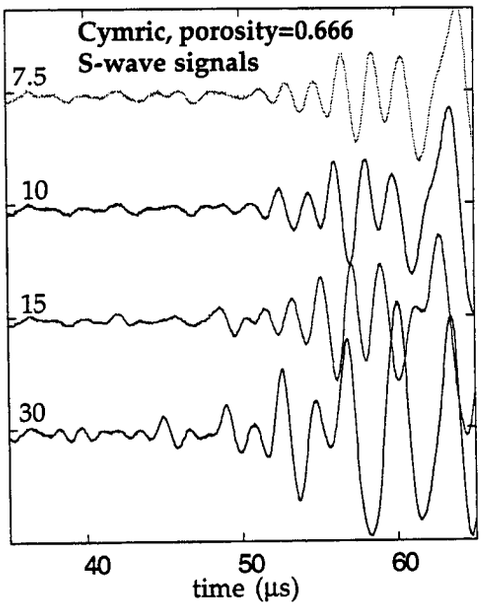


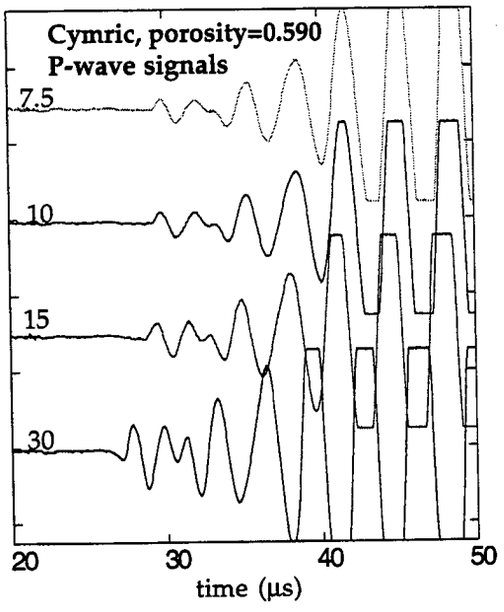


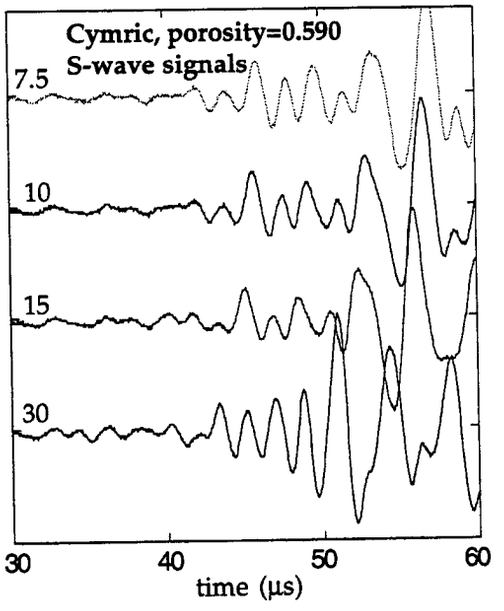


| | porosity=0.666, depth=1240.7 ft | | | | | porosity=0.59, depth=1259.2 ft | | | | |
|---|---|---|---|---|---|---|---|---|---|---|
| Pressure (MPa) | length (mm) | tp (μs) | ts (μs) | Vp (km/s) | Vs (km/s) | length (mm) | tp (mm) | ts (μs) | Vp (km/s) | Vs (km/s) |
| 7.5 MPa | 36.847 | 37.08 | 56.50 | 1.39 | 1.05 | 27.03 | 28.96 | 51.54 | 1.43 | 0.892 |
| 10 MPa | 36.597 | 36.33 | 55.90 | 1.42 | 1.06 | 26.98 | 28.51 | 51.15 | 1.47 | 0.902 |
| 15 MPa | 36.007 | 35.55 | 54.80 | 1.44 | 1.07 | 26.85 | 27.44 | 50.54 | 1.55 | 0.916 |
| 30 MPa | 34.707 | 31.87 | 53.12 | 1.63 | 1.09 | 26.39 | 26.10 | 48.79 | 1.65 | 0.958 |

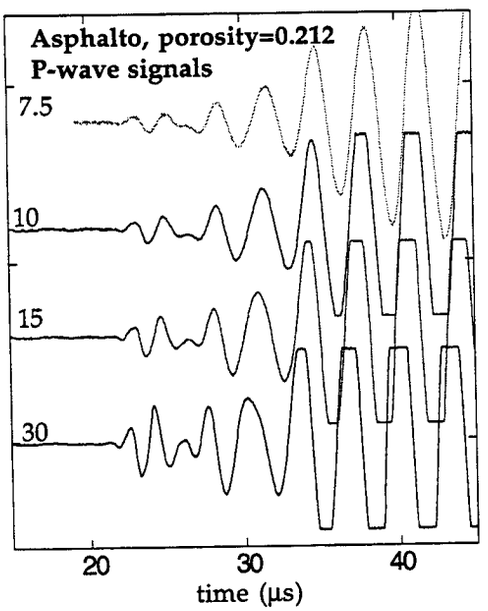


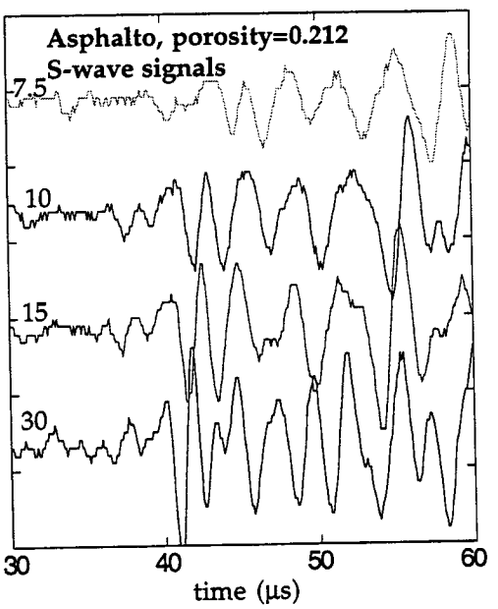


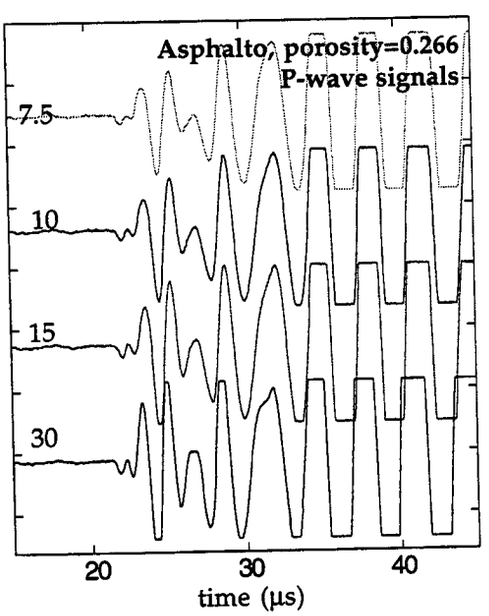


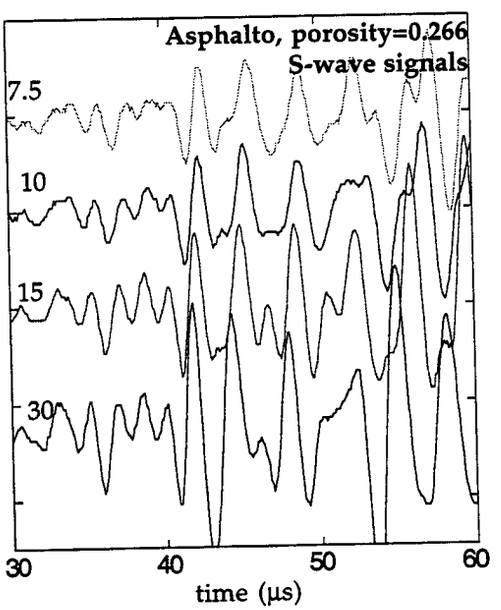


| | porosity=0.212, depth = 5887.3 ft | | | | | porosity=0.266, depth = 5876.5 ft | | | | |
|---|---|---|---|---|---|---|---|---|---|---|
| Pressure (MPa) | length (mm) | tp (μs) | ts (μs) | Vp (km/s) | Vs (km/s) | length (mm) | tp (mm) | ts (μs) | Vp (km/s) | Vs (km/s) |
| 7.5 MPa | 37.826 | 21.96 | 43.34 | 3.206 | 1.927 | 39.661 | 21.80 | 42.43 | 3.362 | 1.867 |
| 10 MPa | 37.814 | 21.93 | 40.92 | 3.222 | 1.943 | 39.653 | 21.74 | 42.34 | 3.376 | 1.879 |
| 15 MPa | 37.797 | 21.83 | 40.53 | 3.223 | 1.967 | 39.632 | 21.66 | 42.03 | 3.403 | 1.888 |
| 30 MPa | 37.757 | 21.46 | 40.11 | 3.323 | 2.003 | 39.591 | 21.40 | 41.83 | 3.467 | 1.920 |

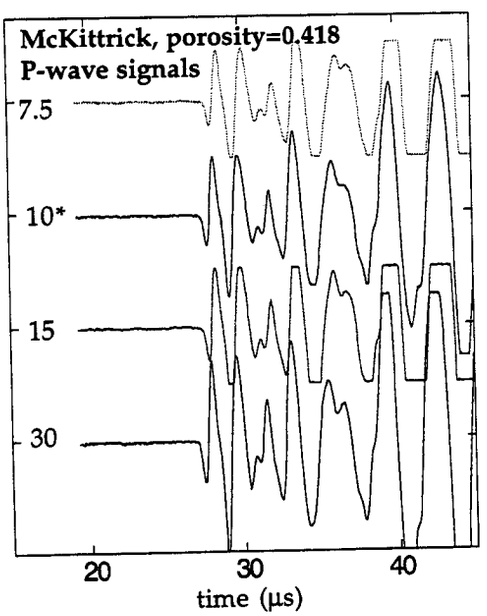


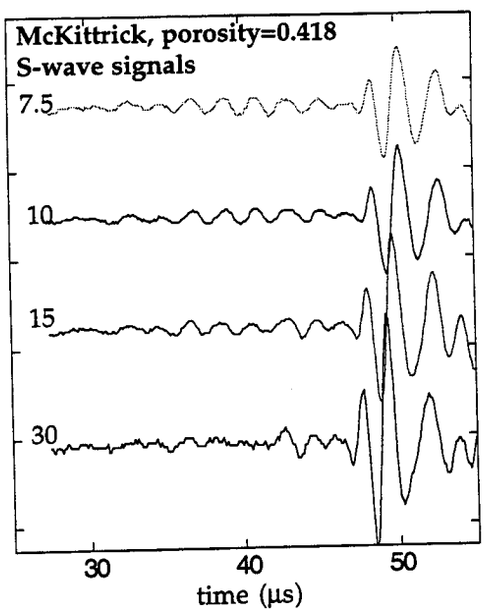


* waveform from pressure unloading

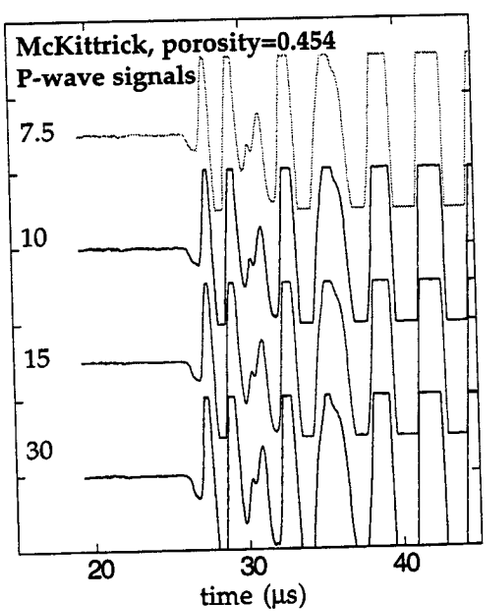


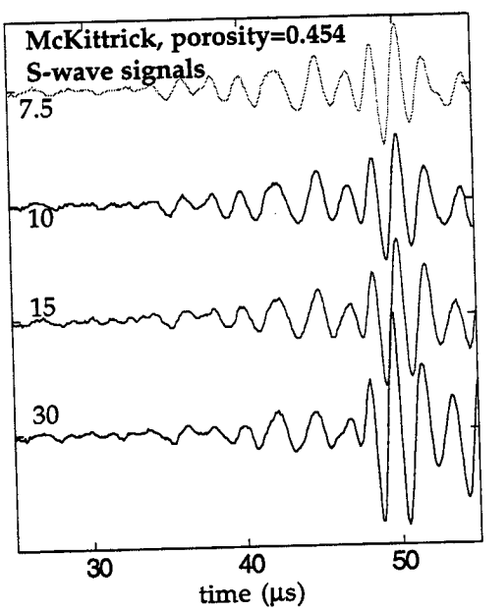


| | porosity=0.418, depth = 3684.5ft | | | | | porosity=0.454, depth = 3255.5 ft | | | | |
|---|---|---|---|---|---|---|---|---|---|---|
| Pressure (MPa) | length (mm) | tp (μs) | ts (μs) | Vp (km/s) | Vs (km/s) | length (mm) | tp (mm) | ts (μs) | Vp (km/s) | Vs (km/s) |
| 7.5 MPa | 39.268 | 27.68 | 48.46 | 2.218 | 1.442 | 37.835 | 26.35 | 48.52 | 2.325 | 1.3818 |
| 10 MPa | 39.250 | 27.36 | 48.44 | 2.220 | 1.449 | 37.823 | 26.29 | 48.49 | 2.329 | 1.3875 |
| 15 MPa | 39.205 | 27.41 | 48.04 | 2.257 | 1.461 | 37.796 | 26.25 | 48.34 | 2.341 | 1.3966 |
| 30 MPa | 39.073 | 27.07 | 47.72 | 2.288 | 1.480 | 37.692 | 25.95 | 48.04 | 2.363 | 1.4083 |